TNO innovation for life

Porosity-depth relation for unconsolidated sediments of the Upper North Sea Group

Donna Dieperink | TNO Intern

28 March 2024

Energy & Materials Transition
www.tno.nl
+31 88 866 42 56
info@tno.nl

28 March 2024

Porosity-depth relation for unconsolidated sediments of the Upper North Sea Group

Author	Donna Dieperink
Function	TNO Intern
Student number	2640649
Course Component	Master Thesis Earth Sciences
Course Code	AM_1186
Insitution	Vrije Universiteit (VU)
Department	Faculty of Science
Research Mentors	Hans Veldkamp, TNO, hans.veldkamp@tno.nl
	Lies Peters, TNO, lies.peters@tno.nl
VU Supervisors	John Reijmer, VU, j.j.g.reijmer@vu.nl
	Jeroen van der Lubbe, VU, h.j.l.vander.lubbe@vu.nl
Second Assessor	Bernd Andeweg, VU, bernd.andeweg@vu.nl

Abstract

For geothermal applications porosity and permeability data are of great importance, as these are necessary to indicate geothermal potential. However, in the mid-depth range (100-1200 m), where potential reservoirs for shallow geothermal applications in the Breda, Oosterhout, and Maassluis Formations of the Upper North Sea Group may be present, there is a lack of such data.

The objective of this study is to estimate porosity from unconsolidated sediments in the Upper North-Sea group and indicate porosity-depth relations across the mid-depth range. Porosity calculations using sonic and density log data, along with five compaction experiments up to 30 MPa, including pycnometer, displacement and acoustic velocity measurements, and CT-scans, are performed on selected wells and samples from the Liessel core (Breda Fm) to estimate porosity.

Porosity estimates calculated from well log data show large error ranges and should be based on both the sonic and density log. The porosity calculations based on both log types for sands (GR < 30 gAPI) show a relatively good fit with Athy's compaction curve currently used for sands in the Upper North Sea Group.

Experimental porosity estimates lack the quality required to indicate porosity-depth relations. The achieved CT-scan resolution is insufficient for accurate porosity estimates. The acoustic velocity measurements are affected by the aluminum casing surrounding the samples. Effective porosity measurements by a pycnometer obtained from selected samples of the Liessel core at larger depths in the range of 30-36%, are not significantly lower than surface measurements. The total porosity estimates calculated from displacement with increasing pressure show a porosity reduction of 6.6 % to 13.5 %. These total porosities are potentially influenced by sample loss during the experiment. Significant differences between these experimental porosity estimates and their poor fit with Athy's curve questions the quality of these data.

Both calculations on porosity from log data and experimental porosity estimates have significant potential to contribute to fully assess the porosity-depth relation. More research into the lithology of the Upper North Sea group, log data quality, and experimental techniques is advised to improve the application of the methods used.

Table of Contents

CT-scan data and acoustic velocity data can be requested from TNO.

1. Introduction

1.1 Shallow geothermal energy

To accelerate the energy transition and cover the increasing energy demand, the use of renewable energy sources should be expanded. Heating and cooling make up about the half of the energy consumption in the EU that at present is for 85% produced by fossil fuels and accounts for 40% of the global CO_2 emissions (Ahmed et al., 2022; Drijver, Bakema, & Oerlemans, 2019). Geothermal energy is a sustainable heat source that could reduce our dependence on fossil fuels for heating and electricity demands (Barbier, 2002). Shallow geothermal energy systems are more technically and economically accessible compared to deep high-temperature geothermal systems, as they are located closer to the surface (Gil et al., 2022). There is no general depth range for shallow geothermal energy, but the following techniques are performed within the mid-depth subsurface range (100-1200 m): well-doublet systems, ground-source heat pumps (GSHP) and underground thermal energy storage (UTES; Al-Khoury, 2011; Tsagarakis et al., 2020). One of the highest efficiencies among other renewable energy systems is produced by GSHP with an efficiency range of 300-500% (Ahmed et al., 2022). Therefore, this is a promising technology to minimize our dependence on fossil fuels for heating. High Temperature Aquifer Thermal Energy Storage (HT-ATES) is a promising technique of UTES, in which the extraction of water from a cold well is used for cooling and from a warm well for heating (Fig. 1.1; (Drijver, Bakema, & Oerlemans, 2019). This technique can be combined with other heat sources for energy storage and can therefore decrease seasonal imbalance in energy demand and supply (Ahmed et al., 2022). Shallow well-doublet systems range from ~500 to ~1500 m depth and reach water temperatures up to approximately 40 °C (Fig. 1.2; RVO, 2017). Depending on the heat demand the temperature gained using these systems can be increased using heat pumps. For example, in Zevenbergen (The Netherlands), a doublet system was realized, reaching the Brussels Sand layer at depths ranging from 600-700 m, with water temperatures of approximately 31 °C (Buik & Bakema, 2019). The produced low-temperature heat in combination with a heat pump, is sufficient to heat greenhouses in the area. Each year this doublet system can produce 30.000 MWh, which is equivalent to the energy produced from 3 million m^3 natural gas (Buik & Bakema, 2019).

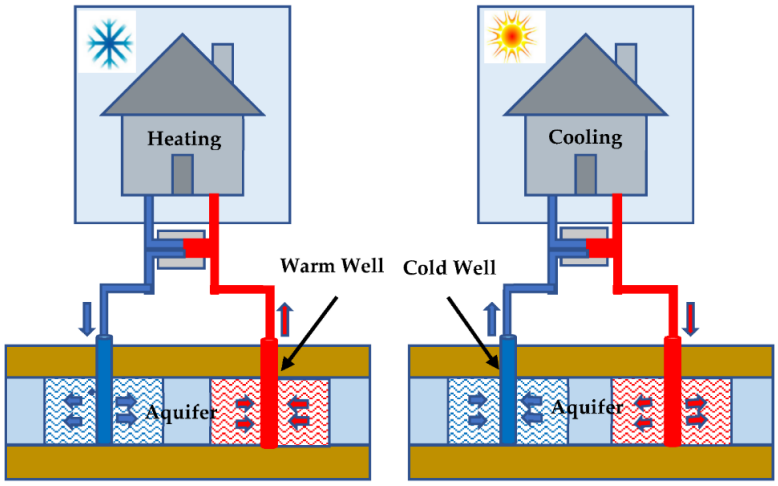

Fig. 1.1 HI-ATES system during winter and summer (Ahmed et al., 2022). Blue- and red marked systems with arrows denote the cooling (blue) energy system entering/leaving the aquifer and the heating (red) system entering/leaving the aquifer.

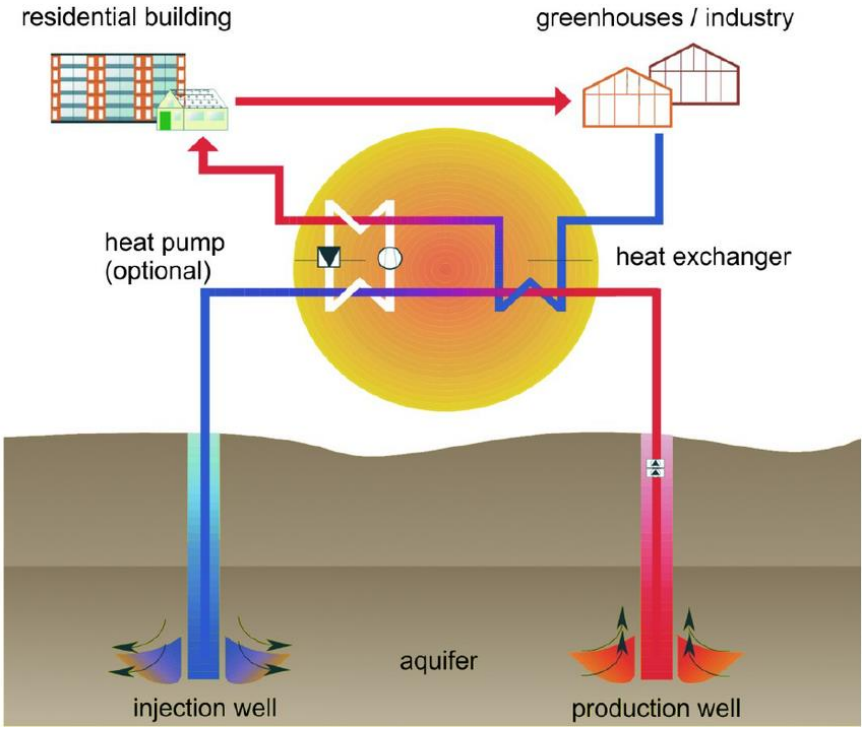

Fig. 1.2 Well doublet-system including an injection well (blue stream), which transports cold water into the subsurface and a projection well (red stream), from which heated water is transported to the surface to heat houses, greenhouses or industry (Agemar, Weber, & Schulz, 2014).

Formations that could act as suitable aquifer for application of shallow geothermal energy techniques within the mid-depth range are the Breda, Oosterhout and Maassluis Formations (Drijver, Bakema, & Oerlemans, 2019; Hartog, Griffioen, & van Bergen, 2005). The economic potential and technical feasibility are part of the geothermal potential and are displayed in ThermoGIS. The technical power is calculated in a technical model using DoubletCalc1D (Mijnlieff et al., 2014) and can be simplified with the formula:

$$P_{ww} = Q_v \times \rho_w \times c_p \times \Delta T_{ww}$$

Eq. 1.1

In which P_{ww} is the geothermal power (W), Q_v is the flow rate (m^3/s), ρ_w is the density of the formation water c_p is the heat capacity of the water (J/(kg*K) and ΔT_{ww} is the temperature difference (K) (Lako et al.; Mijnlieff et al., 2014). The flow rate is directly influenced by the permeability of the reservoir, as stated in Darcy's law (Darcy, 1856). Therefore, to indicate the geothermal potential of aquifers in the shallow subsurface, porosity and permeability data of the reservoir are of great importance (Békési et al., 2020; Veldkamp, Geel, & Peters, 2022). The permeability of a reservoir is strongly affected by the porosity, but there is no one-to-one relationship between these factors due to compaction (Bernabé, Mok, & Evans, 2003). In the mid-depth range (100-1200 m) there is a lack of readily applicable data, as shallow boreholes for groundwater mostly do not exceed 100 m depth and detailed information on boreholes for oil and gas exploration is mostly not available down to ~1000 m depth (Fig. 1.3; TNO, 2023a, 2023b). Deep wells mostly include petrophysical data obtained from well-logging, and sometimes core plugs. This data is available from the Netherlands Oil- and Gas portal (NLOG; TNO,

2023b). There are high numbers of 'deep' wells covering the mid-depth range of 100-1200 m, but most of these lack high quality log data in this interval (Fig. 1.3). Shallow wells also contain petrophysical data, which are mostly obtained from core/cutting descriptions. Compared to deep wells they rarely include petrophysical log data. They are available from the Data and Information of the Dutch Subsurface counter (DINOloket; TNO, 2023a). Within these petrophysical data permeability measurements are abundant at shallow depths (<50 m; TNO, 2023a). Extrapolation of these permeability data to larger depths introduces large uncertainty, because of the effects of compaction. Based on porosity-permeability relations, porosity data in the mid-depth range could support extrapolation of these permeability measurements at shallow depths for higher depths. Therefore, available porosity data in the mid-depth range are combined with experimentally derived porosity data to better estimate the geothermal potential of reservoirs in the Breda, Oosterhout, and Maassluis Formations.

1.2 Objective

The objective of this project is to determine the rate of porosity reduction with increasing burial depth for the unconsolidated Breda, Oosterhout, and Maassluis Formations in the mid-depth range (100-1200 m). To reach this objective an overview of porosity-depth relations of data covering the mid-depth range will be prepared and combined with porosity data from compaction experiments.

1.3 Research area

In this project the boundaries of the mid-depth range are set from 100 m to 1200 m in the subsurface, which predominantly covers the Upper, Middle and Lower North Sea Groups (Fig. 1.4 and Fig. 1.6). The Breda, Oosterhout and Maassluis Formations, whose porosity-depth relations are highlighted in this project, are all part of the Upper North Sea Group (Fig. 1.5). Samples for compaction experiments were collected from the Liessel core, B52C2133 (Fig. 9.1). In the succeeding paragraphs the main characteristics of the investigated formations and the Liessel core are discussed.

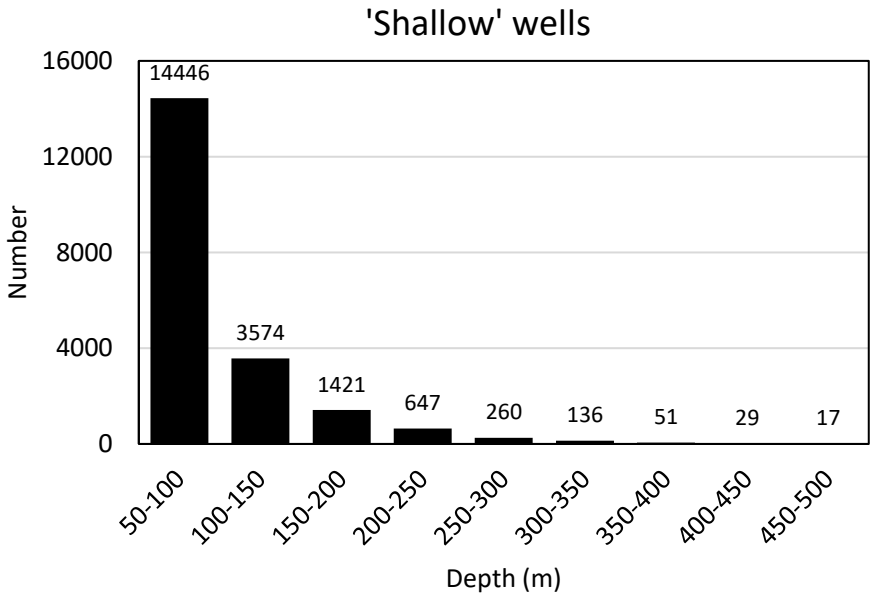

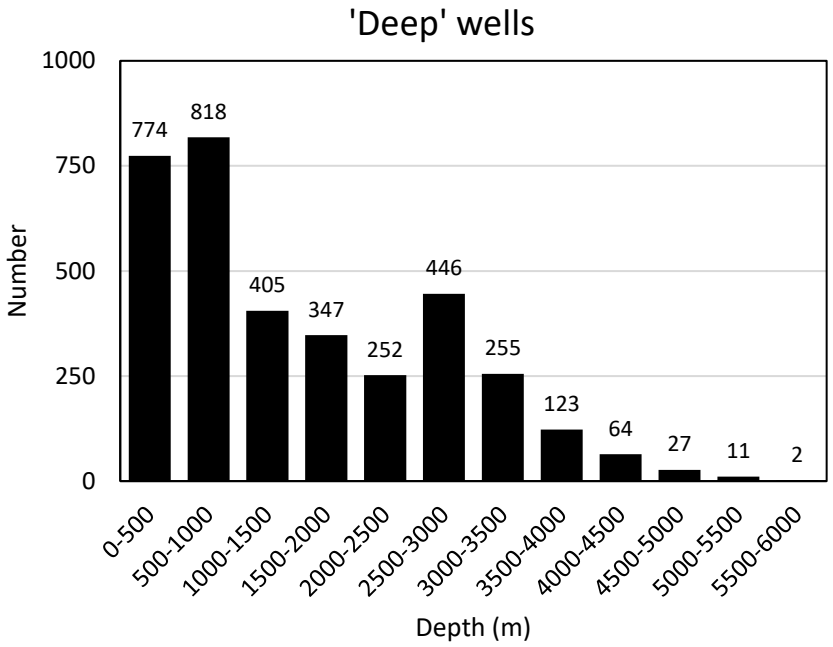

Fig. 1.3 The number of 'shallow' and 'deep wells' for different ranges of end depths from the wells (TNO, 2023a, 2023b). The available 'shallow' wells in the depth range 0-50 m are not displayed in this figure.

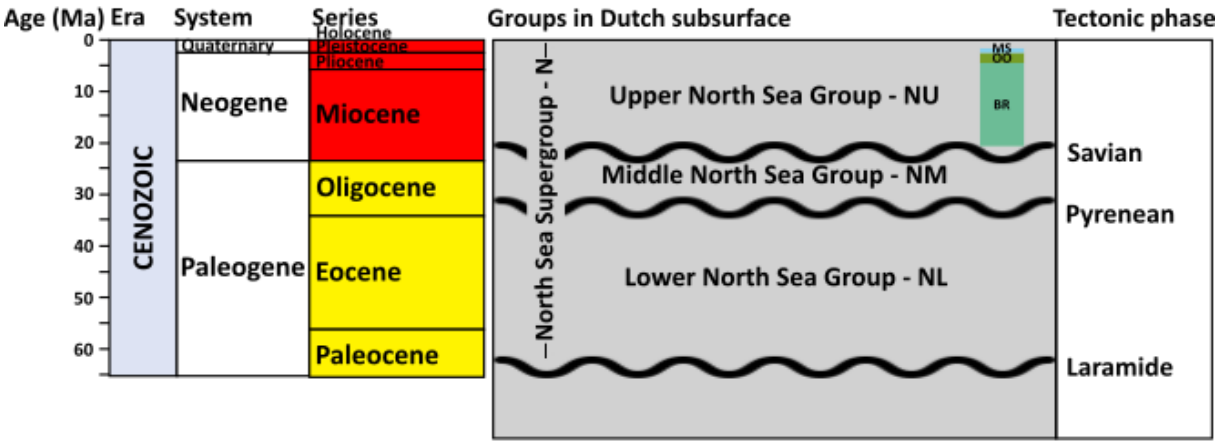

Fig. 1.4 Overview of the age and tectonic phase, dividing the Lower, Middle, and Upper North Sea Group of the North Sea Supergroup. Further division in the Breda (BR), Oosterhout (OO), and Maassluis (MS) Formations are displayed in the Upper North Sea Group.

1.3.1 Breda Formation

The Breda Formation comprises Burdigalian-Zanclean marine sediments (Munsterman et al., 2019; Slupik et al., 2007). The maximum thickness of this deposit is located within the Roer Valley Graben and gradually thins towards the northwest of the Netherlands (Fig. 1.7; TNO, 2023a). Throughout the Breda Formation, shallow marine grey/black-green silty clays alternate with silts or very fine- to calcareous or glauconitic, moderately fine-grained sands (105-210 µm; Munsterman et al., 2019). These sediments are interpreted to be deposited primarily in restricted and open marine depositional environments (Verbeek et al., 2002). Presence of clinoforms and prograding sedimentation patterns often indicate a deltaic depositional environment in which the sediments comprising the Breda

Formation were deposited (Verbeek et al., 2002). Three unconformities are present within the succession of the Breda Formation. These unconformities define the boundaries of the units of the Breda Formation (Munsterman et al., 2019). The Early Miocene Unconformity (EMU; Fig. 1.4 and Fig. 1.5) indicates the transition from the deposits of the underlying Veldhoven formation to the sediments of Breda formation (Munsterman et al., 2019; Verbeek et al., 2002). Furthermore, it is proposed to split up the Breda Formation in two different units, the Groote Heide and Diessen Formations, because of the presence of the Mid-Miocene Unconformity (MMU) and distinct lithological characteristics (Fig. 1.5). The Late Miocene Unconformity (LMU) separates the sediments of the Breda Formation from those of the overlying Oosterhout Formation (section 1.3.2; Munsterman et al., 2019). The Groote Heide Formation consists of a mix of sandy, silty and calcareous fine-grained glauconitic sands together with sandy to silty clays. The presence of glauconite is a defining characteristic of this formation. The sediments of the Groote Heide Formation are deposited in a predominantly marine environment (Munsterman et al., 2019). The Diessen formation, overlying the MMU, consists of sandy loam at the base and silty fine-grained glauconitic sands (Munsterman et al., 2019). The sediments at the base of the Diessen formation are marked by elevated levels of glauconite, evidenced by a notable peak in gamma-ray logs (Munsterman et al., 2019). As the mica concentrations increase upwards, the deposits show a transition from green-grey to green colors (Munsterman et al., 2019). The sediments of the Diessen Formation are deposited in a deltaic system, which is interpreted from the decrease in marine dinoflagellate cysts towards the top of this Formation and the clinoform arrangement indicating multiple phases of progradation (Munsterman et al., 2019).

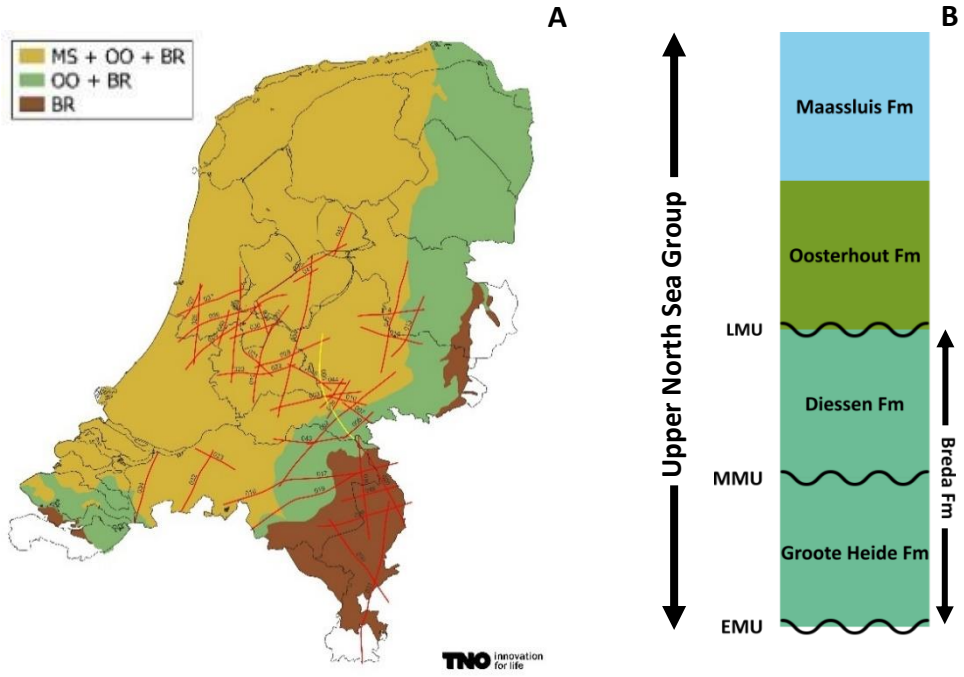

Fig. 1.5.A Presence of the Breda, Oosterhout, and/or Maassluis Formation in the Dutch subsurface. The red lines indicate the presence of SCAN 2D seismic data (EBN, TNO, & EZK, 2024; TNO, 2023b). B. Schematic overview of the Formations and unconformities within the lower part of the Upper North Sea Group. EMU: Early Miocene Unconformity, MMU: Middle Miocene Unconformity, LMU: Late Miocene Unconformity.

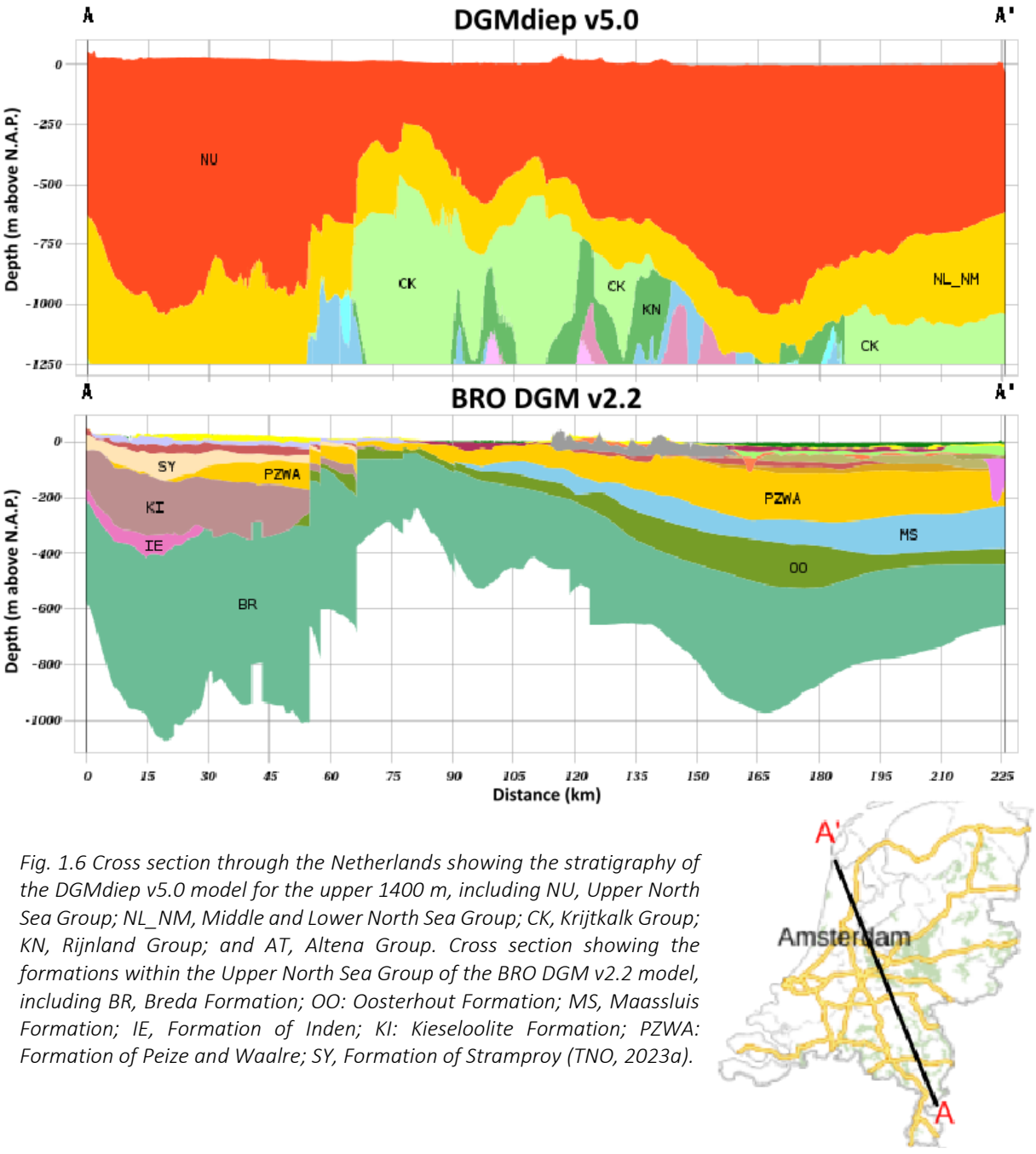

Fig. 1.6 Cross section through the Netherlands showing the stratigraphy of the DGMdiep v5.0 model for the upper 1400 m, including NU, Upper North Sea Group; NL_NM, Middle and Lower North Sea Group; CK, Krijtkalk Group; KN, Rijnland Group; and AT, Altena Group. Cross section showing the formations within the Upper North Sea Group of the BRO DGM v2.2 model, including BR, Breda Formation; OO: Oosterhout Formation; MS, Maassluis Formation; IE, Formation of Inden; KI: Kieseloolite Formation; PZWA: Formation of Peize and Waalre; SY, Formation of Stramproy (TNO, 2023a).

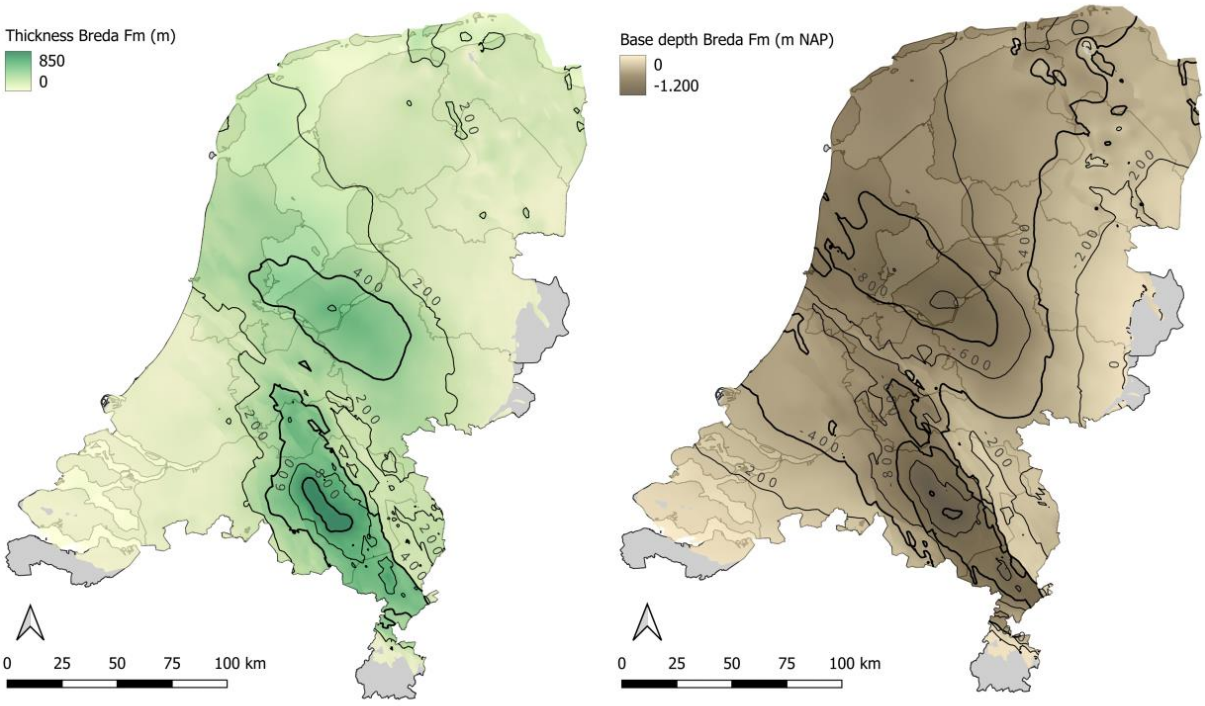

Fig. 1.7 Net thickness and Base depth of the Breda Formation based on Digital Geological Model (DGM) surfaces (TNO, 2023a).

1.3.2 Oosterhout Formation

The deposits of the Oosterhout Formation are of Zanclean-Piacenzian age and are situated above the LMU (Fig. 1.5; Vernes et al., 2023). The maximum thickness of the Oosterhout Formation occurs in the northwest of the Netherlands; the deposits are gradually thinning towards the southeast (Fig. 1.8; Vernes et al., 2023). Exhibiting a mix of often glauconitic, moderately fine- to moderately coarse-grained sands alongside shell-rich layers containing coarse sand, the Oosterhout Formation shares similar lithologies, such as the glauconitic moderately fine sands. with the Breda Formation (Vernes et al., 2023). Distinguishing between the sediments of these formations proves challenging, primarily relying on variations in glauconite and mollusk content (Munsterman et al., 2019). The sediments comprising the Oosterhout Formation show higher glauconite contents and a temporary surge in clay content, thereby yielding higher gamma-ray values (Vernes et al., 2023). The depositional environment of the sediments of the Oosterhout Formation is restricted to a (near-) coastal shallow marine environment (Munsterman et al., 2019; Vernes et al., 2023). Towards the southeast of the Netherlands the sediments of this formation become more sandy, and interconnect with the fluvial sediments of the Kiezeloöliet Formation (Vernes et al., 2023). The Oosterhout Formation can be subdivided in the Lievelde unit, characterized by fine sands, displaying a coarsening upward trend, the Sprundel unit, primarily composed of shells, and the Wouw unit, comprising grey-brown to dark grey clays (TNO, 2023a). The Goirle unit, consisting of grey to white sands, and the Tilburg unit, including glauconitic rich clayey sands, are newly proposed deposits in the Oosterhout Formation (Munsterman et al., 2019). These are positioned above the LMU and mark the base of the Oosterhout Formation. These deposits were earlier interpreted as the top of the Breda Formation (Vernes et al., 2023).

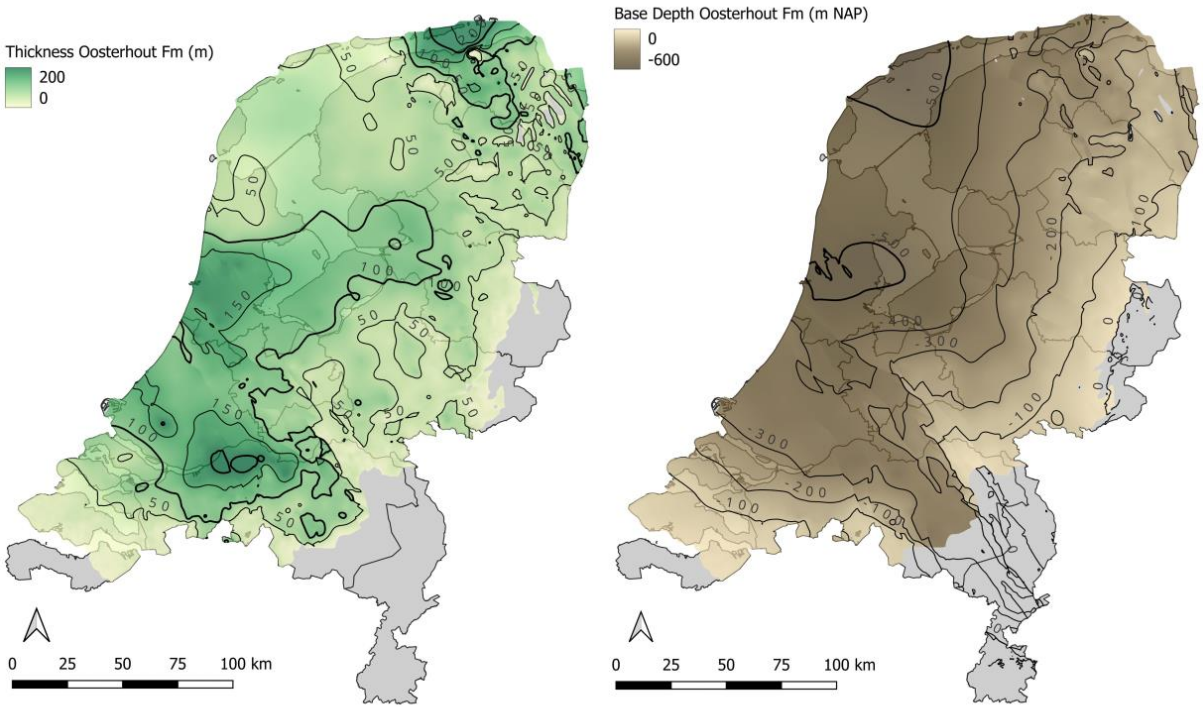

Fig. 1.8 Net thickness and Base depth of the Oosterhout Formation based on DGM surfaces (TNO, 2023a).

1.3.3 Maassluis Formation

During the Pretiglian-Tiglian period, marine sediments of the Maassluis Formation were deposited in the Netherlands (Jansen et al., 2004; Vernes et al., 2023). The formation reaches its highest thickness (~300 m) in the northwest of the Netherlands, wedging out towards the southeast (Fig. 1.6 and Fig. 1.9; Vernes et al., 2023). The Maassluis Formation consists of shell-rich, coarse-grained, generally well-sorted quartz sands, that rarely contain peat, wood remains and higher glauconite contents, and is interbedded with sandy clays or clay lenses (Vernes et al., 2023). Unlike the Oosterhout Formation, the Maassluis Formation features larger grain sizes, reduced glauconite contents and distinct mollusk assemblages (Jansen et al., 2004). These sands and clays are deposited during near-coastal marine conditions, explaining the formation's heterogeneous nature (Vernes et al., 2023). Because of the seasonal lithological alternations caused by differences in wave energy, the formation is not divided in different units (TNO, 2023a; Vernes et al., 2023). Throughout the Maassluis Formation a trend to shallower depositional environments is visible with fluviatile deposits of the Formation van Waalre overlaying the Maassluis Formation (Vernes et al., 2023). The Maassluis Formation shows limeless sands with interruptions consisting of thin clay or silt layers, as well as calcareous coarse to moderately fine sands containing shell remains. Varrying tide and wave action impact in this depositional environment, contributed to these variations, where well-sorted, coarser deposits formed during higher wave activity and deposits richer in clays during reduced wave activity (Vernes et al., 2023).

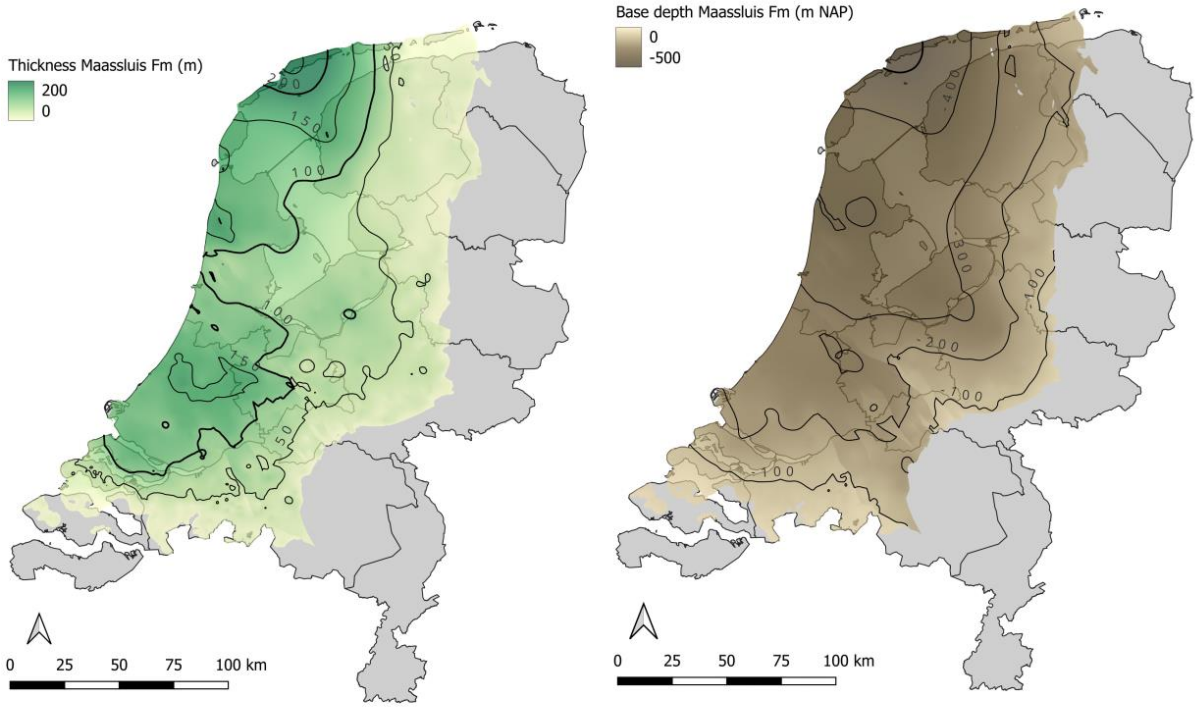

Fig. 1.9 Net thickness and Base depth of the Maassluis Formation based on DGM surfaces (TNO, 2023a).

1.3.4 Liessel core

As part of the program TopIntegraal of TNO (section 1.4) the Liessel well, B52C2133, was drilled in 2019 and the core was collected from the Roer Valley Graben in the southeast of the Netherlands (section 2.2.1 and Fig. 9.1). The core has a length of 30.0 m and mostly comprises the Breda Formation reaching from 8.0 m to 30.0 m depth (Fig. 9.1). The lithology of the Liessel core was described in detail and shows abundant silty very fine to moderately coarse sands within the Breda formation (Fig. 9.1).

1.4 Data availability

The flow rate is an important factor in the calculation of the geothermal potential (Eq. 1.1). To calculate the flow rate permeability data are necessary. Based on porosity-permeability relations, both porosity and permeability data are useful to determine the geothermal potential. A large amount of porosity data in the mid-depth range is necessary to estimate the rate of porosity reduction with increasing depth (section 1.2).

In the drilling and measuring program TopIntegraal of TNO the hydraulic conductivity of 1275 samples from the upper 30-50 m of the subsurface are measured (Buma et al., 2021). Hydraulic conductivity of sand samples are determined using a DeWit-permeameter based on the 'constant head' principle, followed by the 'falling head' principle, as stated in the European norm CEN ISO/TS 17892-11 (Buma et al., 2021). Permeability can be calculated from this hydraulic conductivity using:

$$K = \frac{k \cdot \mu}{\rho \cdot g}$$

Eq. 1.2

In which K is the hydraulic conductivity in m/s, k is the permeability of the porous medium in m^2, μ is the viscosity of the fluid in Pa·s, ρ is the density in kg/m^3, and g is the gravitational acceleration in m/s^2. Furthermore, an estimate of the total porosity is made using the difference between the dry and wet volumetric weight. The hydraulic conductivity of clay samples is determined using an oedometer based on the 'falling head' principle (Buma et al., 2021). The porosity of these samples is estimated using a gas pycnometer set-up based on the European norm CEN ISO/TS 17892-3. Combining these hydraulic conductivity estimates with interpreted lithoclasses results in a division of the subsurface in lithostrat-lithoclasses (Buma et al., 2021). These lithostrat-lithoclasses describe permeable and non-permeable layers per stratigraphic formation and are the basis of modelling the shallow subsurface in REGIS II v2.2. The water-bearing and poorly permeable layers are mapped down to a depth of approximately 500 m with locally larger depths up to 1200 m (Hummelman et al., 2019). The limitation of this model is the depth range down to an average of 500 m and the lack of hydraulic conductivity measurements with increasing depths (Kiden, 2019).

Besides this database with measured permeability and porosity values, porosity estimates can be obtained from core plugs and petrophysical data. The amount of core plugs with porosity measurements is very limited in the mid-depth range (100-1200 m).

To calculate porosity in the mid-depth range of the Breda, Oosterhout and Maassluis Formations, a combination is necessary of sonic, density, or neutron logs together with lithology and stratigraphy data (Geel & Foeken, 2021). The Dutch Oil and Gas Portal - Nederlandse Olie en Gas Portaal (NLOG), provides abundant log and stratigraphy data of the Dutch deep subsurface for deep wells, but often lacks log and detailed lithology data for the mid-depth range, as the application of these wells is mostly oil and gas exploitation (TNO, 2023b). Furthermore, the age of the wells covers a wide range with a variety of log data quality, thereby complicating comparison. Shallow wells in DINOloket contain detailed lithology data, but lack sufficient log data for the mid-depth range (TNO, 2023a). The boreholes B30G0935 (Rijswijk) and B30G4529 (Sprundel), and DAPGEO_2_500m (Delft), recent shallow geothermal and exploration wells, do provide comprehensive log and lithology data for the Breda, Oosterhout and Maassluis Formations in the mid-depth range (TNO, 2023a; Vardon et al., 2022).

Consequently, the porosity can be estimated for the mid-depth range using petrophysical data of deep wells in combination with lithology data of a nearby shallow well (section 2.1.1). Furthermore, shallow wells that include both log and lithology data can be used. When lithology data is lacking a rough estimation on lithology can be made based on REGIS II v2.2 (Hummelman et al., 2019).

1.5 Compaction

Sedimentation in combination with subsidence causes pressure and stress on subsurface sediments, because of the overburden load (Hantschel & Kauerauf, 2009). Fluid flow can decrease this overburden induced pressure, usually resulting in lower pore pressures compared to lithostatic pressures (Hantschel & Kauerauf, 2009). Compaction is defined by the reduction of the sediment bulk volume and is equivalent to volumetric strain (Hantschel & Kauerauf, 2009). Mechanical and chemical compaction decrease the porosity and grain volume due to the overburden load (Alberts, 2005; Hantschel & Kauerauf, 2009). Generally, mechanical compaction occurs in the upper 2-3 km in clastic sedimentary basins, as chemical compaction is dominant in deeper and hotter parts (Bjørlykke, 2003). Grain rearrangement, deformation and breakage, (pressure) dissolution, and cementation are

processes that encompass compaction (Alberts, 2005; Hantschel & Kauerauf, 2009; Revil, Grauls, & Brévart, 2002; Simmelink et al., 2012). Grain rearrangement involves repacking of grains under stress, leading to a decreased porosity (Alberts, 2005). Grain deformation is strongly affected by grain properties and composition. Grain fracturing has a minor effect on the compaction (Alberts, 2005). Pressure solution can result in a lower porosity and higher porosity depending on dissolution or precipitation of minerals (Alberts, 2005).

1.5.1 Chemical compaction

Chemical compaction involves dissolution of minerals in pore fluids and precipitation of new minerals in the pore spaces (He, Hajash, & Sparks, 2007). Therefore, this process can influence porosity. Chemical compaction has a minor influence on the porosity-change over the mid-depth range compared to mechanical compaction (Bjørlykke, 2003). However, there are examples of cementation and lithification within the mid-depth range in the Netherlands. Especially near the top of the Brussels Sand that ranges from 200 to 1200 m depth, thin tight calcite-cemented streaks of 20 to 200 cm are present that divide the reservoir unit (Geel & Foeken, 2021). Furthermore, drilling of a test well at Lingewaard was terminated by the presence of a lithified layer in the Breda Formation at 310 m depth (Veldkamp et al., 2021). Cementations are very rare in the limited lithology data from the Breda Formation. Moreover, in the Oosterhout and Maassluis Formation there are very limited interpretations of cementation. Consequently, chemical compaction is expected to have a minor influence on porosity-change with increasing depth for the mid-depth range.

1.5.2 Influences on mechanical compaction

The porosity evolution with increasing burial load is strongly affected by characteristics of the compacted material (Alberts, 2005). The lithology, mineral composition, grain shape, and grain-size distribution influence the course of mechanical compaction (Alberts, 2005; Chuhan et al., 2002; Dasgupta & Mukherjee, 2020; Revil, Grauls, & Brévart, 2002). An overview of porosity-depth models of shales and sandstones reveals substantial differences (Fig. 9.2). Clean sandstones typically start with initial porosities of approximately 45%. They maintain this porosity over a larger depth range during burial compared to clays. Shales begin with porosities ranging from 75% to 80%, rapidly dropping to approximately 45% within a few tens of meters of burial (Alberts, 2005). Furthermore, empirical data show less variety for shales compared to sandstones, possibly due to distinct compaction processes among these lithologies, with chemical diagenesis playing a less significant role in shales (Byrnes, 1994). A high ratio of ductile minerals, like clays and micas, compared to brittle minerals, like quartz and feldspar, in the sand, can lead to substantial porosity loss during compaction (Chuhan et al., 2002; Pittman & Larese, 1991). Therefore, the sediment mineralogy is an important influence on the compaction rate (Alberts, 2005).

Furthermore, the grain-size distribution has a large influence on the porosity (Alberts, 2005; Saul & Lumley, 2013). Introducing a larger grain into a mix of smaller grains, the large grain occupies more pore volume compared to an assemblage of smaller grains, which are separated by pore space. The addition of a larger grain, however, also loosens the packing of the smaller grains, which results in a higher pore volume. Larger size ratios amplify these effects, reducing porosity until the smaller grains can no longer fill the space between large grains (Alberts, 2005). The porosity minimum occurs when the volume of fines equals the porosity of the coarse-grained component (Fig. 1.10). Different packing models are developed to describe the relationship between the fine content and porosity (Alberts, 2005; Chuhan et al., 2002; Revil, Grauls, & Brévart, 2002).

Besides grain sorting, the grain shape is vital in packing models and eventually influence the porosity-depth relation (Domenico, 1977). Overall, coarse-grained sands experience higher porosity losses than medium- and fine-grained sands during burial (Chuhan et al., 2002). Furthermore, the critical porosity, at which a material transitions from a relatively high porosity to a more compacted state, is smaller for samples with higher clay/sand ratios (Revil, Grauls, & Brévart, 2002). Finally, grain fracturing, dependent on the grain size, grain shape, grain-size distribution, and mineralogy, has a minor influence on porosity losses in the mid-depth range, but is one of the causes of higher porosity losses for coarser-grained, lithic sands (Alberts, 2005; Chuhan et al., 2002).

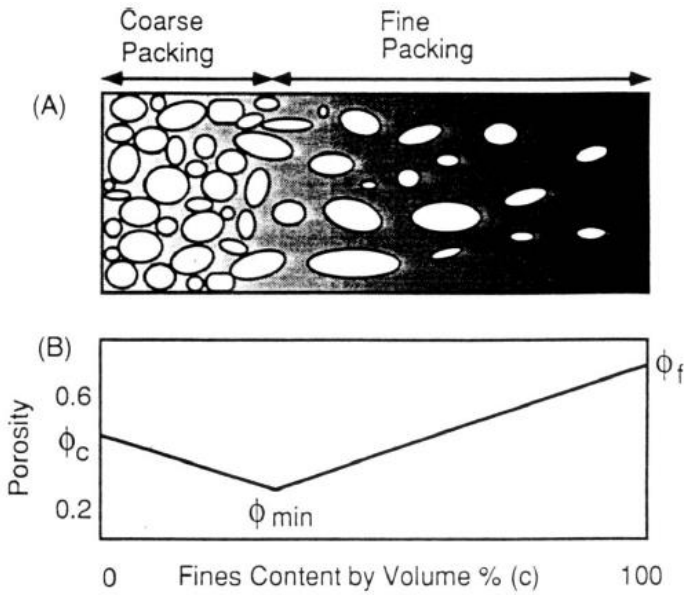

Fig. 1.10 Ideal packing model; A. Combination of natural sediments in a binary mixture. B. The predicted porosity curve (Alberts, 2005).

1.5.3 Compaction models

Various compaction models aim to explain empirical porosity-depth relationships. Athy's model (Athy, 1930), introducing a simple exponential porosity reduction with depth for the first time, is widely used in basin modelling (Hantschel & Kauerauf, 2009; Olowokere, 2011). ThermoGIS uses Athy's curve to estimate geothermal potential in cases where experimental data are not available, such as for the Upper North Sea Group (TNO, 2024).

The exponential porosity decrease against burial depth is expressed by the formula:

$$\varphi = \varphi_0 \cdot e^{-cz}$$

Eq. 1.3

in which φ is the porosity, φ_0 is the average porosity at the surface, c is a compaction constant, and z the burial depth (Athy, 1930).

A porosity asymptote can be added to the formula to include a minimum porosity value of a sediment, which will be reached at infinite depth:

$$\varphi = \varphi_0 \cdot e^{\left(-\frac{z}{L}\right)} + \varphi_\infty$$

Eq. 1.4

in which φ is the porosity, φ_0 is the average porosity at the surface, φ_∞ is the porosity asymptote, L is the decay length scale, and z the burial depth.

For adjusting Athy's curve based on porosity measurements a formula including a base porosity is used:

$$\varphi = \varphi_{\text{base}} + (\varphi_0 - \varphi_{\text{base}}) \cdot e^{(-cz)}$$

Eq. 1.5

In which φ is the porosity, φ_0 is the porosity at the surface, φ_{base} is the porosity to which the curve reaches, c is a compaction constant, and z the burial depth (Fig. 1.11; TNO, 2024).

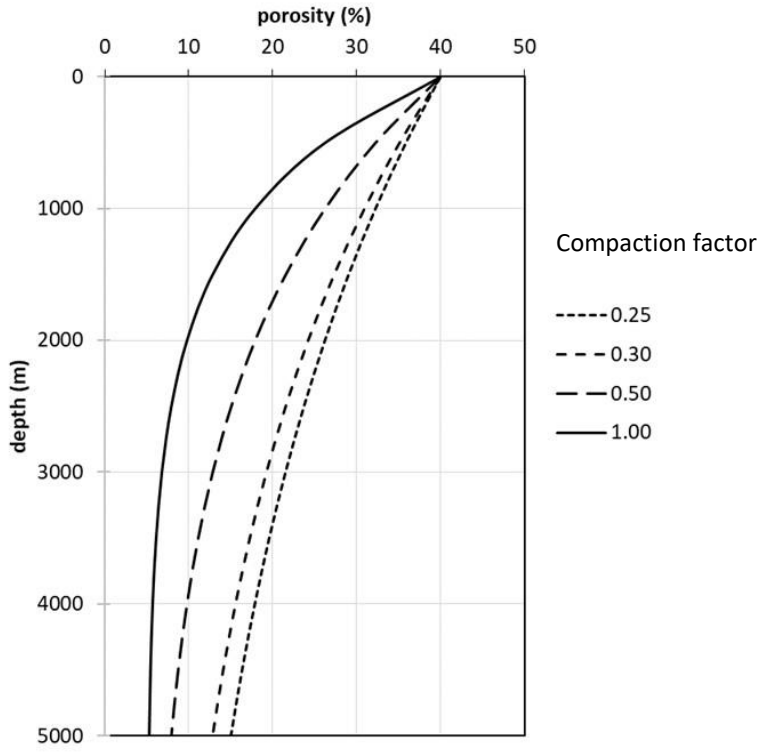

Fig. 1.11 Athy's curve for a ϕ_0 of 40%, ϕ_{base} of 5% and different compaction factors. At shallow depths porosity values estimated from Athy's curve show large differences, even with minor differences in the compaction factor. Therefore, extensive availability of porosity measurements is important to estimate an accurate curve of Athy.

The primary cause of porosity reduction is increased overburden stress, which results in intergranular fluid escape (Athy, 1930; Dasgupta & Mukherjee, 2020; Hantschel & Kauerauf, 2009). Athy (1930) used pure shale samples from Oklahoma to define an empirical relation between the porosity and depth. This model, however, does not relate the compaction degree to porosity loss or density increase, but to the increase of overburden and tectonic stresses (Dasgupta & Mukherjee, 2020). Athy's model solely relies on empirical data and does not consider (i) disequilibrium compaction in over-pressured parts of sedimentary basins, (ii) viscous phenomena, (iii) lithological and temperature variations in the sediment column, and (iv) age dependent behavior of sediments (Guy et al., 2019; Revil, Grauls, & Brévart, 2002). An older basin (> 100 Ma) shows relatively lower porosity values with increasing depth

compared to a younger basin (< 1 Ma), as more chemical compaction has occurred in old basins (Schneider et al., 1996).

The model of Schneider (Schneider et al., 1994; Schneider et al., 1996) incorporates porosity dependence on effective stress and accounts for viscous compaction phenomena, such as pressure solution, using six viscoelastic parameters. Moreover, Schneider's model permits modelling of overpressured sediments (Schneider, Burrus, & Wolf, 1993) and is expressed by the formula:

$$\varphi = \varphi_r + \varphi_a e^{-\sigma/E_a} + \varphi_b e^{-\sigma/E_b}$$

Eq. 1.6

Where φ is the porosity, φ_r is the elastoplastic residual porosity, φ_a, φ_b, E_a, and E_b are elastoplastic coefficients, and σ is the effective stress, the total stress minus the pore pressure as defined by (Terzaghi, 1925).

For most empirical data the results from Schneider's and Athy's models align (Hantschel & Kauerauf, 2009). Compaction parameters of carbonate rocks and clastic sediments have been compiled from various studies and experimental work by Doug Waples (Table 9.1; Table 9.2; and Table 9.3; Hantschel & Kauerauf, 2009). Empirical porosity data on unconsolidated sands for defining the compaction parameters in different models are available (Chuhan et al., 2002). However, a comprehensive predictive deterministic compaction model for unconsolidated sand is not available, because of the large amount of influencing processes, such as grain rearrangement, grain deformation and fracturing, pressure solution, cementation and diagenetic processes (Alberts, 2005; Chuhan et al., 2002).

The analytical model by Giles (1997) differs from the effect-oriented models discussed above by encompassing every process that might reduce porosity (Alberts, 2005). This model can be simplified as:

Rate of porosity loss = rate of elastic strain + rate of mechanical creep + rate of pressure solution + rate of plastic deformation of ductile grains – rate of change of solid volume

Eq. 1.7

(Alberts, 2005; Giles, 1997). However, the drawback of this model is the necessity for numerical solutions and the requirement of a rock burial history (Alberts, 2005).

The complexity of compaction models increases, as more factors influencing the compaction process are studied. More empirical data, especially for unconsolidated sands, are necessary to further develop the compaction models and indicate their quality.

1.5.4 Porosity – acoustic wave velocity relation

Based on the relation between the porosity and acoustic wave velocity, porosity can be calculated from sonic log data, which include the acoustic wave slowness (section 2.1.3). Acoustic wave velocities are influenced by (i) the rock framework, density of grains, type of cementing material, pressure on skeleton, lithology and porosity, (ii) density, pressure and compressibility of the pore fluid, and (iii) the temperature of the medium (Hicks & Berry, 1956). As seismic reflection technology has improved over the years and is widely used in aquifer characterization, the potential to extract flow properties of sediments from these data has increased (Zimmer, 2004). Compaction results in an increase of p-wave

velocity (Fig. 1.12 and Fig. 1.13; Doornenbal et al., 2022; Zimmer, 2004). There is a limited increase in pressure-wave velocity with decreasing porosity (Fig. 1.12) and almost no change in shear-wave velocity with decreasing porosity (Zimmer, 2004). Measured pressure-wave velocities of water-saturated samples show a larger sensitivity to porosity compared to dry samples (Zimmer, 2004). The pressure-wave velocity can therefore be used to estimate porosity in the subsurface (section 2.1.3). Especially for the North Sea Group the interval velocity shows a lower increase with higher mid-depths compared to other (older) lithostratigraphic groups (Doornenbal et al., 2022).

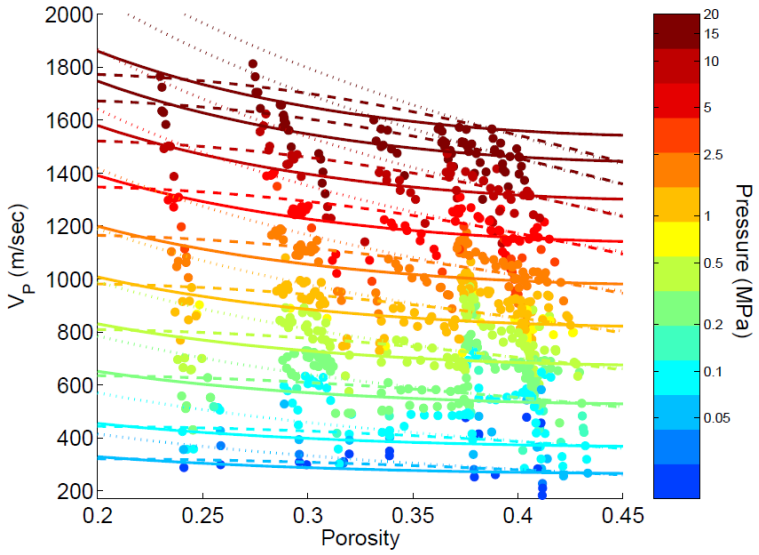

Fig. 1.12 Compressional wave velocity data measured by Zimmer (2004) against the porosity. Colour-coding is displayed on the right-hand side for pressure of different samples of dry and wet unconsolidated sands.

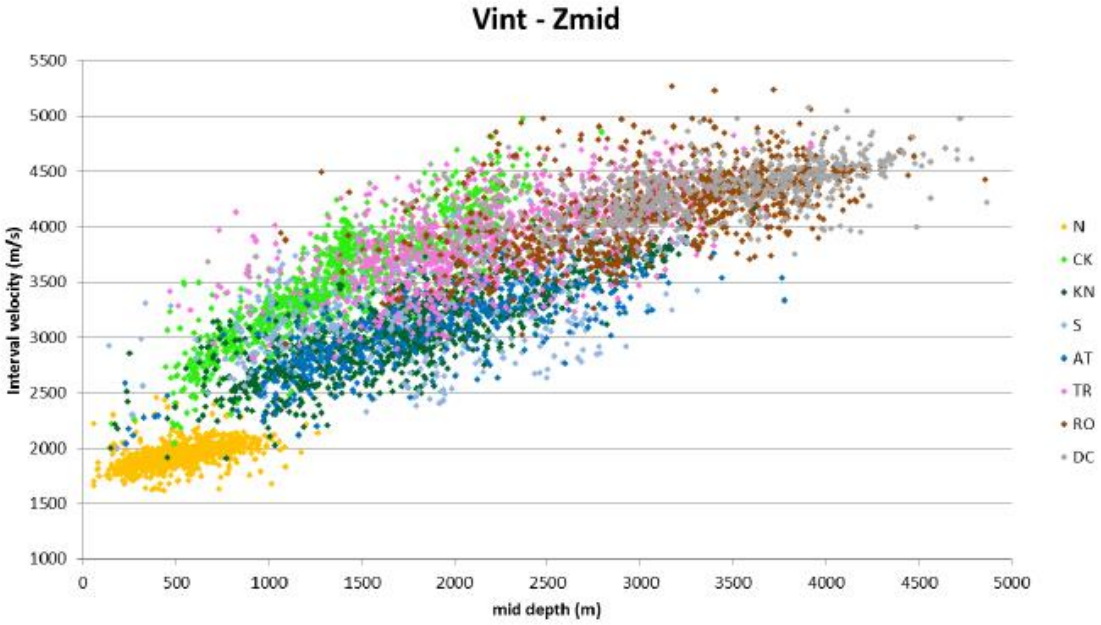

Fig. 1.13 Interval velocity against the mid depth of each main lithostratigraphic group. In order of increasing age: N: North Sea Group, CK: Chalklime Group, KN: Rhineland Group, S: Upper Jurassic Group, AT: Altena Group, TR: Triassic Group, RO: Rotliegend Group, DC: Limburg Group. From (Doornenbal et al., 2022)

2. Methods

Porosity can be calculated from sonic and density log data. However, the influence of compaction on porosity estimates calculated from log data introduces large uncertainties in these calculations. Porosity values show variations over a depth range because of lithology changes and compaction. Due to the lack of core plug data for the mid-depth range porosity estimates cannot be calibrated, and large uncertainties remain. Results of compaction experiments are combined with measured porosity and grain size distribution data of the core, from where samples were extracted, to evaluate porosity measurements. These experimental porosity estimates are compared to the results from porosity calculations to further assess the quality of the porosity estimates. Finally, these porosity estimates can be used as a proxy for the permeability (k), which is used to calculate geothermal potential of aquifers.

2.1 Processing of available data

Wells that contain both detailed lithology data, log data and porosity data from core plugs for the Breda, Oosterhout and/or Maassluis Formations in the mid-depth range are extremely rare. Therefore, combining wells with log data and lithology data to calculate and validate porosity estimates is necessary. Deep wells mostly include log data and lack high quality lithology data, as shallow wells mostly contain lithology data, but no log data. Therefore, the available data were combined, by matching lithology data of shallow wells to log data of nearby deep wells. Furthermore, porosity was calculated from applicable log data of selected deep wells to obtain indicative porosity-depth relations across various lithologies within these formations.

2.1.1 Selection combinations shallow and deep wells

Because of the lack of wells containing both detailed lithology and log and data, nearby deep and shallow wells were selected to combine their data. Selection criteria included:

- Deep wells that have sonic or density data within the mid-depth range (100-1200 m),
- Deep wells that were drilled after 1980,
- Sonic data of the deep wells are of good quality,
- The shallow wells include the Breda, Oosterhout and/or Maassluis Formations,
- The shallow wells show detailed stratigraphy and lithology data,
- The distance between deep and shallow wells is less than 1500 m,
- The sonic data of the deep well overlap with depths where the Breda, Oosterhout and/or Maassluis Formations are present,
- The log data of the deep wells match with stratigraphy and lithology differences of the shallow wells.

Using SQL Developer all deep wells including sonic and density logs and shallow wells covering the Breda, Oosterhout and/or Maassluis Fm's were extracted from the TNO subsurface database (TNO, 2023a, 2023b). QGIS facilitated addition of Breda, Oosterhout Maassluis Formation tops and surface elevation of the Netherlands - Actueel Hoogtebestand Nederland (AHN) – values to each well by

sampling raster values from the Digital Geological Model (DGM) surfaces of these formations. Deep wells with sonic logs that overlap the Breda, Oosterhout and/or Maassluis Formations were then selected using the following rule in the query builder:

"acoustic_from" > 0 AND (("acoustic_from" - "AHN1") < ("BR-T1" * -1) OR ("acoustic_from" - "AHN1") < ("OO-T1" * -1) OR ("acoustic_from" - "AHN1") < ("MS-T1" * -1))

“acoustic from” and “acoustic to” are variables that refer to the depth range along which acoustic (sonic) logs were recorded. “acoustic_from” > 0 was added to account for errors in the database and to eliminate deep wells without sonic data. “Acoustic_from” is the top of the sonic data and is corrected to the Normal Amsterdam sea-level - Normaal Amsterdams Peil (NAP) – by subtracting the AHN. The top of the sonic should be lower than the top of the Breda, Oosterhout and/or Maassluis Formations to allow for overlap. The BR-T1, OO-T1 and MS-T1 are the formation tops; they are multiplied by -1 to compare to the positive sonic top data.

This selection using the query builder in QGIS was also performed for density logs:

"density_from" > 0 AND (("density_from" - "AHN1") < ("BR-T1" * -1) OR ("density_from" - "AHN1") < ("OO-T1" * -1) OR ("density_from" - "AHN1") < ("MS-T1" * -1))

A buffer of 1500 m was made in QGIS around the selected deep wells. The deep wells and the shallow wells were then selected, where the shallow wells intersect this buffer. The deep wells with drilling ages after 1980 were selected from this pool to increase the chance of extracting good logging data. Because of potential errors in the dataset, the presence of sonic and density data was checked and deep wells without suitable sonic and/or density data were eliminated. This relates, for instance, to wells where a sonic and/or density log was recorded in the correct depth interval, but the readings were considered unreliable after visual inspection (Fig. 2.1). Finally, 13 deep wells were selected: BKH-01, BLF-106, DRT-01, HBV-01, JPE-01, KTG-01, NWK-02, RLO-01, SCH-2952, SPKO-02, STH-01, VAL-01 and WDL-01 (Fig. 2.3).

2.1.2 Quality control of selected shallow and deep well sets

The combined deep wells and shallow wells were compared in Petrel, evaluating the set’s quality, based on interpreted stratigraphy depths, gamma-ray, sonic and density log alignment with the interpreted lithology of the shallow well, and their proximity (Table 9.4). This results in 7 remaining combinations of deep and shallow wells: HBV-01 - B44G0232, JPE-01 - B33F0115, JPE-01 - B33F0116, KTG-01 - B48E0081, NWK-02 - B30F0470, RLO-01 - B34D0223, and WDL-01 - B28B0143 (

Fig. 2.3). Furthermore, shallow wells B30G4529 and B49F0378, and a recently drilled well at Delft, DAPGEO-02_500m (Vardon et al., 2023), including lithology and sonic data were selected. The porosity was calculated from the sonic and density data of the deep wells and recently drilled wells to allow for comparison with different stratigraphy’s and lithologies from the shallow wells (section 2.1.3).

2.1.3 Porosity calculation

The effective porosity can be calculated from neutron, density, resistivity and sonic logs using a shaly-sand model (Geel & Foeken, 2021). A combination of a neutron and density log is preferred to calculate the effective porosity. However, for the selected mid-depth range, no neutron log data were available for wells overlapping the Breda, Oosterhout, or Maassluis Formations. Therefore, the best porosity estimates were calculated from the density logs, which are the next best choice to calculate effective porosity (Geel & Foeken, 2021). Finally, sonic log data were used to calculate porosity, as these were

most frequently available in the mid-depth range. When both density and sonic logs were accessible, the porosity calculations based on the sonic log were corrected by optimizing the fit in a cross-plot with both calculations (section 3.1.2). The difference between effective and total porosity should be considered; the total porosity includes the total volume of pore spaces within a sediment, as the effective porosity only includes the interconnected pore spaces, which can transmit fluids (Fig. 2.2). Pure sands generally have similar total and effective porosities, but when clay is added, the effective porosity is generally lower compared to the total porosity. Porosity calculation based on log data results in estimates on the effective porosity (Geel & Foeken, 2021).

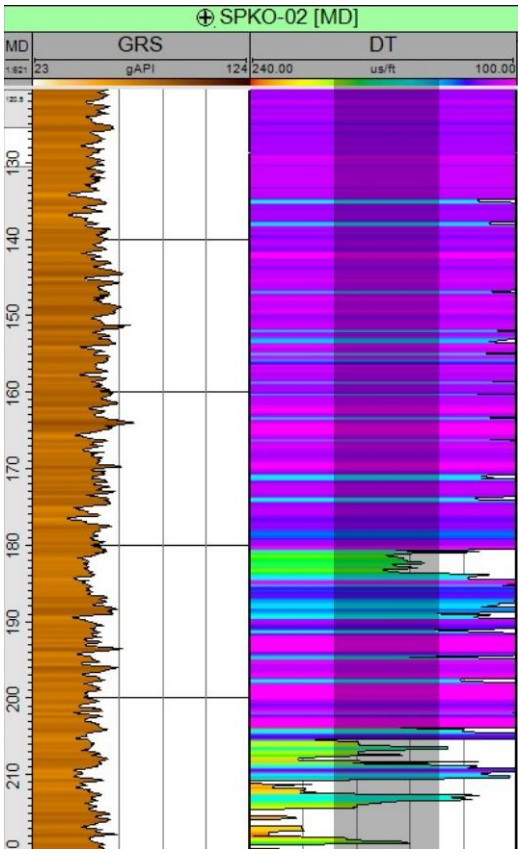

Fig. 2.1 Example of a sonic log, including sonic slowness (DT) that is considered unreliable, because of the unusually low values and the large fluctuations. The black transparent rectangle shows the range of sonic slowness values, expected in high-quality sonic log data.

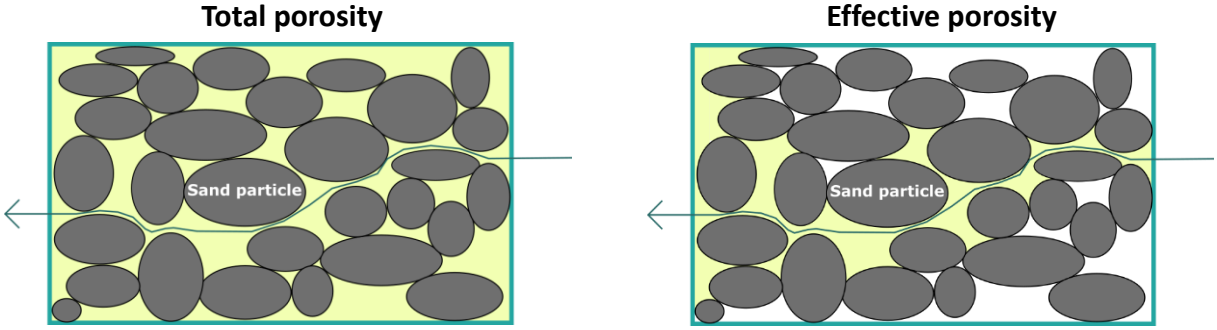

Fig. 2.2 Total porosity includes all pore spaces of the sediment (yellow). Effective porosity only includes interconnected pore spaces, that can transmit fluids (yellow).

Fig. 2.3 Locations of the selected deep and shallow well combinations, the Rijswijk (B30G4529), Sprundel (B49F0378), Delft (DAPGEO_2_500m) and Liessel well (B52C2133).

Well	Name	Spud year	Available logs	Strat overlap
HBV-01	Huibeven-01	2002	GR SON	BR OO MS
JPE-01	Joppe-01	1985	GR SON RHOB	BR OO
KTG-01	Kortgene-01	1982	GR SON RHOB	BR OO MS
NWK-02	Noordwijk-02	1983	GR SON	BR OO
RLO-01	Ruurlo-01	1984	GR SON RHOB	BR OO
WDL-01	Wierden-Loo-01	1998	GR SON	BR OO
B30G4529	Rijswijk (Shell test hole)	2008	GR SON RHOB	OO MS
B49F0378	Sprundel	1989	GR SON	BR OO
DAPGEO_2_500m	Delft	2022	GR SON	BR OO MS

Table 2.1 Overview of the well name, spud year, available logs, GR: Gamma Ray, SON: Sonic slowness, and RHOB: density, and the presence of the Breda (BR), Oosterhout (OO), and/or Maassluis (MS) Formations within the depth range, where log data are present (TNO, 2023a, 2023b).

Effective porosity from the sonic log

The fundamental Wyllie formula (Wyllie, Gregory, & Gardner, 1956) is used to calculate the (sonic) effective porosity (m^3/m^3) based on the sonic log. This equation is formulated for compacted clean sands at high depths and should therefore be corrected for compaction and lithology variations when applied to unconsolidated sediments that can include clay for the shallow mid-depth range (Geel & Foeken, 2021). This results in the following formula:

$$\varphi_{\mathrm{son}}^{\mathrm{e}} = \left(\frac{\mathrm{DT} - \mathrm{DT_{ma}}}{\mathrm{DT_{fl}} - \mathrm{DT_{ma}}} - \mathrm{V_{cl}} \cdot \frac{\mathrm{DT_{sh}} - \mathrm{DT_{ma}}}{\mathrm{DT_{fl}} - \mathrm{DT_{ma}}}\right) \cdot \frac{1}{\mathrm{C_p}}$$

Eq. 2.1

$$\mathrm{C_p} = \frac{\mathrm{DT_{sh}}}{\mathrm{DT_{csh}}}$$

Eq. 2.2

(Geel & Foeken, 2021; Wyllie, Gregory, & Gardner, 1956)

In which DT is the sonic slowness of the deep well (µs/ft), DT_{ma} is the matrix slowness (µs/ft), DT_{fl} is the fluid slowness (µs/ft), V_{cl} is the clay volume, DT_{sh} is the shale slowness (µs/ft) C_p is the compaction factor, and DT_{csh} is the compacted shale slowness. Eq. 2.1 is an adaptation of the fundamental Wyllie porosity formula, adjusted to account for variations in clay content and compaction. The compaction factor is calculated based on the ratio of the sonic slowness of an underlying shale layer and a standard compacted shale slowness of 100 µs/ft (Eq. 2.2).

The clay volume is determined from the gamma-ray (GR) log with the formula:

$$\mathrm{V_{cl}} = \frac{\mathrm{GR} - \mathrm{GR_{min}}}{\mathrm{GR_{max}} - \mathrm{GR_{min}}}$$

Eq. 2.3

In which GR is the gamma-ray at a specific depth, GR_{min} is the minimum gamma-ray for clean sandstones, and the GR_{max} is the maximum GR for pure shales, which were both indicated from the GR logs for well-known stratigraphy's (Geel & Foeken, 2021). For the calculated effective porosities, the GR_{max} and GR_{min} were selected from logs covering the Breda, Oosterhout, and Maassluis Formation, preferably with lithology information of the nearby shallow well. The GR_{max} is picked from clay layers and the GR_{min} from sand layers.

The DT_{sh} was selected from well-known underlying shale layers, such as the Veldhoven clay member, the depositional unit of Boom/Rupel clay member, and Oosterhout Formation for the shallow wells. For the selected deep wells the standard quartz value of 56 µs/ft is used for DT_{max} and DT_{csh} is set to 100 µs/ft (Geel & Foeken, 2021). The DT_{fl} does not only depend on the salinity of the formation fluid, but also on the salinity of the mud. During drilling of the well the mud filtrate invades the formation and replaces the original formation water. The sonic log therefore includes signals of the mud filtrate which influences DT_{fl}. In most drilling reports the salinity of the mud filtrate is not described (Table 9.5) and should be calculated using the mud filtrate resistivity and formation temperature:

$$C_w^{0.955} = \frac{166164}{R_f T_f + 21.6667 R_w - 0.560333}$$

Eq. 2.4

In which C_w is the salt concentration (ppm), R_w is the mud filtrate resistivity (Ωm) and T_f is the formation temperature (°C) (Akinsete & Adekoya, 2016). The DT_{fl} was then derived from the salinity of the mud filtrate using Table 2.2 and the R_w and T_f of the selected wells (Table 9.5). When no salinity data is present or can be calculated a DT_{fl} of 218 is picked, as mostly freshwater bentonite is used as drilling mud for the relatively shallow depths.

Salt concentration (ppm)	DT_{fl} (µs/ft)	ρ_{fl} (g/cm^3)
0	218	1.0
2,000	216	1.0
4,000	214	1.0
6,000	212	1.0
8,000	210	1.0
10,000	208	1.0

Table 2.2 DT_{fl} (ppm) and ρ_{fl} (g/cm^3) for different salt concentrations of the mud filtrate (Carmichael, 1989; Lyons, 2010).

Effective porosity from the density log

Porosity can be calculated from the density log with the formula:

$$\varphi_\rho = \frac{\rho_{ma} - \rho_b}{\rho_{ma} - \rho_{fl}} - V_{cl} \cdot \frac{\rho_{ma} - \rho_{sh}}{\rho_{ma} - \rho_{fl}}$$

Eq. 2.5

In which φ_ρ is the density porosity in (cm^3/cm^3), ρ_{ma} is the matrix density, which is set as the quartz density of 2.65 g/cm^3 for these calculations, ρ_b is the measured bulk density from the log (g/cm^3), ρ_{fl} is the fluid density (g/cm^3) , which depends on the mud salinity (Table 2.2), and V_{cl} is the clay volume. The porosity calculations based on density logs include lower uncertainties compared to the sonic log-based estimates, because the density effective porosity does not have to be corrected for compaction. The compaction factor to calculate sonic porosity is therefore corrected based on a cross-plot of the sonic against density porosity estimates, when both sonic and density log data are present (Geel & Foeken, 2021).

2.2 Compaction experiment

To validate the porosity estimates from sonic calculations, a compaction experiment was performed to simulate overburden load and indicate porosity at various depths for different lithologies (Fig. 2.4). First, samples were selected and prepared for a uni-axial stress-strain device measurement. Then, the initial porosity was measured, and CT-scans were performed prior to compressing the individual samples. Finally, the samples were exposed to an overburden pressure up to 21.2 kN, simulated by increasing the load of the uni-axial stress-strain device. After the application of pressure, porosities were measured, and CT-scans were performed again to observe any changes in the sample structure.

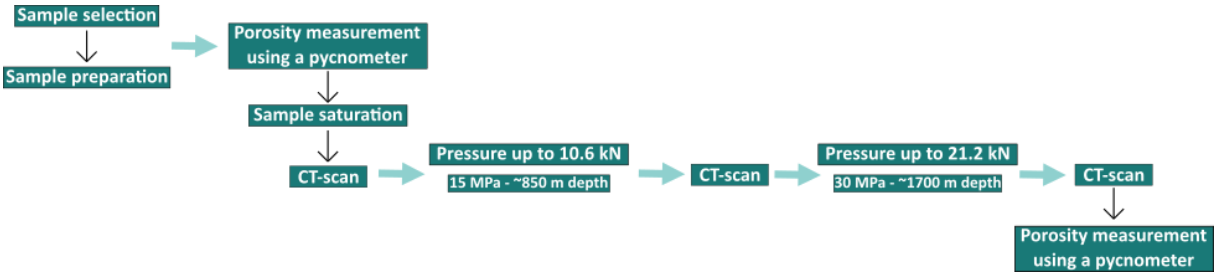

Fig. 2.4 Schematic overview of the steps performed in the compaction experiments.

2.2.1 Sample selection

Five samples were obtained from the 30.0 m long core, from well B52C2133 (Liessel), which includes the Breda Formation from 8.0 m to 30.0 m (Fig. 9.1). The samples were sawn out perpendicular to the core, each ranging between 10.0 and 16.0 cm in length, to use in the compaction experiment (Fig. 2.5). The criteria for selection include variations in sand, silt and lutum percentage, the M63 - the median grain size of the sand fraction in µm, and in the glauconite content (Table 2.3). Within each sample the heterogeneity is very limited with the exception of sample 5 (Table 2.3). The Breda Formation in the Liessel core lacks clay, which decreases the diversity in lithologies of the core. However, the sands that were sampled, include more than 90% grains with a size between 0.063 mm and 2 mm and show small differences in silt, lutum and glauconite percentages (Table 2.3; Das, 2016). Sand, silt and lutum size ranges are defined according to NEN5104 (Fig. 9.6).

Sample	Lithology	Depth range (cm)		M63	LU (%)	SI (%)	ZA (%)	GR (%)	OR (%)	CA (%)	GLAU (%)	Fm
		Top	*Base*									
1	Sand	847	860	170	0	2	98	0	0	1	1 a 2	Breda
2	Sand	1675	1691	170	0	1	99	0	0	1	6	Breda
3	Sand	2188	2200	200	0	2	98	0	0	1	3	Breda
4	Weakly silty sand	1582	1593	160	3	5	92	0	0	1	2	Breda
5	Weakly silty sand (2789-2793 cm)	2789	2800	180	1	3	96	0	0	1	6	Breda
	Glauconitic sand (2793-2795 cm)				1	2	62	35	0	1		Breda
	Silty sand (2795-2800 m)			160	1	14	85	0	0	1	6	Breda

Table 2.3 Overview of selected samples of the Liessel core, B52C2133, showing M63 – the median grain size of the sand fraction in µm -, lutum (<2 µm) percentage (LU), silt (2-63 µm) percentage (SI), sand (63 µm – 2 mm) percentage (ZA), gravel (2-63 mm) percentage (GR), organic material percentage (OR), carbonate percentage (CA), glauconite percentage (GLAU) and formation (Fm) based on the core description. It should be noted that the M63 and percentages are visual estimates and not machine-measured data.

2.2.2 Sample preparation

The samples will be placed in the uni-axial stress-strain device in between two pressure pieces of approximately 3.0 cm, which will transmit pressure onto the samples (section 2.2.6). The sample diameter must be 3.0 cm to fit into this stress-strain device, and the sample length is required to be at least double the size of the pressure pieces. Consequently, for this experiment the minimum sample length is 6.0 cm. Initially a sample length of 7.0 cm was chosen, considering the effects of compaction and the minimum sample length. After preparation of the sample the sample length eventually became

7.4 cm, because of difficulties in protruding and transporting the sample. To contain the unconsolidated samples and minimize horizontal deformation, an aluminium casing surrounding the sample was used. Subsequently, porosity can be calculated during increasing pressures, as the vertical displacement of the pressure pieces is measured. The aluminium casing has a length of 7.4 cm, an inner diameter of 3.0 cm, and an outer diameter of 3.5 cm (Fig. 2.7.A). Aluminium was selected for the casing, because it offers strength (to prevent deformation) and allows the X-rays to penetrate during CT-scanning. The samples were extracted from the pieces core using an aluminium pipe with an inside diameter of 3.0 cm and an engraved line at 7.0 cm length (Fig. 2.7.E and Fig. 2.6.A). The sharp edge of the pipe facilitated cutting through the sediments. The 7.0 cm line on the protruding pipe indicates up to where the sand should be cut to fit in the aluminium casing (Fig. 2.6.B). After the pipe was pushed into the sand, a knife was used to cut the sediment at the base of the pipe and hence loosen the sand to allow sample collection in the pipe (Fig. 2.6.C). In practice, the sand collected within the protruding pipe slightly exceeded 7.0 cm. The aluminium casing can be attached to the protruding pipe by an inlet in the aluminium casing of 2.0 mm, to simplify the transfer of the sand into the aluminium casing (Fig. 2.7.A/E). With a push device the sample is removed from the protruding pipe into the aluminium casing (Fig. 2.7.F-H and Fig. 2.6.D-E). A 5 cm^2 piece of parafilm was added to one side of the aluminium casing to prevent the sand from falling out (Fig. 2.7.B-C). Two small holes were made in the parafilm to facilitate the movement of the sand and the push device into the aluminium casing. Because of the somewhat longer protruded samples, the sand sticking out of the aluminium casing was scraped off with a knife. This sampling procedure results in a final sample length of 7.4 cm. Before measuring the porosity of the sample using the pycnometer, the samples were left to dry overnight in an oven at 60 °C. Once removed from the oven, the parafilm was broken and therefore replaced with a new piece of 5.0 cm^2.

Fig. 2.5 The sawn out sample locations of samples 1-5 (white boxes) in an overview of core B52C2133 located in Liessel (Fig. 2.3). Sample 1: 847-860 cm (box 1); sample 2: 1675-1691 cm (box 2); sample 3: 2188-2200 cm (box 3); sample 4: 1582-1593 cm (box 4); sample 5: 2789-2800 cm (box 5). The top of the core is visualized by the upper left image and the bottom by the lower right image. Reddish parts contain more iron.

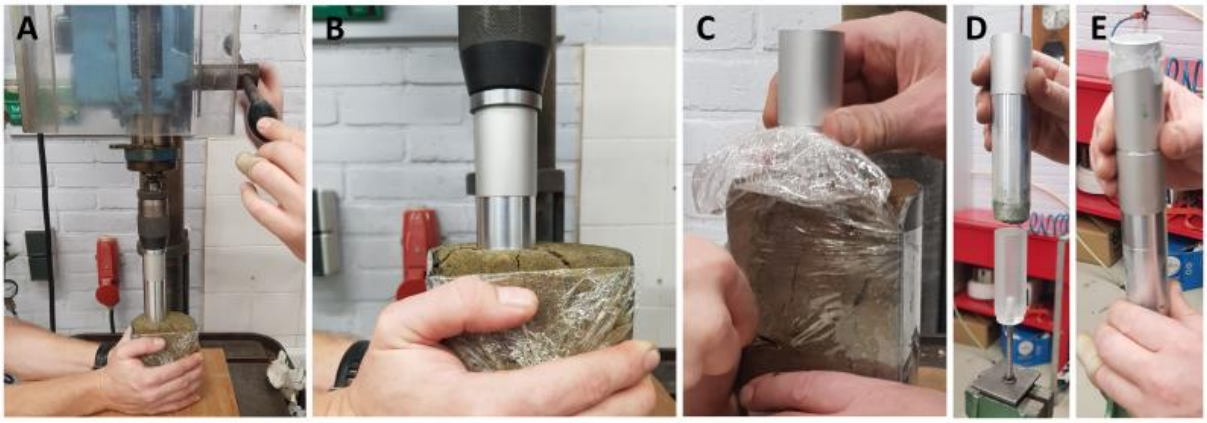

Fig. 2.6 Overview of the steps to fill the aluminium casing with sand. A. Set-up to push the sand in the protruding pipe. B. The sand was pushed until the 7.0 cm line on the protruding pipe. C. With a knife the sand was cut at the point to where the protruding pipe reaches. D. The filled protruding pipe was placed above the push device. E. The aluminium casing was put on the protruding pipe and the sand was pushed in this casing.

Fig. 2.7 A. Aluminium casing. B. Parafilm piece. C. Aluminium casing with parafilm on one side. D. Orientation of the aluminium casing, when filled with sand. E. Aluminium protruding pipe. F. Push device. G. Push device in protruding pipe. H. Overview of the complete line-up to get a sample in the aluminium casing.

2.2.3 Pycnometer

A pycnometer measures the matrix volume, which is the grain volume of a sample, based on volume differences in helium between a reference chamber and sample chamber (Fig. 4.5). When a sample has high porosity, a large amount of helium can penetrate in between the grains of the sample. When porosity is high, the ratio between the volume of helium in the sample chamber and the helium volume in the reference chamber is also high. Based on this ratio of helium volume the pycnometer gives the matrix volume of the sample as output. The pycnometer Ultrapyc 3000 is used in this study. The porosity can be calculated from the measured matrix volume using the formula:

$$\text{Porosity} = \frac{\text{Total volume}_{\text{sand}} - \text{Matrix volume}_{\text{sand}}}{\text{Total volume}_{\text{sand}}} \times 100$$

Eq. 2.6

The total volume of the sand was calculated from the inner diameter of the aluminium casing and the length of the sand with the following formula:

$$\text{Total volume}_{\text{sand}} = \text{r}^2 * \pi * \text{L}$$

Eq. 2.7

Given that the aluminium casing's inner diameter is 3.0 cm and the length of the sand sample is 7.4 cm, the total sample volume computes to 52.3 cm^3. However, the aluminium casing was included in the measurement of the matrix volume by the pycnometer. Therefore, the matrix volume of the aluminium casings was measured separately without sample. As there are no pores in aluminium, the matrix volumes correspond to the total volume of the aluminium casing. The measured matrix volume of the aluminium casings is used to correct the measurements of the sand-containing aluminium casings:

$$\text{Porosity} = \frac{\text{Total volume}_{\text{sand}} - \text{Matrix volume}_{\text{sand in aluminium casing}} + \text{Matrix volume}_{\text{aluminium casing}}}{\text{Total volume}_{\text{sand}}} \times 100$$

Eq. 2.8

Furthermore, the influence on the sample's matrix volume of the parafilm at the bottom of the aluminium casing was evaluated. Addition of the parafilm led to a significantly higher porosity outcome of 0.6% for aluminium casing 1. Therefore, porosity data calculated for the sand-containing aluminium casings with parafilm were also corrected for the presence of parafilm. The matrix volume was measured twice of an aluminium casing adding different pieces of parafilm of 5.0 cm^2 to assess consistency, resulting in a porosity difference of 0.02%. As the parafilm was replaced after drying in the oven and CT-scanning, and variations in parafilm layers of 5.0 cm^2 resulted in a negligible porosity difference (±0.02 %), matrix volumes of the aluminium casings were all measured in combination with consistent 5 cm^2 parafilm folded over. The matrix volume of samples 1-5 in the aluminium casing were then measured. Finally, porosity values were calculated from the matrix volumes of the aluminium casings with parafilm, containing sand, and solely the aluminium casing with parafilm using Eq. 2.8.

2.2.4 Sample saturation

To achieve full saturation of the samples, nettings featuring pores of 82x82 µm were attached to both sides of the samples with tie wraps to prevent sand loss (Fig. 2.8.A). The samples were each put in a separate tray to catch sample that might escape during saturation. The samples were put in one container and the other container was filled with tap water (Fig. 2.8.B). Both the tap water and samples

were pumped vacuum using a KNF Laboport vacuum pump (N 840.3; FT.1 8 G; 20 L/min) for 1 hour (Fig. 2.8). Hereafter, the sample container was filled with vacuumed water from the bottom, gradually covering all samples. Then, the water-filled sample container was vacuum pumped for 1 additional hour. The samples were left in the vacuumed water overnight for complete saturation. After saturation the samples were CT-scanned and stored with two pieces of parafilm on the top and bottom in a refrigerator.

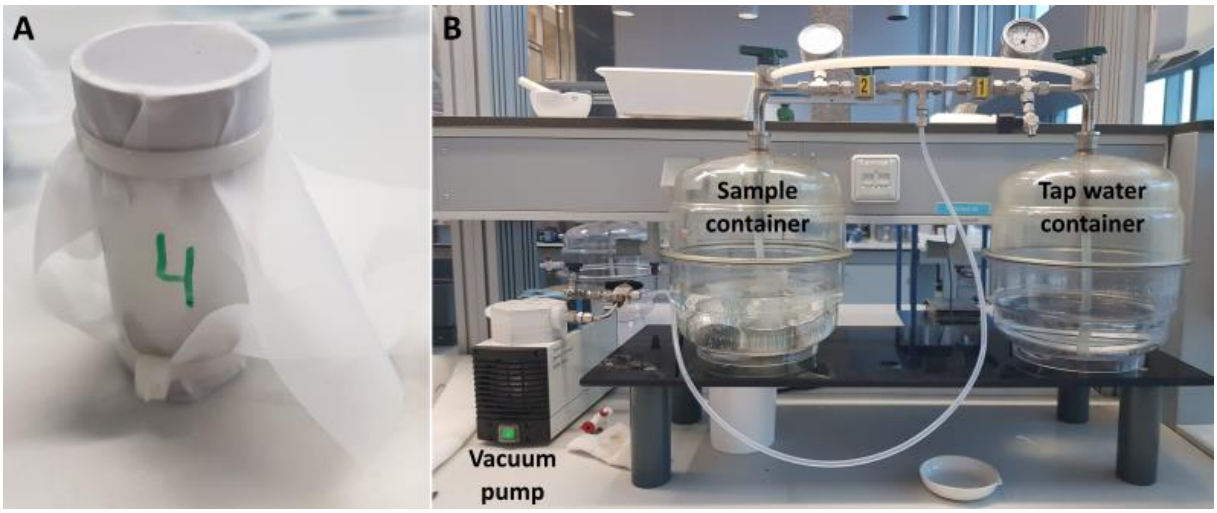

Fig. 2.8 A. Netting attached at bottom and top of sample. B. Saturation set-up with the KNF Laboport vacuum pump, the container with the samples in trays and the container with tap water.

2.2.5 CT-scanning

CT-scans were measured using the TESCAN CoreTOM MicroCT scanner in the Laboratory of Geoscience and Engineering of the Technische Universiteit Delft (TU Delft, Delft University of Technology). Test-scans were performed to assess if porosity could be calculated based on CT-scans. The best image quality was obtained using a high-spatial resolution and high-source voltage. However, the scanning duration increases fast with higher spatial resolution and source voltage. As the highest spatial resolution of 12 µm and X-ray source voltage of 100 kV, were still insufficient to clearly distinct different grains from the CT-scan, a spatial resolution of 25.0 or 27.5 µm and X-ray source voltage of 100 kV were used to reduce the scanning duration to approximately 7 minutes. The power of the CT-scanner was set to 25 W, exposure to 34.00 ms, and 1440 projections were taken per sample. Before CT-scanning, a vertical line was drawn on the samples to secure similar sample orientation during every CT-scan (Fig. 2.9). Therefore, the CT-scans for the different pressure stages can be easily compared with each other. It should be noted that similar orientations of the samples during different pressure stages were eyeballed and could therefore show minor differences. The saturated samples were placed in aluminium cups, which were folded around the sample to prevent leakage of water from the saturated samples in the CT-scan (Fig. 2.9). CT-scans were performed before stress was applied to the samples, and with 15 MPa and 30 MPa stress regimes.

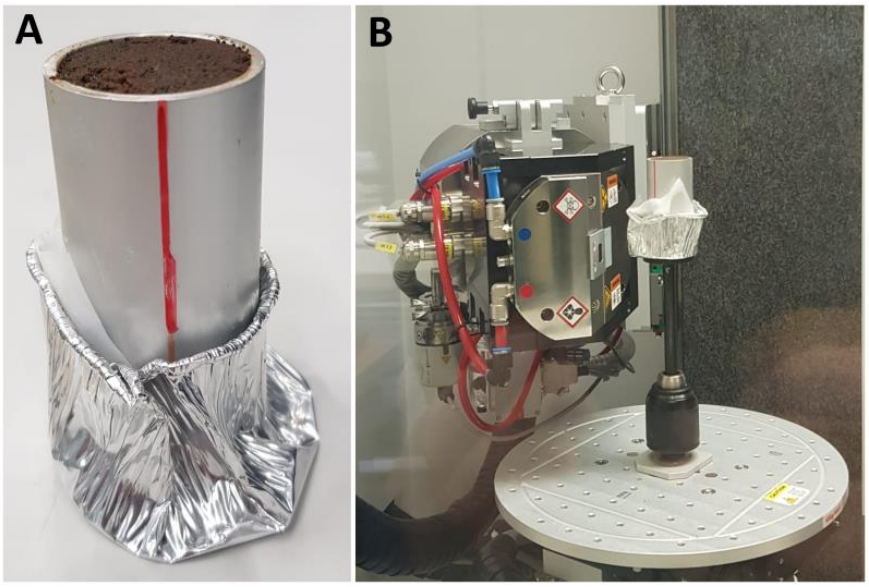

Fig. 2.9 A. Sample before CT-scanning with a vertical line for orientation and an aluminium cup to prevent leakage of water in the CT-scanner. B. CT-scan set-up with the vertical line directed towards the source.

2.2.6 Unconfined compressive strength (UCS) determination

Before the sample was placed into the uni-axial stress-strain device, the aluminium cup was removed from the saturated samples and the samples were weighted without the nettings and tie wraps. However, at times sand fell out, but remained in the aluminium cup that was weighed. Furthermore, some sand remained trapped within the nettings after removing them from the sample. The netting and aluminium cup were flushed with water and the sand and water was caught in a bowl after weighing the bowl separately (Fig. 2.11). The water-sand mixture in the bowl was left to dry overnight, allowing weighing the dry sample and determining the amount of lost sample. Up to 9 gr per sample was lost during the complete experiment (section 4.2.2). An aluminium attachment piece was added, creating extra space beside the sample to accommodate the sample within the pressure pieces of the device (Fig. 2.10.A). Two sieve meshes with pores of 82x82 µm and a diameter of 3.0 cm were added to both sides of the sample to prevent sand from escaping at higher pressures. Before placing the sample in the uni-axial stress device, the edge of the sand was pressed flat using the push device, so that the force was evenly distributed over the sample. Furthermore, two Linear Variable Differential Transformers (LVDT's) were positioned to measure the movement of the bottom piston. Estimation of the maximum overburden load at 1100 m depth was calculated using the formula:

$$P = \rho \times g \times z$$

Eq. 2.9

In which P is the overburden pressure, ρ the average density of the overburden material and z is the depth. The density of the sediments of the Breda Formation is approximately 2000 kg/m^3, estimated from density logs KTG-01 and RLO-01. This results in an overburden stress of 23.5 MPa at 1100 m. To account for the potential presence of higher-density shales within the Breda Formation, the experiment was performed to a maximum load of 30 MPa. The stress applied by the stress-strain device was increased at a displacement-controlled speed of 0.0100 mm/s, reaching 10.6 kN, equivalent to a stress of 15.0 MPa on the sample and simulating a depth of approximately 850 m, for the first

experiment, and reaching 21.2 kN, corresponding to a stress of 30.0 MPa on the sample and simulating a depth of approximately 1700 m, after CT-scanning. During stress increase the LVDT's had to be displaced multiple times, as the bottom piston moved out of the recording range. After compressing the samples, a CT-scan was made, and the samples were left to dry in the oven at 60 °C over the weekend before porosity measurements were performed again using the pycnometer.

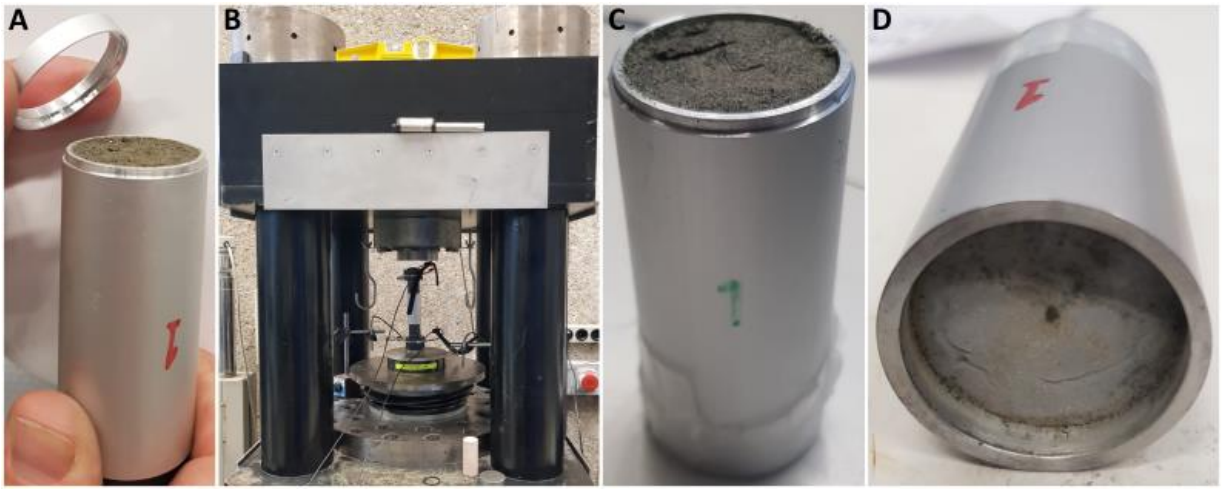

Fig. 2.10 A. Aluminium attachment piece to fit the sample in between the pressure pieces. B. Set-up of the sample in the uni-axial stress-strain device. C. Sample 1 before compressing. D. Sample 1 after a strength of 21.2 kN on the sample with sieve meshes at the edges.

Fig. 2.11 Total lost sand from the aluminium cups used during CT-scans and nettings between saturating of the samples and compressing them.

2.2.7 Acoustic velocity

The acoustic velocity experiment involved measuring the arrival time of pressure waves passing through the five different sand samples using Piezo transducers. The Piezo transducer converted voltage, generated by an 33210A Agilent arbitrary waveform generator, that was amplified by an Electronics & Innovation RF Power Amplifier, into mechanical tension (Fig. 2.12). There are shear wave (s-wave) Piezo transducers, through which both shear- and pressure waves (p-waves) pass and p-wave Piezo transducers, through which only p-waves pass. The first sample was measured with shear wave

Piezo transducers, but those were replaced with pressure wave Piezo transducers for the other samples to enhance the clarity of the p-wave signals. After transmission of the mechanical tension through the sample, the signal was converted back to voltage by the Piezo receiver. The signals were displayed on a Yokogawa DL9240L digital oscilloscope and saved on a computer. The saved data consisted of two files: one containing binary-encoded voltage data and a par-file containing information about the channel used, the number of measured points, the vertical and horizontal sensitivity per division, the sampling rate, the off-set value, and the measuring time. The received signals were averaged and saved every 20 seconds. Acoustic measurements were manually started concurrently with compression of the sample. Furthermore, signals through the Piezo transducers were measured without an intermediate sample to determine the time required for the acoustic signal to pass through the wiring in the set-up and the Piezo transducers alone, without involving the sample. The acquired p- and/or s-wave data were processed and plotted using a MATLAB script (Appendix 10). P-wave arrival times could be indicated from the plots. The p-wave arrival time, after passing the sand sample, was corrected for delays in the measuring system by subtracting the p-wave arrival time of the Piezo transducers without an intermediate sample from the p-wave arrival time of the Piezo transducers with an intermediate sample. P-wave velocity was then calculated by dividing the length of the sand samples at the time of the acoustic measurement by the corrected arrival time. The selected points that indicate the start of the p-wave were consistent in all measurement to allow for relative comparisons. It is important to note that interpreting the absolute p-wave velocities requires caution due to uncertainties arising from the attachment of Piezo transducers to uneven sides of the sand samples and uncertainties on the arrival time of the p-wave. Furthermore, averaging signals over 20 seconds introduced uncertainties, considering that the sample was deforming over this time-period.

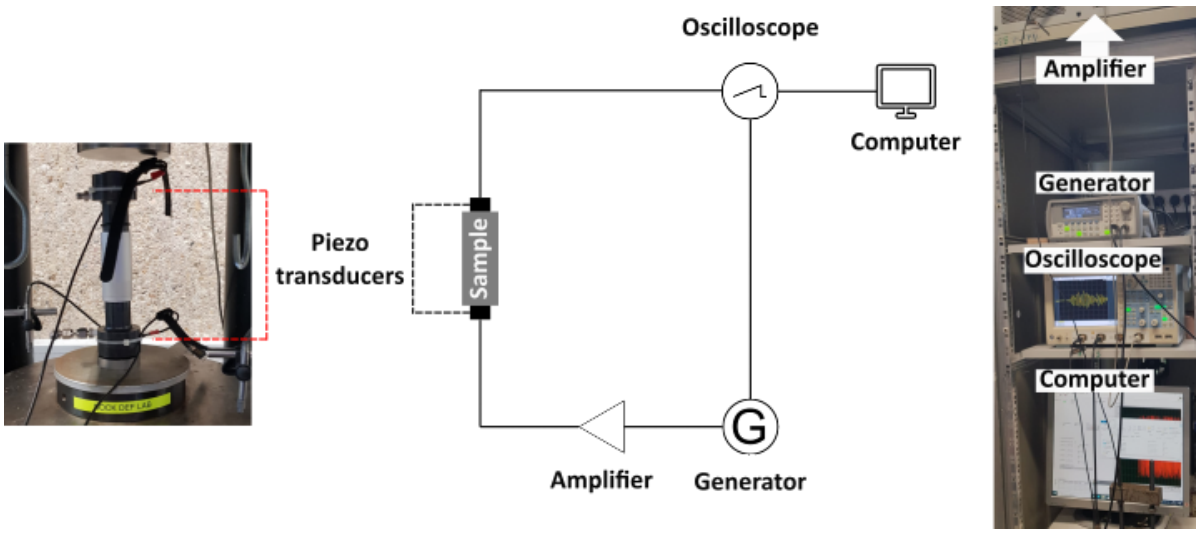

Fig. 2.12 Schematic set-up of the acoustic velocity experiment and pictures of the devices in the lab.

3. Results

3.1 Effective porosity calculations from log data

Effective porosity was calculated from sonic and density logs of the selected deep wells and shallow wells B30G4529, B49F0378, and DAPGEO_2_500m. Porosity calculated based on the sonic log alone results in a large error range, as detailed in section 3.1.2. Porosity calculated from the density shows a smaller error range, as no correction for compaction is necessary. The compaction factor, which is one of the main causes of a large error range in porosity estimates based on the sonic log, can be corrected using cross-plots of sonic porosity estimates against density porosity estimates. Comparing porosities calculated from the different log types can give an indication of the uncertainty of the porosity calculations. In Fig. 9.4 (corrected) sonic and density porosities of all selected wells are illustrated together with the GR, DT, (RHOB), and lithology of the matching shallow well.

3.1.1 Overview of effective porosity estimates

In all wells, with exception of KTG-01 and B30G4529, an overall negative trend is visible with increasing depth for the porosity estimates in the Breda Formation (Fig. 3.1). These wells also show a small increase in porosity with increasing depth just below the Oosterhout Formation, before the negative trend in the Breda Formation (Fig. 3.1). No distinct trend is visible in the calculated porosity data within the Oosterhout Formation. JPE-01, KTG-01, and B30G4529 show a clear decline in porosity estimates with increasing depth for the Oosterhout Formation. However, significant jumps to higher porosity values are observed in the Oosterhout Formation in B49F0378, DAPGEO_2_500m, JPE-01, KTG-01, RLO-01, and B30G4529. NWK-01 shows a gradual increase of porosity values with increasing depth (Fig. 3.1). Limited data availability prevents the identification of trends within the Maassluis Formation. In HBV-01 an increase of the porosity is visible, while KTG-01 shows minimal variation in porosity values, and B30G4529 includes negative porosity peaks (Fig. 3.1). These porosity estimates include incorrect data with porosities lower than 0% and higher than 50%. This could only be explained by the presence of gravel or shell layers. Major porosity fluctuations occur throughout the depth record. The parameters in the calculations (section 2.1.3) also introduce considerable uncertainty, with alternative parameter selections being viable. The minimum and maximum estimates calculated with the most extreme selected parameters that can be derived from the log data on effective porosities, are described in section 3.1.2. All wells exhibit a general negative porosity trend, i.e., decreasing with depth over the complete depth profile, but locally show variations in porosity at different depths.

3.1.2 Error range

Calculating the ϕ^e_{son} results in large error ranges up to ~80% between minimum and maximum estimates (Fig. 3.2 and Fig. 9.3). It should be noted that these overestimate the uncertainty, as outliers in the log data are used as input data (Table 9.6). Across the well record these error ranges fluctuate, especially for wells RLO-01 and JPE-01, where error ranges reach approximately 50-80% between minimum and maximum estimates. KTG-01, WDL-01, and HBV-01 exhibit lower error ranges of up to 25%. ϕ^e_{den} estimates show smaller error ranges compared to the ϕ^e_{son} estimates, with a maximum of ~60%. Similarly, for ϕ^e_{den} estimates, RLO-01 and JPE-01 show the largest error range of up to 60%, while KTG-01 shows a smaller error range with a maximum of 15%. B30G4529 has error ranges for ϕ^e_{son} and ϕ^e_{den} of up to 50%. The density porosity shows smaller error ranges compared to sonic porosity (Fig. 3.2). No correction for compaction is necessary when calculation is based on the density log, which could explain this smaller error range.

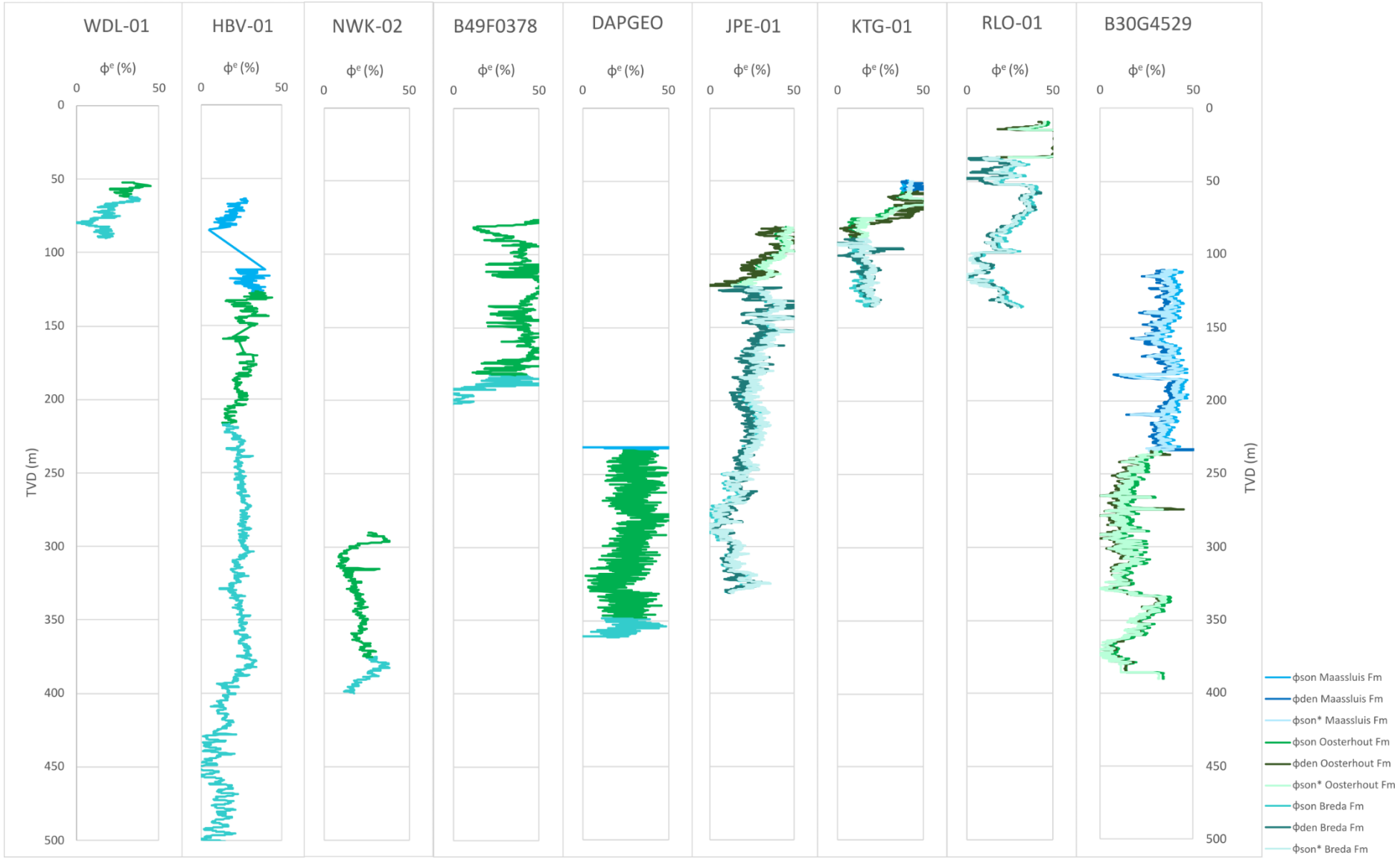
WDL-01
HBV-01
NWK-02
B49F0378
DAPGEO
JPE-01
KTG-01
RLO-01
B30G4529
ϕe (%)
0
50
TVD (m)
0
50
100
150
200
250
300
350
400
450
500
ϕson Maassluis Fm
ϕden Maassluis Fm
ϕson* Maassluis Fm
ϕson Oosterhout Fm
ϕden Oosterhout Fm
ϕson* Oosterhout Fm
ϕson Breda Fm
ϕden Breda Fm
ϕson* Breda Fm

Fig. 3.1 Overview of effective porosity (φ^e) estimates calculated from the sonic log (φson), the density log (φden), and the sonic log (φson) for which the compaction factor is corrected using the density porosity for the Breda Formation (turquoise shades), Oosterhout Formation (green shades), and Maassluis Formation (blue shades). The porosity estimates are shown over a range of 0-50% along 0-500 m True Vertical Depth (TVD). A general negative trend is visible with increasing depth for all selected wells.*

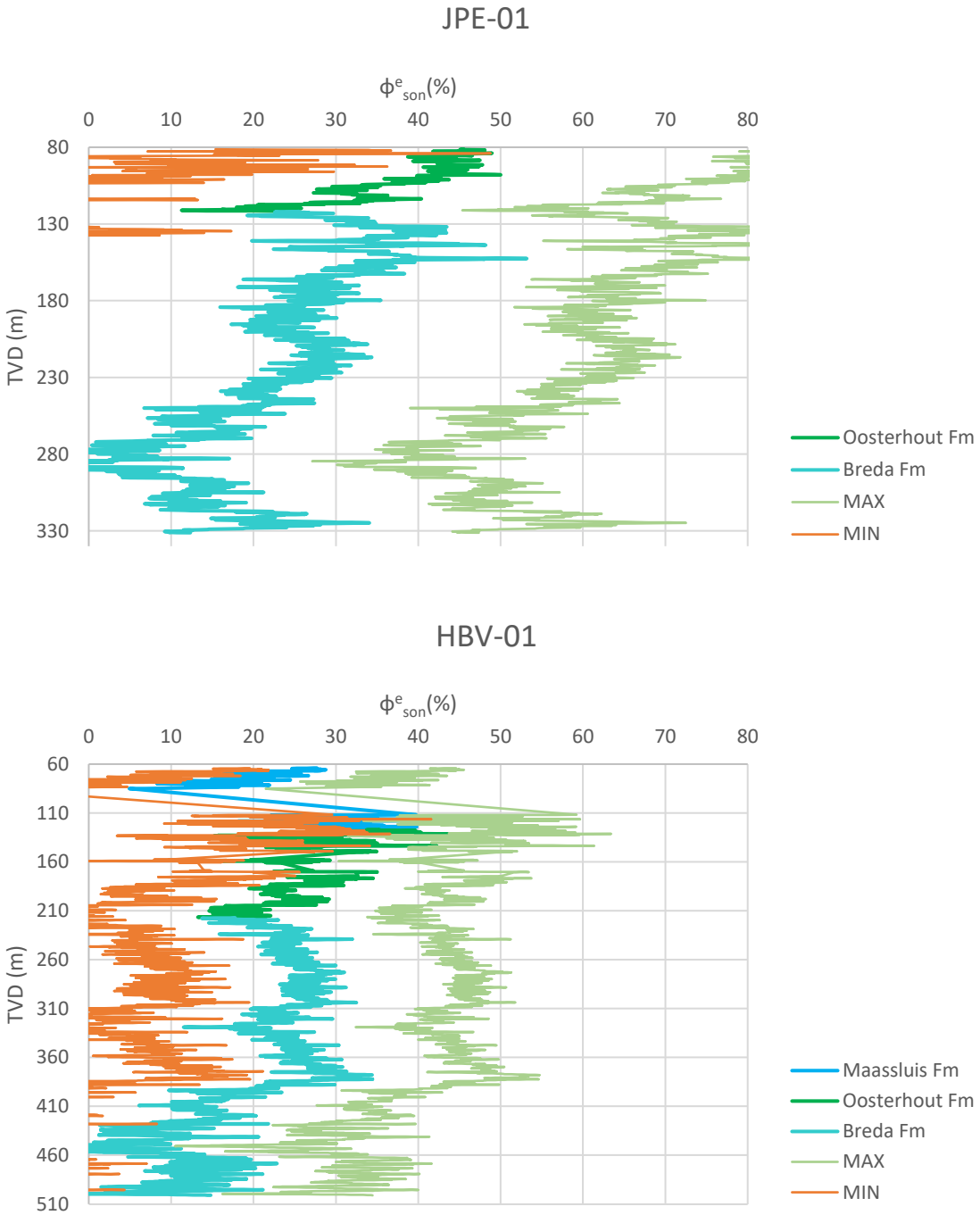

Fig. 3.2 φ^e_{son} calculations of the HBV-01 and JPE-01 well against the True Vertical Depth (TVD in m). The minimum (red), maximum (light green), and φ^e_{son} estimates based on selection of average log values, for the Breda (turquoise), Oosterhout (dark green), and Maassluis (light blue) are visualized for a porosity range of 0-80%.

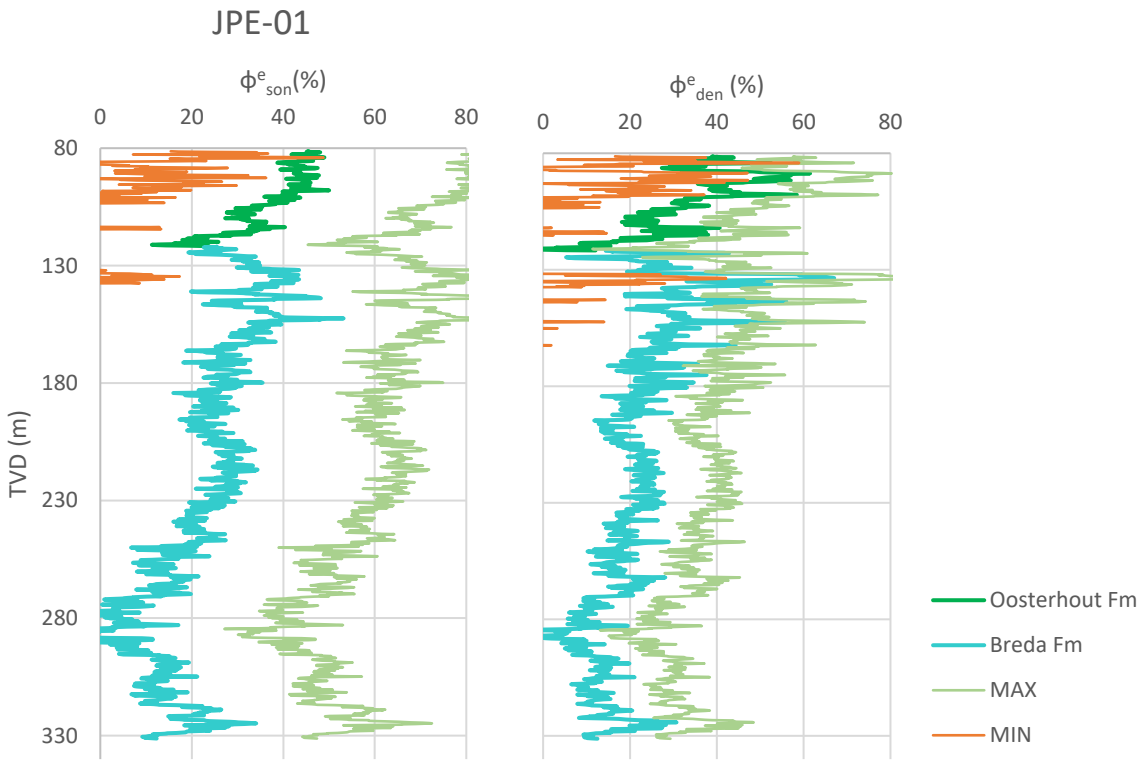

Fig. 3.3 φ^e_{son} and φ^e_{den} calculations of the JPE-01 well against the True Vertical Depth (TVD; in m). The minimum (red), maximum (light green), and φ^e_{son} estimates based on carefully picked parameters for the Breda (turquoise) and Oosterhout (dark green) are visualized for a range of 0-80%.

The compaction factor used to calculate the φ^e_{son} is adjusted to the best fit with φ^e_{den} for wells JPE-01, KTG-01, RLO-01, and B30G4529, where density log data are available (Fig. 3.4). JPE-01 shows a good correlation between ϕ^e_{son} and ϕ^e_{den}. At lower porosity values up to ~10% ϕ^e_{den} tends to be higher compared to φ^e_{son}. For porosity above 10%, ϕ^e_{den} estimates are lower compared to ϕ^e_{son}. Despite correction of the compaction factor, ϕ^e_{den} is still low compared to φ^e_{son} at porosities higher than 10%, but the overall disparity decreases. KTG-01 demonstrates a good correlation between ϕ^e_{son} and ϕ^e_{den} up to 20%, beyond which significant discrepancies emerge. After correction based on the compaction factor, there is still a lack of correlation between the ϕ^e_{son} and ϕ^e_{den}. Both graphs illustrate a shift from lower ϕ^e_{den} estimates compared to ϕ^e_{son} estimates for porosities below 20% to relatively higher lower ϕ^e_{den} estimates compared to ϕ^e_{son} estimates for porosities above 20%. Similarly, RLO-01 displays poor correlation between ϕ^e_{son} and ϕ^e_{den}. Two groups of porosity estimates are present; one with lower ϕ^e_{son} estimates and the other with higher ϕ^e_{son} estimates. After correction of ϕ^e_{son} this division is still visible. Finally, B30G4529 shows the strongest correlation between ϕ^e_{son} and ϕ^e_{den}, including some outliers with higher ϕ^e_{den} compared to ϕ^e_{son} for porosities above ~25%. Consequently, even after correction of the compaction factor not all porosity estimates show strong correlation, raising doubts about their quality.

JPE-01

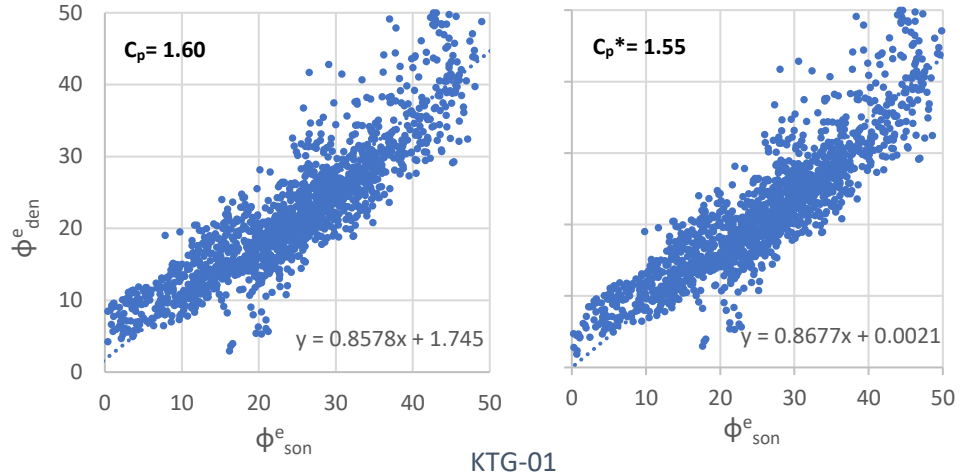

KTG-01

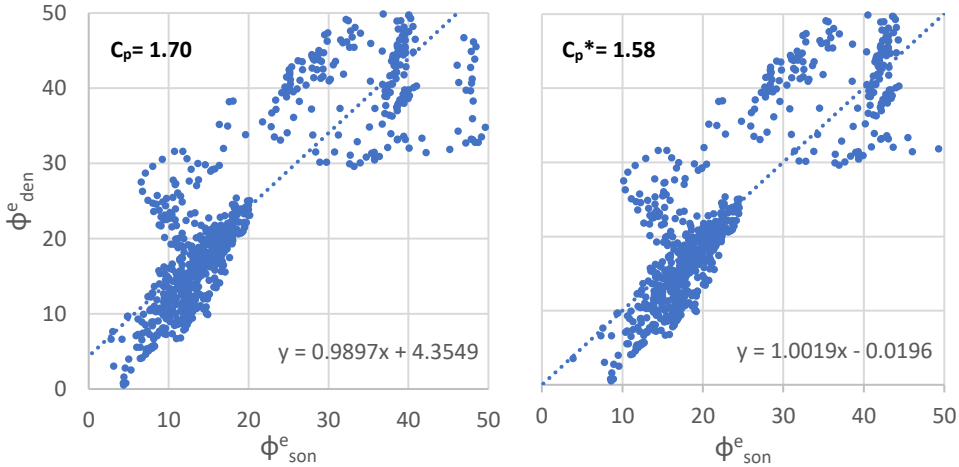

RLO-01

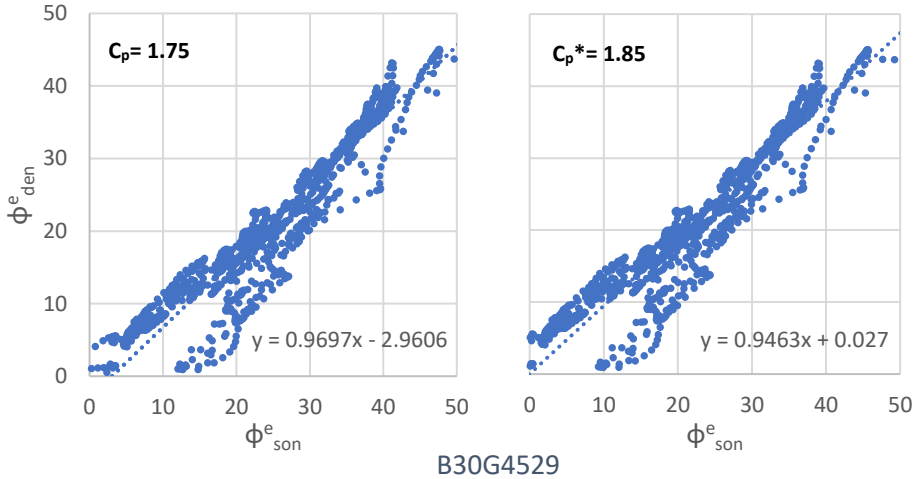

B30G4529

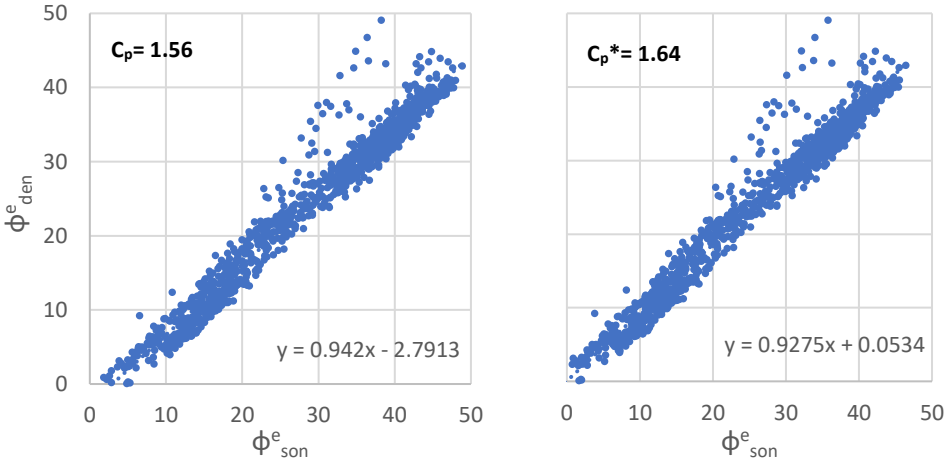

Fig. 3.4 Cross-plots of φ^e_{den} against φ^e_{son} of wells JPE-01, KTG-01, RLO-01, and B30G4529 for the uncorrected compaction factor (C_p), which is based on the DT_{sh} of a nearby shale bed, and for the corrected compaction factor (C_p), which is based on the best fit between the φ^e_{den} and φ^e_{son}. Wells JPE-01 and B30G4529 show a good fit between the φ^e_{den} and φ^e_{son}, as wells KTG-01 and RLO-01 show a bad fit, even after correction of the compaction factor.*

3.1.3 Qualitative match with lithology

Porosity estimates decreases by mechanical and chemical compaction, but different lithologies may also result in different porosities over the depth record. Therefore, the quality of the calculated porosity data is also indicated based on their changes with lithology variations. Effective porosity of clay is generally lower compared to the effective porosity of sands (Woessner & Poeter, 2020). Comparison between porosity calculations of deep wells and lithology interpretations of nearby shallow wells are conducted, with wells B30G4529, B49F0378, and DAPGEO_2_500m utilizing their own lithology data for comparison. It is important to note that major lateral variations in lithology may occur over a few hundred meters, which makes the lithology data of shallow wells with a larger distance from the combined deep well less reliable for comparison (Fig. 9.4).

HBV-01

The lithology data of the nearby well B44G0232 only has small overlap with the ϕ^e_{son} data of HBV-01 (Fig. 9.4). The quality of the sonic data above 200 mMD* (meter measured depth) is questionable due to the presence of gaps and noisy values in the sonic log data, complicating the correlation between interpreted lithologies from well B44G0232 and the calculated ϕ^e_{son} data. The presence of clay above the shell layer at approximately 150 mMD matches the calculated lower ϕ^e_{son} at this depth. Below 400 mMD the decrease in ϕ^e_{son} correlates with the presence of clay, as interpreted in the composite log of the deep well HBV-01. This clay presence cannot be compared to lithology data of higher quality, as B44G0232 does not reach this depth and no other lithology data is available.

JPE-01

Above 180 mMD there is a large number of fluctuations in the calculated porosities (Fig. 9.4). These variations do not compare exactly with the presence of sand or clay in B33F0116 and B33F0115, but can relate to the thin alternations between sand and clay layers from 100 mMD to 160 mMD. The different lithology interpretations between B33F0116 and B33F0115 complicate the comparison of the porosity estimates with the lithology. Below 260 MD very low porosity estimates (0-20%) are calculated, which correlates with high GR values. There are no lithology data present to interpret these low porosities.

KTG-01

B48E0081 has no overlap with the depths including porosity estimates of KTG-01 (Fig. 9.4). The composite log shows a less sandy lithology correlating to lower porosity estimates below 85 mMD (Fig. 9.4). The discordance in the composite well log correlates with porosities below zero, that are caused by a peak in the GR to values above 150 gAPI. The reliability of this data is questioned as GR values generally range from ~20 gAPI to ~120 gAPI (Fig. 9.4).

NWK-02

In B30F0470 clay is consistently present over the entire depth range where porosities were calculated, with a thin sand layer at approximately 305 mMD (Fig. 9.4). However, this clay presence does not align

** mMD (meter Measured Depth) is the linear distance along the borehole from the rotary table to a point in the well. This differs from the TVD (True Vertical Depth), as this is the vertical distance from the surface elevation of the well location in AHN to a point in the well.*

with the higher porosities up to 45% at approximately 300 mMD, 322 mMD and 390 mMD. Furthermore, the lithology of the composite well log indicating the presence of sand throughout the selected depth range does not correlate with the estimated porosities, which include values of approximately 20%.

RLO-01

The transition from sand to clay at 110 mMD in B34D0223 can be correlated with the decrease in porosity at approximately 100 mMD (Fig. 9.4). The very low GR values between 35 and 53 mMD, which result in very high porosity estimates of approximately 50-60%, correspond to a coarse sand layer. The lower porosity values of approximately ~15-30% below 53 mMD cannot be explained by the presence of sand, as interpreted in B34D0223.

WDL-01

The high porosity values up to 48% above 73 mMD correlate with sand interpreted in B28B0143. The lower values of approximately 30% can be explained by the finer sand fraction (ZZFO) at this depth (Fig. 9.4). Moreover, the loam below the fine sand matches with the relatively high porosity calculations of ~36%. Furthermore, the lower porosity values below 83 mMD correlate with the decrease of sand fraction as denoted by the composite well log image of WDL-01.

B30G4529

The transition from sand to clay at approximately 250 mMD is evident in lower porosity estimates below 250 mMD (Fig. 9.4). Thin shell layers correlate with depths with relatively low porosity values of 15-20%. The increase in porosity up to values of ~34% is like depths where sand and loam is present at 340-360 m. The quality of porosity estimates below 385 mMD is questioned due to the constant GR and DT values at these depths, which is unusual in log data.

B49F0378

The sonic log of this well shows numerous extreme fluctuations, which questions the quality of these log data. Therefore, resulting porosity estimates also show fluctuations, that cannot be correlated to the interpreted lithology. The unusually thick shell raises further doubts on the quality, as this has not been encountered in other lithology interpretations of the Breda Formation.

DAPGEO_2_500m

The sonic and gamma ray log varies significantly, resulting in rapidly varying porosity calculations (Fig. 9.4). This questions the quality of both the log data and the resulting porosity estimates. For the sand interval at 274-280 mMD the porosity estimates ranging from 35-50% are somewhat higher compared to the surrounding clays (Fig. 9.4). The surrounding clays show a wide range of calculated porosities, varying from approximately 20% to 40% (Fig. 9.4). The porosity ranges for the different lithologies can be expected for these lithologies. However, the ranges are relatively large, which may obstruct the detailed interpretation of the porosity values.

Consequently, the wells show variations in correlation between calculated porosity estimates and lithology interpretations from nearby shallow wells or within the same well. The correlation of HBV-01 and KTG-01 between the lithology and porosity estimates cannot be determined, because of a lack in corresponding depths in the different data. NWK-02 and B49F0378 show an overall poor correlation between the interpreted lithology (of the selected nearby well), while RLO-01, WDL-01, B30G4529 and DAPGEO_2_500m exhibit a generally strong correlation. Notably, JPE-01 shows a stronger correlation with B33F0116 than with B33F0115. This demonstrates that comparison with lithology of nearby wells

should be made with caution due to lateral differences in lithology and differences in interpretations of the lithology.

Log data of well B49F0378 and DAPGEO_2_500m are suggested to include high uncertainty and are therefore not further used in the comparison with experimental porosity data.

3.2 Porosity measurements using a pycnometer

No clear trend is visible in the effective porosity measured by a pycnometer before and after subjecting the sample to an overburden load of approximately 30 MPa (Table 3.1). The measured porosity before and after applying the load shows minor differences of up to 3.1% for sample 4 (Table 3.1). The porosity decreases for samples 2 and 5, as samples 1, 3 and 4 show an increase in measured porosity after subjecting the samples to experimental overburden pressure.

Sample	φ^e *before pressure* (%)	Maximum pressure (MPa)	Maximum depth (m)	φ^e *after max pressure* (%)	$\Delta\varphi^e$ *after max pressure* (%)
1	30.5	29.7	1679	32.2	1.7
2	33.8	29.8	1683	32.8	-0.9
3	35.9	44.7	2526	36.0	0.2
4	28.0	29.5	1669	31.1	3.1
5	32.2	26.8	1516	30.0	-2.1

Table 3.1 The effective porosity of samples 1-5 before and after subjecting the sample to a simulated overburden load of 30 MPa measured by a pycnometer and the measured porosity change between measurements after 30 MPa pressure and before applying pressure.

3.2.1 Comparison with porosity data of Liessel core and lithology

No laser particle size analysis and total porosity measurements using the falling head method were performed on samples 1-5. Comparison between porosity estimates from this study, measured with a pycnometer, with earlier porosity measurements from samples of the Liessel core using the falling head method is difficult, because of the different depths on which the samples were collected (Fig. 3.5). Only sample 4 shares the same depth in the Liessel core as another data point, including laser particle size analysis data (Fig. 3.5). The effective porosity measured using the pycnometer is lower compared to total porosity measurements using the falling head method of nearby data points (Fig. 3.5). Samples 1, 4 and 5 show the largest differences compared to the porosity estimates of nearby data points (Fig. 3.5). Sample 2 and 3, which have the highest measured effective porosities, are like the porosity estimates of the nearby data points (Fig. 3.5). Particle-size measurements of the other samples using a laser differ from the particle size estimates from the core description, with most data points including less sand than estimated values in the core description (Fig. 3.5). An overview of the lutum, silt, and sand percentages, M50 of the sand fraction, and total porosity of the nearby data points for samples 1-5 are given in Table 3.2. It is difficult to indicate the accurate lithology for samples 1-3 and 5, because of the different depths of core description and laser particles size analysis data points and possible variations in lithology for different depths throughout the Breda Fm. Section 4.2.3 provides additional insights into the comparison between core description data and laser particle size analysis data, as well as the indication of the lithology for samples 1-5.

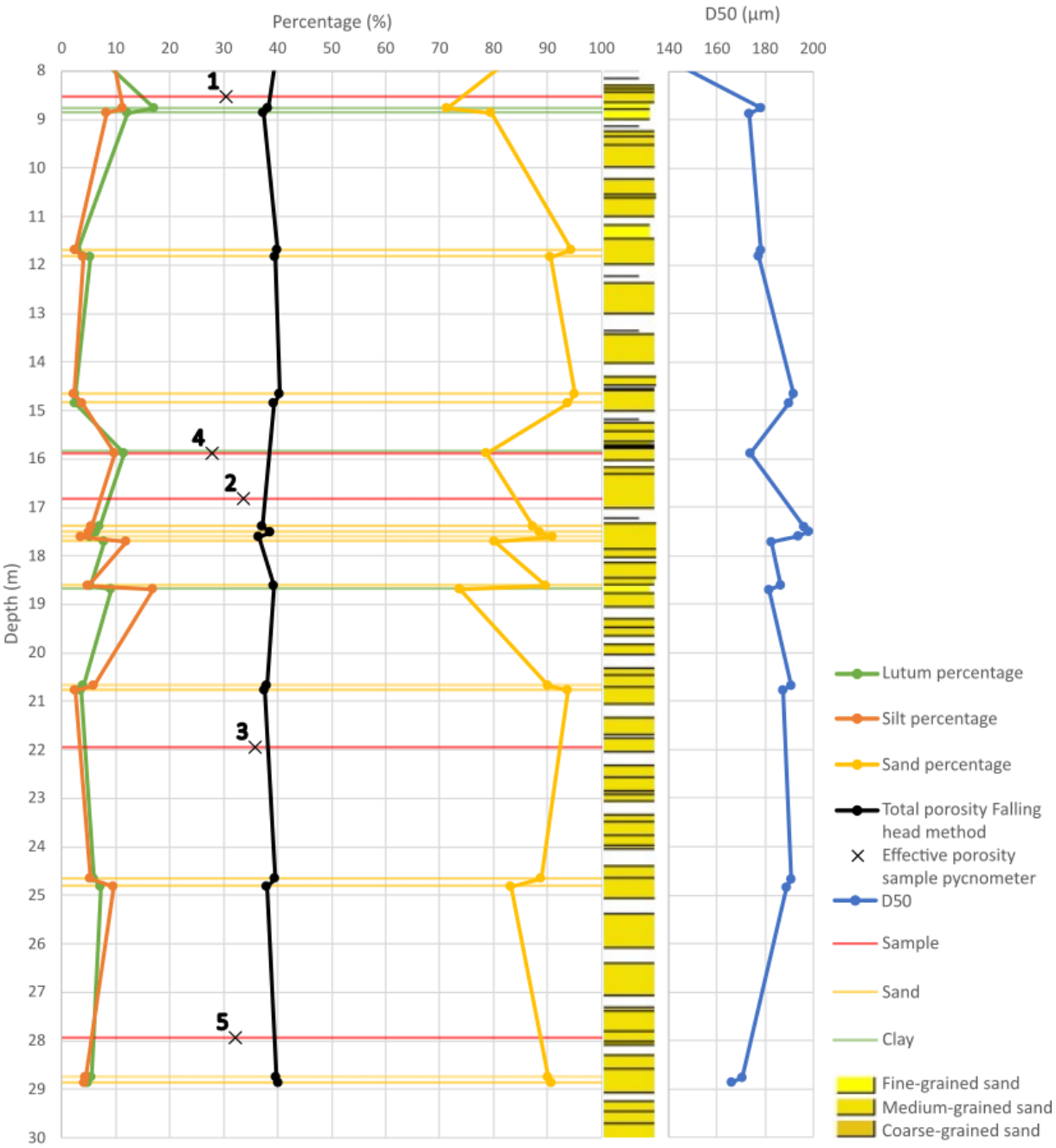

Fig. 3.5 Total porosity measurements of samples within the Breda Formation from the Liessel core, B52C2133, using the falling head method (black dots), effective porosity measurements of samples 1-5 using the pycnometer (black x), clay (green), silt (red), and sand (yellow) percentages and the D50 of the sand fraction, which is the average particle size in µm measured with a laser particle size analyzer, the simplified interpreted lithology sand (yellow line) or clay (green line) according to NEN5104 (Fig. 9.6), depth of samples 1-5 (red line), and the lithology interpretation based on the core description. Effective porosity measured by a pycnometer are generally lower than total porosity measurements of other samples in the Liessel core using the Falling head method. Laser particle size diffraction data classifications in clay (green lines) do not compare with the classification in fine-grained sand (yellow blocks) based on core description data.

Sample	Depth range (cm)		Depth range nearby data point (cm)		Distance to nearby data point (cm)	D50	LU (%)	SI (%)	ZA (%)	φ^e (%)	φ_{tot} (%)
	Top	*Base*	*Top*	*Base*							
1	847	860	885	890	25	173	12.2	8.3	79.6	30.5	37.4
2	1675	1691	1738	1743	47	196	7.1	5.5	87.4	33.8	37.7
3	2188	2200	2065	2070	118	191	3.9	6.0	90.1	35.9	38.1
4	1582	1593	1585	1590	0	174	11.5	9.8	78.7	28.0	-
5	2789	2793	2874	2879	85	170	5.4	4.5	90.1	32.2	39.7
	2793	2795									
	2795	2800									

Table 3.2 Lithology, D50 of the sand fraction, lutum (LU) percentage (%), silt (SI) percentage (%), sand (ZA) percentage (%) from laser particle size analyses of data points nearby samples 1-5, the distance between the different samples, the effective porosity (ϕ^e) measured by the pycnometer of samples 1-5, and the total porosity (ϕ_{tot}) measured using the falling head method of the nearby data points.

3.3 Porosity changes calculated from displacement during the compaction experiment

The Linear Variable Differential Transformers (LVDT's) measured piston displacement every 250 ms during pressure increments up to 21.2 kN (30 MPa). When the piston moved beyond the measurement range of the LVDT's, these sensors were readjusted, resulting in discontinuities within displacement measurements. These different displacement measurements were then added together. Data points that did not show a displacement-controlled speed of 0.0100 mm/s were discarded, and the start of the displacement was set to 0. Data from experiments up to 30 MPa were combined with data from the experiments up to 15 MPa based on ascending stress values. Unedited displacement data against the stress for sample 5 up to 15 MPa are plotted in Fig. 3.6. Total porosity change was calculated from the displacement of the piston measured by LVDT's, under the assumption that this displacement only affected pore space volume without causing grain fracturing or deformation. The formula used for this calculation is:

$$\Delta V_{\text{pore}} = \pi \cdot r^2 \cdot \text{Displacement LVDT}$$

Eq. 3.1

In which ΔV_{pore} is the change of the pore volume (m^3) and r is the radius of the sand sample of 0.015 m. Together with the total volume of the sand cylinder, when no pressure is applied, the change in total porosity can be calculated. Transitions between the compiled areas show some similar total porosity values for the same depth (Fig. 3.7), attributed to breaks in pressure increase during LVDT adjustment. Adding the data of the 30 MPa experiment to the 15 MPa results in a small offset within the graphs, as this is only based on stress levels. Because the end of the pressure increase was regulated manually, discrepancies exist between the maximum stress and calculated end depths for each sample (Fig. 3.7). The displacement-controlled speed during the experiment on sample 3 was set too high, which resulted in stresses exceeding 30 MPa within seconds. Therefore, the LVDT's were not adjusted in time and the measured displacement data during this experiment is unusable to calculate the porosity change from displacement.

All samples show a total porosity decrease of 5-15% after simulating a ~30 MPa overburden load (Fig. 3.7). Sample 5 shows the highest total porosity decrease with 13.5% at 1200 m depth and sample 1

the smallest with 6.6% at 1200 m (Table 3.3). The velocity of the total porosity decrease diminishes with increasing depth for all samples (Fig. 3.7). Sample 5 differs from the other samples, as the porosity decrease is slower down to 200 m compared to the other samples (Fig. 3.7). Thus, the total porosity calculations show clear porosity reduction with increasing depth for all samples.

Sample	Depth (m)	$\Delta\phi_{tot}$ (%)
1	1200	-6.6
2		-10.3
4		-9.4
5		-13.5

Table 3.3 The total porosity decrease at 1200 m depth for samples 1, 2, 4, and 5. The depth is calculated from the pressure based on a density of the overburden sediments of 1770 kg/m^3

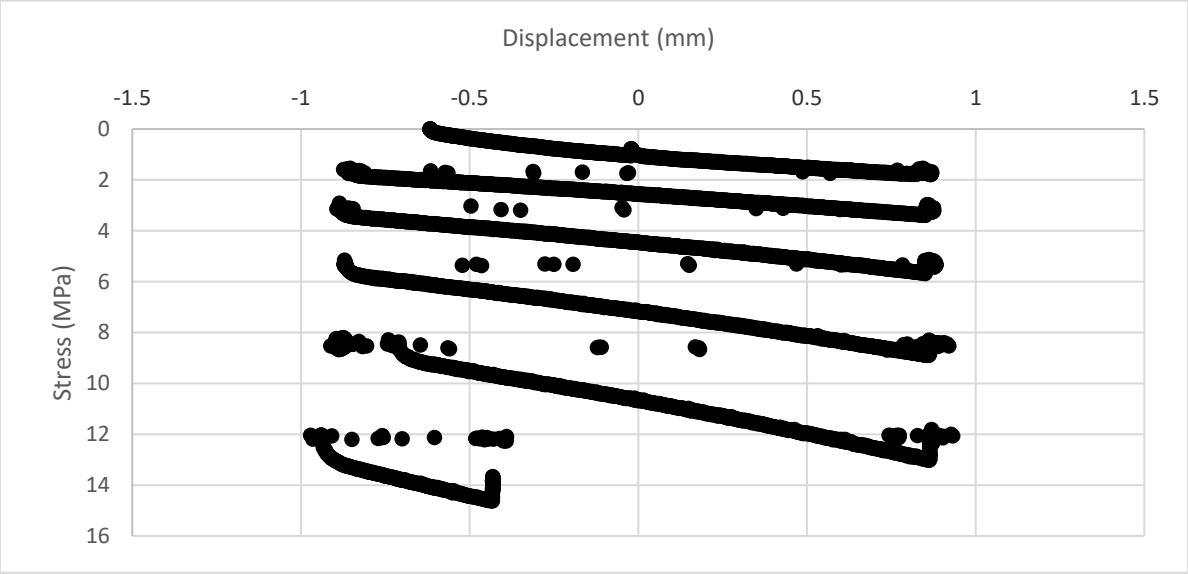

Fig. 3.6 Raw displacement data measured by the LVDT's against the stress for sample 5 in the experiment up to 15 MPa. The scattered jumps from a positive to a negative displacement are caused by readjustment of the LVDT's. The beginning of the continuous line, showing increasing displacement with higher stresses, is added to the end of the upper continuous line.

3.4 Porosity calculations from CT-scans

The possibility to calculate the total porosity (with error range) from CT-scans with a resolution of 25.0 or 27.5 µm was tested on a cropped cube of the CT-scan data of sample 1 after exposure up to 15 MPa (Fig. 3.8). The CT-scans were edited using normalization and unsharp operations in Dragonfly to distinguish between pores and grains more clearly (Fig. 3.9). The plotted range of gray values was adjusted to better visualize the different gray scales and the histogram (Fig. 3.10). Using the Otsu method in Dragonfly the lower gray value range, the Lower Otsu, was selected, which indicates the pore spaces (Fig. 3.11). The higher gray value range, the Upper Otsu, that was selected, indicates the grain volume.

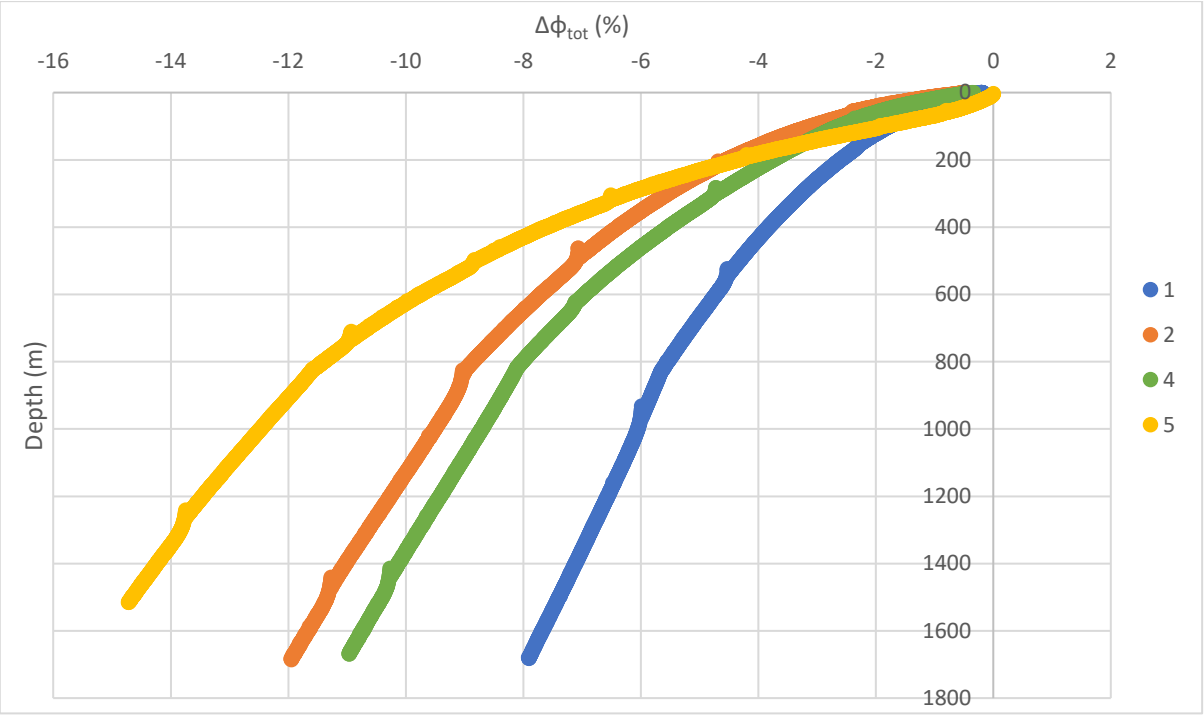

Fig. 3.7 Overview of the calculated total porosity change against the depth for samples 1, 2, 4, and 5. The depth is based on an estimated density of the overburden load of 1770 kg/m^3. All samples show a trend to a more negative porosity change at larger depths. At shallower depths this porosity decrease is faster compared to larger depths. The total porosity of sample 3 could not be calculated from displacement, because of an error in the settings to apply pressure, which resulted in a lack of displacement data.

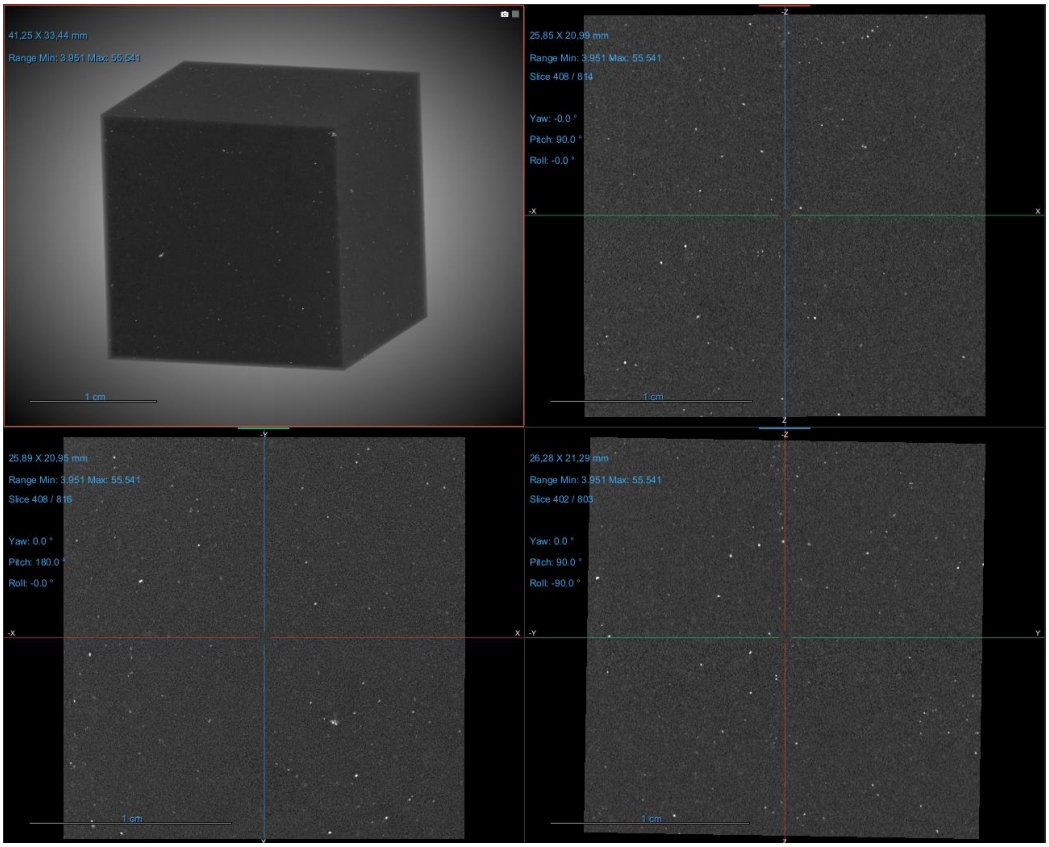

Fig. 3.8 Cropped cube of CT-data of sample 1 after 15 MPa pressure showing a 3D view, XY, XZ, and YZ slice.

The resolution of the CT-scans is too low to result in a clear dichotomy of gray values. Due to the lack of clear dichotomy in the gray values as visualized in the histogram, defining a distinct lower and upper Otsu range proves challenging (Fig. 3.10). Therefore, different ranges are selected, leading to varying total porosity estimates (Fig. 3.11). The ~50% difference between the minimum estimate of 16.25% and the maximum estimate of 63.65% is major. These total porosity estimates are therefore excluded from comparison with other porosity estimates. A more detailed study into the gray value distribution of the CT-scans and further data processing is necessary to decrease the error range in porosity estimates. However, this is out of the scope for this study.

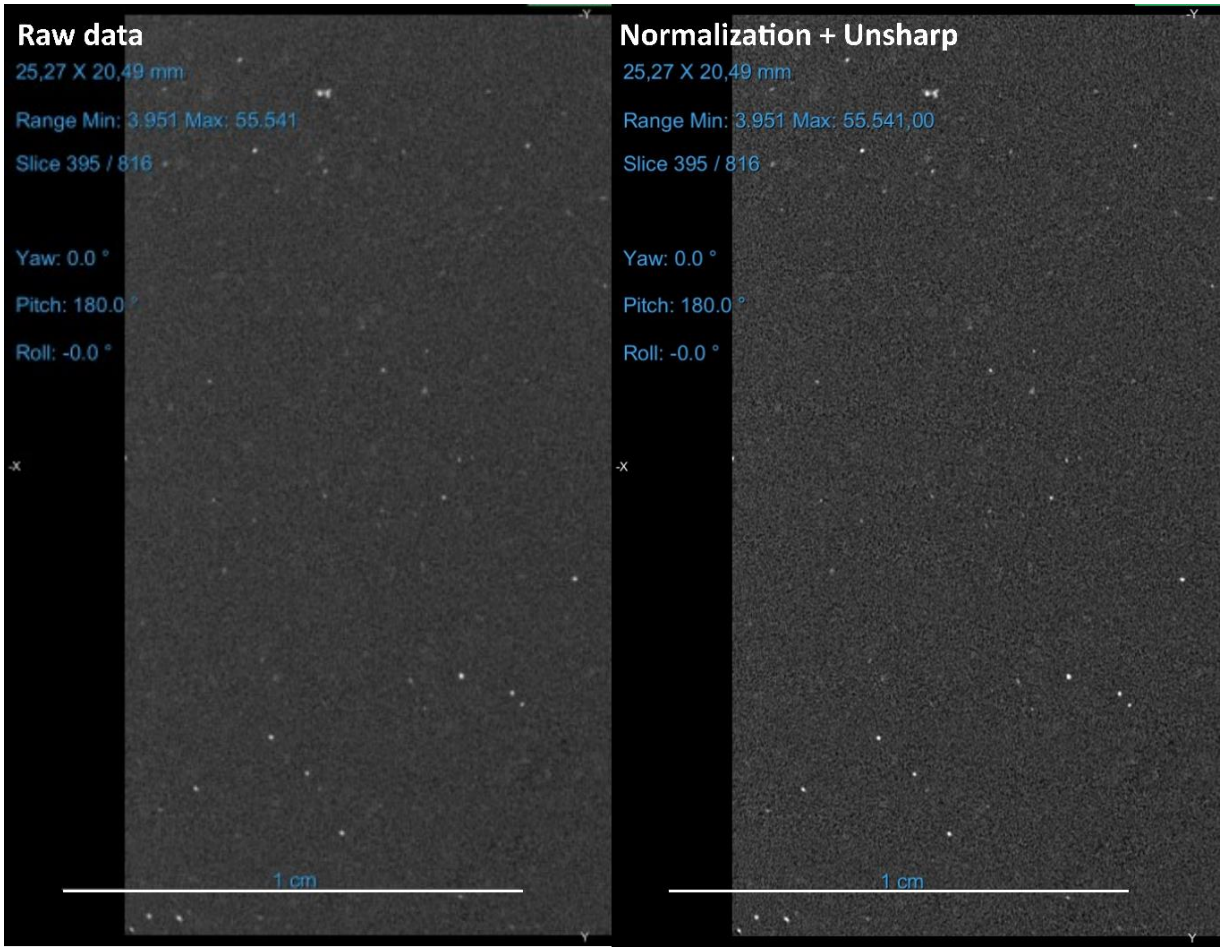

Fig. 3.9 CT-scan data of sample 1 without edits (raw data) and CT-scan data, where normalization was applied to improve the contrast in the image and the Unsharp operation with a 3D dimension, size 3, standard deviation of 1.0, and unsharp factor of 1.0 to sharpen the edges of the grains in Dragonfly of sample.

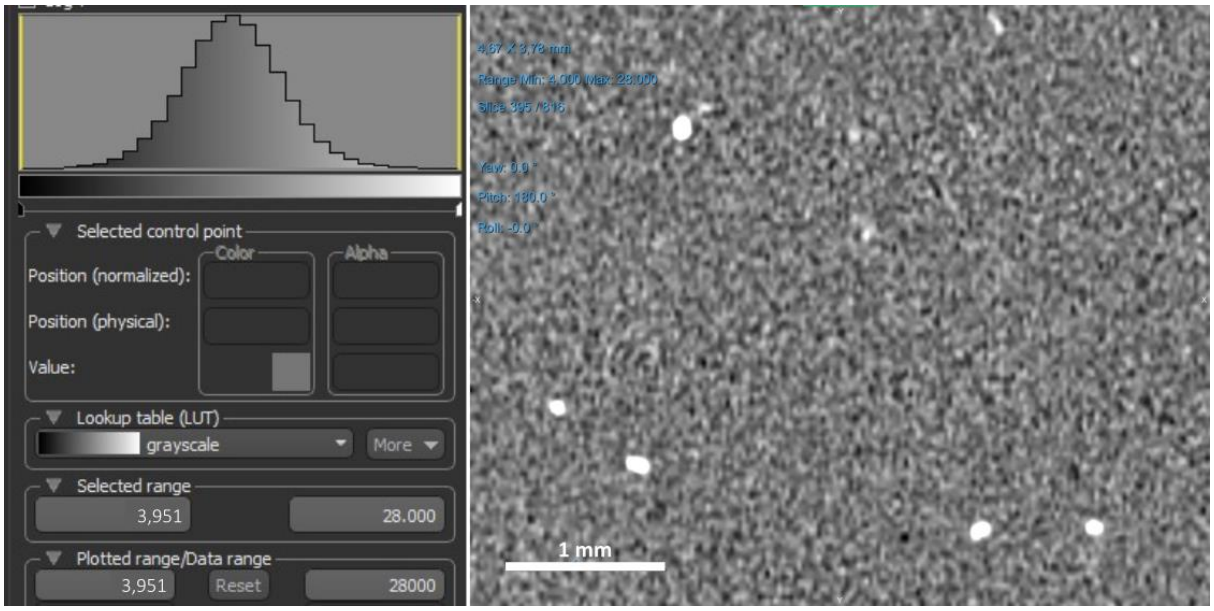

Fig. 3.10 Zoomed slice 395/816 of the cropped data cube of sample 1 with an adjusted plotted gray value range.

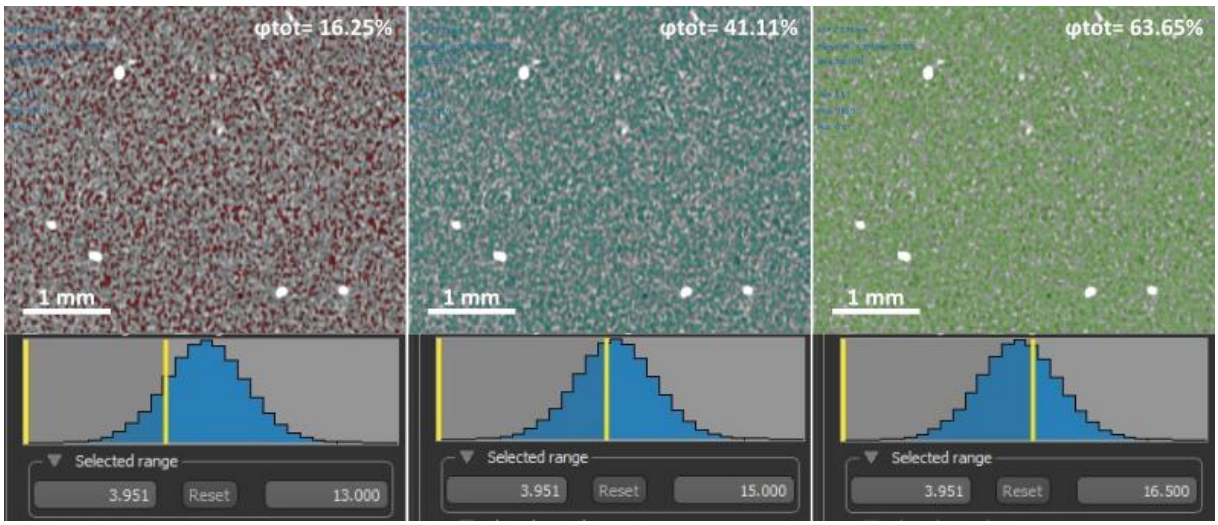

Fig. 3.11 Different estimates on the Lower Otsu range representing the pore volume of the test cube from sample 1 resulting in total porosity estimates of minimal 16.25%, medial 41.11% and maximal 63.65%. The uncertainty is too large to indicate accurate total porosity estimates based on CT-scans.

3.5 Comparison of porosity data

Different methods were used to collect porosity data on the Breda, Oosterhout, and/or Maassluis Formations for the mid-depth range (100-1200 m). The effective porosity data of samples 1-5, measured by a pycnometer prior to applying pressure, were already compared to the available total porosity data of the Liessel core using the falling head method in section 3.2.1. After exposing the samples to a burial load, the effective porosity was measured again by a pycnometer. The total porosity was calculated from the displacement. These porosity estimates are compared in sections 3.5.1 and 4.3. Total porosity was also shown as calculated from CT-scans that were performed after applying a pressure of 30 MPa. However, these porosity data include large uncertainty. Therefore, they were not compared to other porosity estimates. Furthermore, the effective porosity was calculated from log

data. Section 3.5.2 shows a comparison of these porosity data calculated from log data and experimentally derived porosity estimates.

3.5.1 Comparing experimentally derived porosity data

The effective porosity changes measured by the pycnometer for samples 1, 2, 4, and 5 do not compare to the changes in total porosity calculated from the measured displacement (Table 3.4). The calculated total porosities all show a decrease after applying a load of 30 MPa, as the effective porosity estimates show an increase for sample 1 and 4, and a less extreme decrease for samples 2 and 5 (Table 3.4). In both datasets sample 5 shows the largest decrease in porosity with the maximum applied pressure, followed by sample 2 (Table 3.4). Sample 4 shows the most significant difference between the positive effective porosity change measured by the pycnometer and the relatively strong negative total porosity change calculated from displacement data (Table 3.4). The absolute porosity changes measured by a pycnometer and calculated from displacement data show large differences, while there are some similarities in the relative variations in porosity estimates between different samples.

Sample	Maximum burial load (MPa)	Maximum depth (m)	$\Delta\varphi^e$ (%)	$\Delta\phi_{tot}$ (%)
1	29.7	1679	+1.7	-7.9
2	29.8	1682	-0.9	-12.0
4	29.5	1668	+3.1	-11.0
5	26.8	1515	-2.1	-14.7

Table 3.4 Comparison of the effective porosity change measured by a pycnometer of samples 1, 2, 4, and 5 after application of the maximum burial load and the total porosity change calculated from the measured displacement during the compaction experiment of samples 1, 2, 4, and 5 for the maximum burial load. The maximum depth is calculated from the maximum burial load based on a density of the overburden sediments of 1770 kg/m^3.

3.5.2 Comparison between sonic/density porosities and experimentally derived porosities

The effective porosity changes calculated from the log data show a larger decrease over the depth range compared to the calculated total porosity estimates based on experimental displacement data (Table 3.5). It is challenging to compare the effective porosity measurements obtained by the pycnometer with calculated effective porosity from the log data due to differences in depth ranges (Table 3.5). The change in effective porosity measurements over a depth range from ~0 to ~1600 m (Table 3.1) using a pycnometer are significantly higher than the calculated effective porosity change from log data (Table 3.5).

Sample →				1	2	4	5	1	2	3	4	5
Well ↓	Depth range (m)	$\Delta\phi^e(*)_{son}$ (%)	$\Delta\phi^e{}_{den}$ (%)	$\Delta\phi_{tot}$ (%)	$\Delta\phi_{tot}$ (%)	$\Delta\phi_{tot}$ (%)	$\Delta\phi_{tot}$ (%)	$\Delta\varphi^e$ (%)	$\Delta\varphi^e$ (%)	$\Delta\varphi^e$ (%)	$\Delta\varphi^e$ (%)	$\Delta\varphi^e$ (%)
HBV-01	64 - 501	-20.5	-	-3.0	-4.7	-4.2	-8.0					
JPE-01	81 - 343	-29.6	-24.8	-2.0	-3.2	-2.7	-5.4					
KTG-01	49 - 135	-20.6	-20.9	-1.1	-1.5	-1.3	-2.2					
NWK-02	131 - 400	-14.7	-	-1.8	-2.8	-2.5	-4.9					
RLO-01	10 - 136	-16.8	-19.0	-1.7	-2.8	-2.4	-2.8	+1.7	-0.9	+0.2	+3.1	-2.1
WDL-01	52 - 90	-17.8	-	-0.5	-0.6	-0.6	-1.0					
B30G4529	111 - 385	-25.0	-20.0	-1.9	-3.0	-2.6	-5.3					
B49F0378	76 - 234	-71.3	-	-1.4	-2.2	-1.8	-3.8					
DAPGEO_2_500m												

Table 3.5 Overview of the effective and total porosity changes calculated from (corrected) sonic and density logs ($\Delta\varphi^e(*)_{son}$ and $\Delta\varphi^e{}_{den}$), calculated from experimental displacement data ($\Delta\varphi_{tot}$), and measured by a pycnometer ($\Delta\phi^e$) over specific depth ranges that cover the Breda, Oosterhout and/or Maassluis Formations, depending on their

presence within the well. The depth range over which $\Delta\phi^e$ was calculated is not equal to the range described in this table, but covers the surface to the maximum depth, which are shown in Table 3.1. $\Delta\varphi^e(*)_{son}$ and $\Delta\varphi^e{}_{den}$ were calculated based on the average of 30 porosity estimates surrounding the minimum and maximum depth of the depth range. The calculated porosity changes are higher compared to the experimentally derived porosity changes.

It should be noted that the porosity calculations from the log data are influenced by a combination of lithological differences and compaction over the depth range, as the experimental data are not influenced by lithology changes per sample. Therefore, to facilitate further comparison between these porosity estimates, they are classified into different groups based on variations in lithology (section 4.3).

3.6 Compressional wave slowness calculations

The compressional wave slowness, DT, was calculated from arrival times of acoustic signals plotted using a MATLAB script and the sample length (Fig. 3.12; Appendix 10). The DT calculated for sample 1 after 15 MPa is different from the other estimates (Fig. 3.13). This variation could be attributed to the use of s-wave PIEZO transducers during this specific experiment, as opposed to p-wave transducers used in the other experiments (section 2.2.7). There is no general trend visible in DT with increasing depth for the different samples (Fig. 3.13). Samples 4 after 15 MPa and 30 MPa, and sample 5 after 30 MPa show lower DT estimates at larger depths, while sample 1 after 30 MPa, sample 2 after 15 MPa and 30 MPa, and sample 5 after 15 MPa show an increase in DT with increasing depths (Fig. 3.13). With exception of sample 4, applying 15 MPa pressure, the DT estimates only change 1-3 µs/ft, and are relatively constant over the depth range. Section 4.5 compares the calculated compressional wave slowness from the experimental data with sonic log data of selected wells and indicates the quality of the experimentally derived compressional wave slowness.

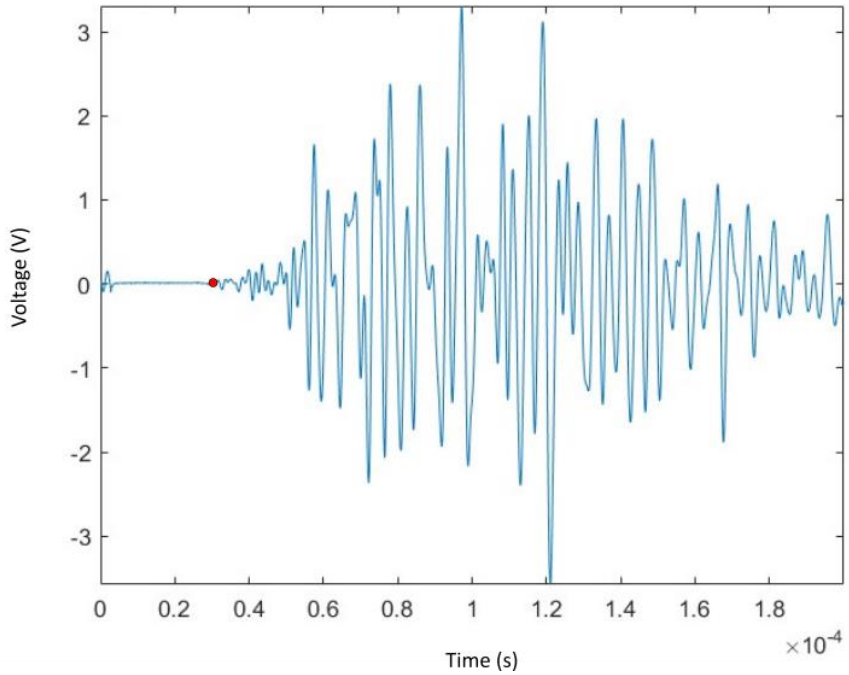

Fig. 3.12 Acoustic signal through sample 4 after applying 15 MPa stress. The red dot indicates the selected arrival time, from which the DT can be calculated.

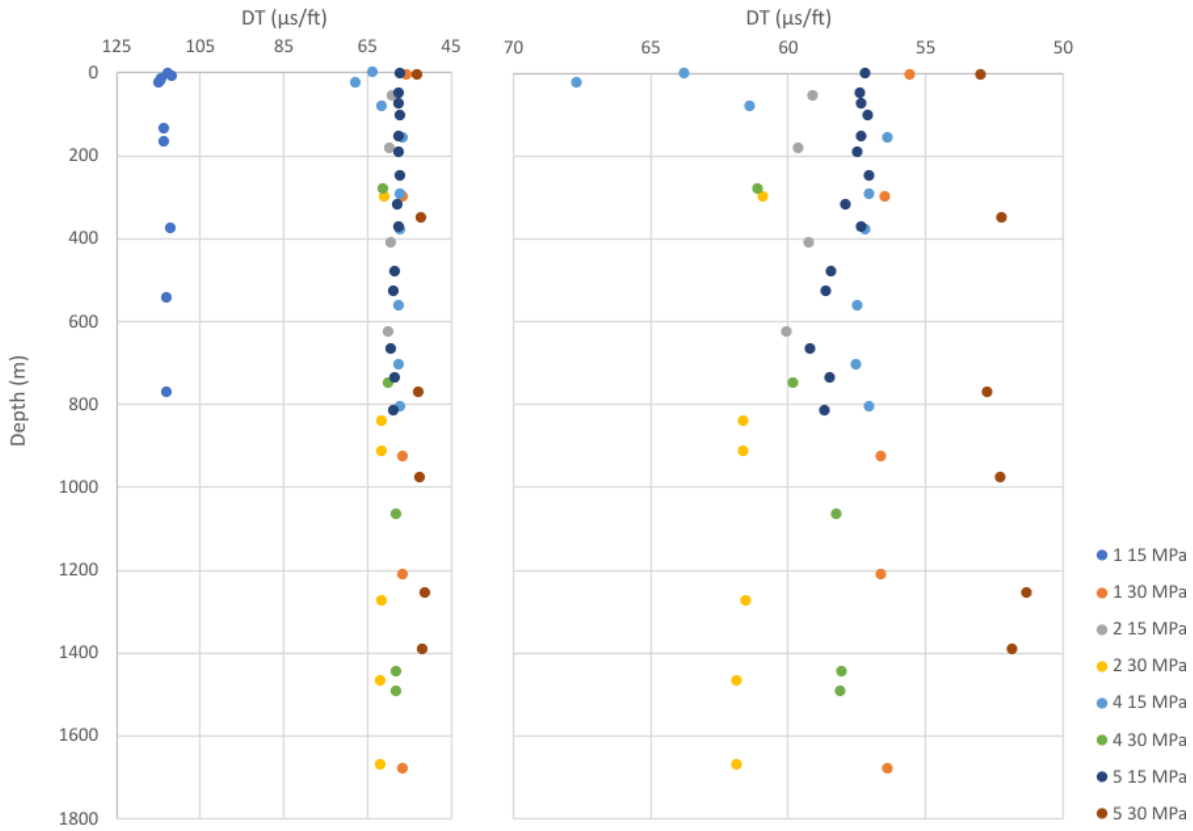

Fig. 3.13 Overview of the calculated DT (µs/ft) from acoustic signals including the different estimates for sample 1 after 15 MPa pressure, and zoomed in on sample 1 after 30 MPa, samples 2, 4, and 5 after 15 MPa and after 30 MPa against the depth, based on a density of the overburden sediments of 1770 kg/m^3. The sonic slowness calculations for sample 1 after 15 MPa is very different from the other calculations. No general trend is visible in the sonic slowness against the depth.

4. Discussion

4.1 Porosity calculations from log data

In the calculated porosity values an overall negative trend is visible to larger depths for the different wells (Fig. 3.1). This negative trend is expected, because of the influence of mechanical compaction and minor influence of chemical compaction (sections 1.5.1 and 1.5.3). It is difficult to define which part of the porosity change is caused by compaction, because lithology variations and uncertainties in the porosity calculations also result in porosity changes (sections 3.1.2 and 3.1.3). The large error ranges for the porosity calculations of up to ~80% relate to uncertainties in parameter values, such as the compaction factor and the salinity (Table 9.6 and Table 9.7; section 2.1.3), and in the quality of log data (Fig. 9.4). Therefore, interpretations based on absolute porosity estimates calculated from only a sonic or a density log should be evaluated with caution. Relative differences between porosity calculations for the selected depth range per well can be interpreted with less uncertainties, as the parameters are set for the complete depth range and do not differ with depth. The sections below describe the causes of uncertainties within the log data and other parameters to calculate the porosity from log data.

4.1.1 Uncertainties in log data and parameters in porosity calculations

Wells with low-quality log data were excluded from porosity calculations (section 2.1.2 and Table 9.4). Porosity calculations based on log data from selected wells show large error ranges (section 3.1.2). These error ranges are calculated by picking outliers in the fluctuating log data without considering existing trends. The maximum porosity estimates were calculated by selecting the maximum DT_{shale}, ρ_{fl}, GR_{min} and GR_{max} and minimum DT_{fl} and the minimum estimates with reversed extremes of the parameters (Table 9.6 and Table 9.7). Interpretations of log data involve considerable uncertainty due to the large number of influences on these log data, not all of which are fully understood. However, the error ranges based on these outliers and without criteria for minimum and maximum porosity are very extreme and overestimate the actual error range. The following sections highlight factors contributing to uncertainties and fluctuations in log data, of which not all are corrected using the formula to calculate porosity (section 2.1.3).

Gamma ray (GR) log

Calculation of the clay volume V_{cl} from maximum and minimum values of the gamma ray (GR) log relies on distinguishing between sand and clay layers using different ranges of GR values for different lithologies (Fig. 4.1). Generally, the GR is effective to distinguish between sand and clay layers, but glauconitic sands show relatively high GR values, making them comparable to clay values (Fig. 4.1) This similarity in values can result in an overestimation of the clay volume, because the GR values of glauconitic sands are close to the selected GR_{max}. Given the abundance of glauconite in the Breda, Oosterhout, and Maassluis Formations (section 1.3), the chance of overestimation of the clay content and consequently underestimating the effective porosity is high. This could explain the low porosity estimates at depths, where sand is interpreted, such as in NWK-02, WDL-01 (section 3.1.3).

The gamma ray signal is further influenced by differences in (i) borehole size, potentially caused by washouts (Fig. 4.1), (ii) eccentric orientation of the logging tool, (iii) drilling mud type, and (iv) logging through the casing (Rider, 2002). Generally, corrections for borehole size effects and eccentric tool orientation are performed by the service company. However, it is not clear whether these corrections were done for the selected wells. Addition of KCl to the drilling mud can elevate the baseline of the

gamma ray values, as the depth of investigation up to 50 cm could overlap with the presence of mud filtrate in the formation (Fig. 4.2; Geel, 1999). With exception of HBV-01, drilling mud types were obtained from drilling reports, indicating that KCl was not used. Therefore, drilling mud types are not expected to have influenced the base line of the gamma ray measurements. Consequently, uncertainties on the presence of corrections for logging circumstances can lead to differences in calculated V_{cl} values.

Extreme fluctuations in the GR data can yield negative estimates of V_{cl}, which are practically not possible. These result in overestimations of porosity values, where GR is relatively high compared to the GR_{max}. Conversely, instances where V_{cl} exceeds 1 result in underestimations of porosity.

The V_{cl} calculation is strongly influenced by fluctuations in the GR log and therefore variations in lithology throughout the depth record. Assumptions on the correlation between GR values and lithology may be incorrect when the logging method affects GR values and when glauconitic sands are present. Details on the GR logging, obtained from the drilling report should be considered, when calculating V_{cl}.

Sonic (DT) log

Sonic measurements can be affected by cementation, water salinity, radial sensitivity of the sonic logging tool, sonic slowness of the matrix, and temperature. At shallower depths lower compressional wave velocities are observed due to less cementation between the matrix grains. This leads to relatively high porosity estimates for unconsolidated formations at shallow depths (Foster, 2007). Applying a compaction factor could correct for the lack of cementation at shallow depths (section 2.1.3; Geel & Foeken, 2021). This compaction factor is the main parameter that causes uncertainty in the porosity calculations from the sonic log (Geel & Foeken, 2021). Different methods, such as estimating compaction factors based on underlying shale layers or iteratively selecting factors from cross-plots of sonic porosity against density porosity calculations (Geel & Foeken, 2021), have been used in this study. Another widely used method to correct for compaction by adjusting the clay volume is described in this formula:

$$\mathrm{V_{cl}} = 0.083(2^{3.7 \cdot \mathrm{V_{sh}^*}} - 1)$$

Eq. 4.1

This formula is designed to correct for compaction in Tertiary unconsolidated rocks. The calculated clay volume is used to indicate porosity from the sonic log (Geel, 1999). However, this correction does not consider differences in sonic slowness resulting from varying borehole conditions. Compaction factors calculated from the underlying shale layer (section 2.1.3) vary a lot from factors obtained through iterative selection from sonic porosity against density porosity cross-plots (section 3.1.2 and Table 9.6). Therefore, it is recommended to estimate the compaction factor based on (i) cross-plots of the sonic against the density porosity and (ii) to use at least two different log data types to calculate porosity.

The formation around the borehole is invaded by mud filtrate in the first few centimeters (Foster, 2007). The sonic velocity has a depth of investigation from 12 cm to 1 m depending on the formation velocity, and a vertical resolution of 60 cm, which should be considered when comparing porosity estimates with lithology interpretations (Fig. 4.2; Geel, 1999). The sonic log data therefore include signals from the mud filtrate. The salinity of the mud filtrate is important when calculating the porosity.

The salinity was calculated using the mud filtrate resistivity and the formation temperature except for HBV-01, B30G4529, B49F0378, and DAPGEO_2_500m, where salinity data were not available (section 2.1.3). The small variations in salinity cause porosity differences of less than 1%. Differences in thickness of the invasion zone across the core record, ranging from 1 cm to tens of centimeters, could lead to variations in acoustic signals traversing the formation with and without mud filtrate at different depths (Foster, 2007). These variations were not corrected by selection of different sonic velocities of the fluid for different depths.

Lower sonic velocities at shallow depths influence the path of the sonic signals through the sediments, with radial sensitivity varying depending on log properties, formation characteristics, sonic logging tool type, and the bore-hole environment (Sørensen, 2015). Generally, slower acoustic signals at shallower depths will move faster through the mud compared to the formation, resulting in a higher mud signal for shallower depths (Chakraborty, Yadav, & Chatterjee, 2021; Foster, 2007; Serra, 1983). No correction is performed for differences in the mud signal over the depth-range, as this was out of the scope for this study.

The assumption of a DT_{ma} of quartz of 56 µs/ft is made due to the predominance of quartz sands in the Breda, Oosterhout, and Maassluis Formations. However, presence of clays and glauconitic sands introduces complexities (section 1.3). Glauconitic grains exhibit higher sonic slowness of approximately 105 µs/ft (Fig. 4.3; Hossain, Mukerji, & Fabricius, 2012), leading to potential overestimations of porosity when using a DT_{ma} of quartz of 56 µs/ft. This simplification on the matrix sonic slowness could result in slight over- or underestimations of porosity based on lithology.

Temperature controls the sonic velocity with a decrease of approximately 8 µs/ft for an increase from 5 to 25 °C for a sandy sediment layer (Carbó & Molero, 2000). No temperature corrections were performed on the sonic log data, which results in underestimation of the porosity at higher temperatures and depths by a few percentages.

Sonic slowness is influenced by numerous factors, often simplified to calculate the porosity. Most of these simplifications result in differences of a few percent compared to corrected values. The compaction factor has the most significant impact on porosity estimates and should be corrected using a density porosity and sonic porosity cross-plot.

Density (RHOB) log

When calculating the porosity from the density log, the assumption is made that the matrix consists of a single mineral (Foster, 2007). The matrix density of the main component, quartz, which is 2.65 g/cm^3 is used. However, also glauconite and clays are present over the depth interval analyzed in different wells (section 1.3). The density of glauconite ranges from 2.4-2.95 g/cm^3. Using the glauconite density of 2.67 g/cm^3 as the matrix density, could result in porosity differences of approximately 1%. Therefore, using the quartz density provides a reasonable approximation of porosity.

The fluid density, which depends on the salinity, is calculated from the resistivity of the mud filtrate and formation temperature like the fluid sonic slowness (section 2.1.3). The density logging tool has a higher depth of investigation compared to the sonic logging tool, resulting in less influence of mud filtrate density on the measured density log (Fig. 4.2). For selected wells with density logs, the fluid density was estimated to be 1.0 g/cm^3 due to the relatively low salinity of fresh-water drilling mud (Table 9.7). Because of the higher depth of investigation for the logging tool, the salinity of the formation water has a larger influence on the density porosity calculation. Based on combining two

databases containing salinity measurements for Paleogene sediments in Smit (2022) at 800 m true vertical depth (TVD) the salinity is approximately 30,000 ppm, which compares to a fluid density of 1.0 g/cm^3.

Consequently, despite lithology and salinity differences, the matrix density estimate of 2.65 g/cm^3, and the fluid density estimate of 1.0 g/cm^3 introduce low uncertainty in the porosity calculation.

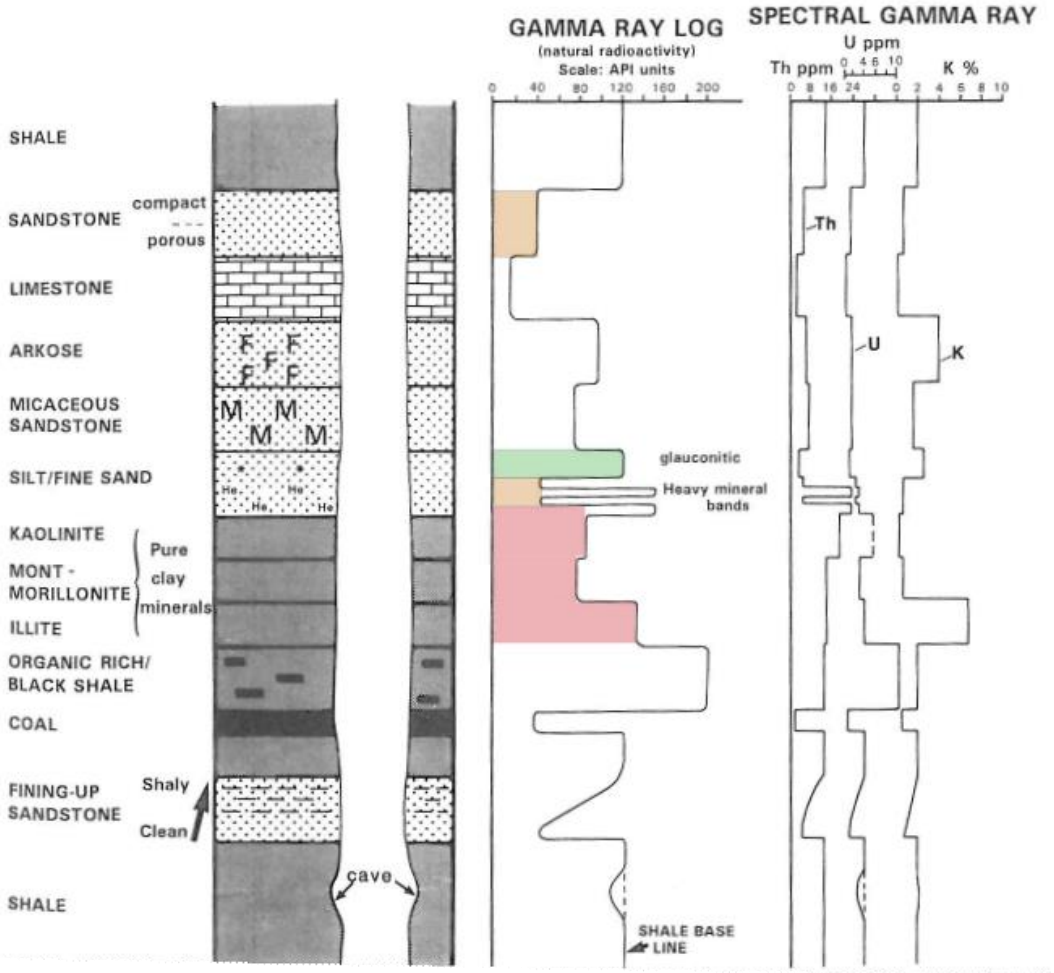

*Fig. 4.1 Gamma ray (GR) log values in gAPI and thorium (Th), uranium (U), and kalium (K) concentrations in ppm for different lithologies. The orange planes highlight the GR for sandstones, the red plane for pure clays, and the green plane for glauconitic sand. * = glauconite. After Rider (2002). The gamma ray values are high for glauconitic sands (green) compared to quartz sands (orange). GR values of glauconitic sands correspond to the values for clays (red).*

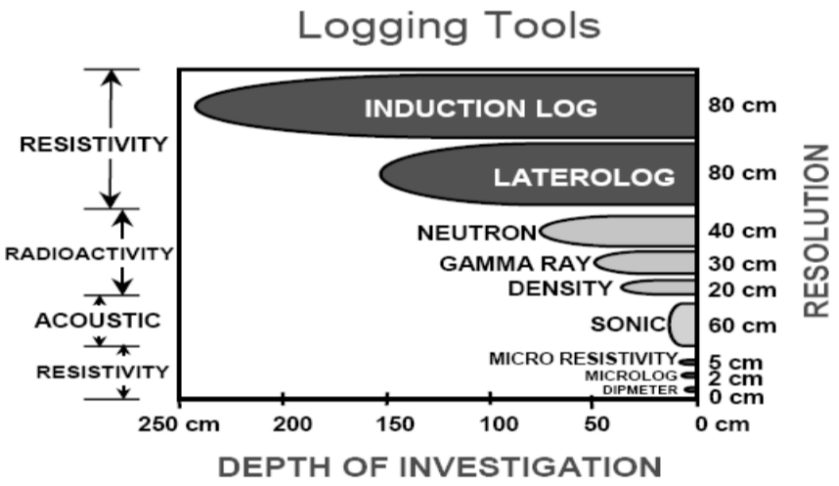

Fig. 4.2 Depth of investigation beyond the borehole and vertical resolution of different logging tools (Bond et al., 2010).

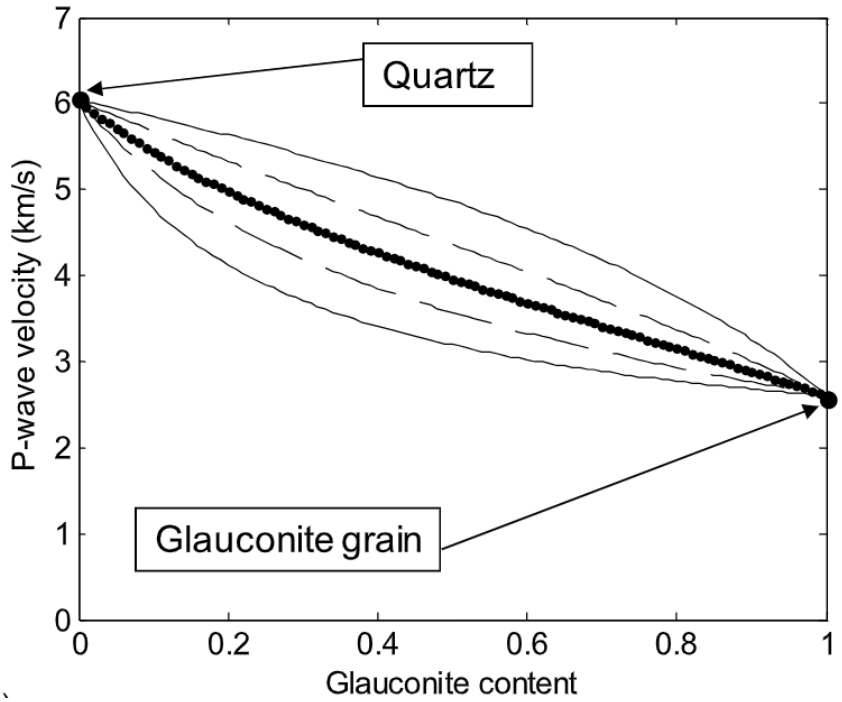

Fig. 4.3 P-wave velocity (km/s) variations covering the range from pure quartz to glauconite (Hossain, Mukerji, & Fabricius, 2012). Higher glauconite content results in a lower p-wave velocity.

4.1.2 Quantitative match with lithology

Qualitative comparison of the estimated porosity with lithology are described for each selected well in section 3.1.3. To provide a comprehensive overview of porosity estimates for different lithologies and depth groups, the porosity calculations are plotted in Fig. 4.4 based on GR values. Sand is interpreted at gamma rays below 30 gAPI, clayey sand between 30 gAPI and 60 gAPI and clay above 60 gAPI (Fig. 4.4). The division of lithologies based on GR measurements of well B30G4529 with high-quality data is simplistic, as more detailed lithology research based on the selected shallow wells was not possible due to time restrictions. Additionally, it should be mentioned that GR measurements are incorporated

into the calculations of sonic and density porosity. As most lithology interpretations in nearby shallow wells are based on the gamma ray and for time efficiency, these lithology data are not considered in this overview.

The scatter of the data is significant, which is in line with the earlier mentioned error range (section 3.1.2). Porosity values present in the box (50% of the estimates) for sand are within the range of ~35-45%, for clayey sand of ~10-30%, and for clay of ~15-20% (Fig. 4.4). 50% of the sand porosity estimates calculated from log data fall within the effective porosity range of 16-46% for sand. 50% of the clay porosity estimates are higher than the effective porosity range of clay of 1-18% (Woessner & Poeter, 2020).

For sand and clayey sand an overall negative trend is visible with increasing depths, which could be explained by compaction (Fig. 4.4). Clays do not show a negative trend with increasing depth (Fig. 4.4). Latter trend can be explained by the properties of clay particles, which are less prone to grain rearrangement and compaction when compared to sand particles (Essen, 2022). Compaction-related reduction in effective porosity could therefore be less significant in clay-rich formations. However, total shale porosity shows a faster decrease with increasing depth and compaction compared to sands (Fig. 9.2). The effective porosity of clays is relatively low compared to the total porosity due to the poor interconnection of the pore spaces. Therefore, total porosity should not be compared directly to effective porosity estimates (Meegoda & Gunasekera, 1992).

The clayey sands within the depth range of 400-500 m show lower effective porosity estimates than calculated for the clays. This difference may be attributed to the deeper position of the clayey sands within the well profiles. The clayey sands show a large range of porosity estimates for each depth range. This could be caused by a great mix of lithologies within the classified groups based on GR, as sediments of the Upper North Sea group include large heterogeneity in lithology (section 1.3). The lithology could be classified in more detailed groups based on more specific clay content and grain sorting using the gamma ray log.

In the clays present within the 0-100 m depth range a large amount of negative outliers occur, primarily associated with very high GR values in KTG-01, leading to an underestimation of the porosity value (section 4.1.1). The minor differences in porosity estimates across different depth ranges within the clay lithology could be explained by compaction, but also by variations in clay mineralogy (Wang et al., 2016).

Moreover, the range of the porosity estimates for the 0-100 m depth ranges of all lithology groups are high compared to the depth ranges at larger depths for the same lithology group (Fig. 4.4). These larger ranges could be caused by limitations of the method to calculate porosity based on the sonic log at these shallow depths, because this method was designed for consolidated materials at much higher depths (section 2.1.3; Geel & Foeken, 2021). Correction using a compaction factor may be insufficient for very shallow depths in the upper 100 m of the subsurface. Furthermore, log data could have lower quality in this shallow depth-range, which results in high ranges of porosity estimates.

Overall, the sonic porosity estimates show good correlation with different lithology types. The number of outliers is high, which could be due to uncertainties in the log data (section 4.1.1). Sand and clayey sand show a negative trend in the calculated porosity to higher depth ranges, which is expected because of compaction. The lack of this trend for clays could be explained by difficulties in rearranging clay particles.

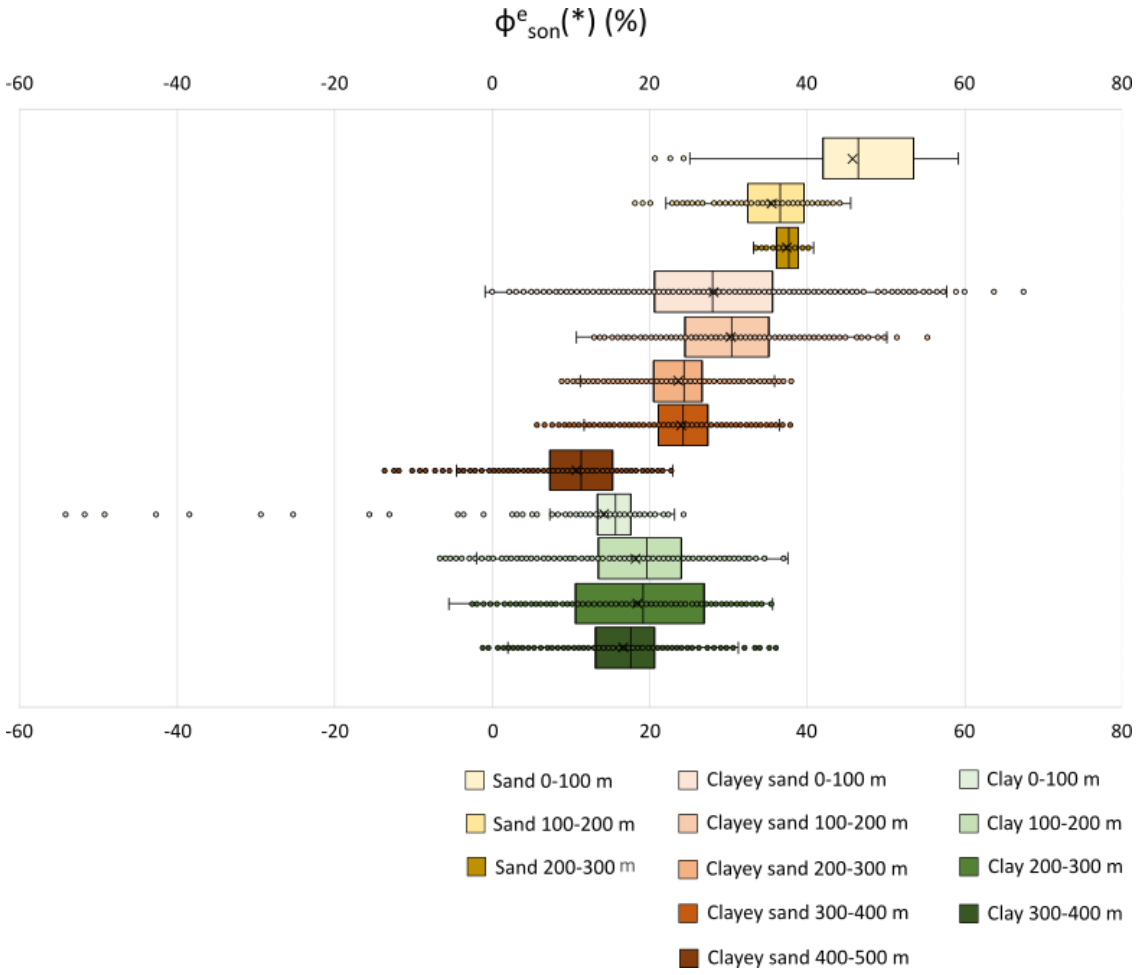

Fig. 4.4 Box and whisker plot showing the (corrected) sonic porosity estimates per lithological group and depth group. Sand: GR < 30 gAPI, clayey sand: 30 gAPI < GR < 60 gAPI, clay: GR > 60 gAPI. Wells B49F0378 and DAPGEO_2_500m are not included in this overview, because of questions on the data quality. Data of the following wells were included per depth range: 0-100 m -> WDL-01, HBV-01, JPE-01, KTG-01, and RLO-01; 100-200 m -> HBV-01, JPE-01, KTG-01, RLO-01, and B30G4529; 200-300 m -> HBV-01, NWK-01, JPE-01, and B30G4529; 400-500 m -> HBV-01. An overall negative trend in porosity estimates is visible for increasing depth-ranges and lithology groups including more clay. The clayey sand and clay groups show a large range in porosity estimates from calculations based on log data. The upper 100 m subsurface for all lithology groups show a high porosity range.

4.1.3 Overall quality

The process of calculating porosity from sonic or density logs involves numerous steps, leading to significant error ranges (section 3.1.2). These calculated error ranges of up to ~80% include porosity estimates below 0% and above 46% (Fig. 3.2). These estimates are not expected for sands and clays, whose effective porosity falls within ranges from 0-46% and 0-18%, respectively (Woessner & Poeter, 2020). The large error ranges represent potential outcomes when no strict criteria are established for minimum and maximum porosity and when outliers in log data are considered. Therefore, these error ranges are overestimations. However, they highlight the uncertainty in porosity calculations based on one log data type.

Variations in porosity calculations are visible in the number of outliers of porosity estimates for different lithologies (Fig. 4.4). This variability suggests that interpretations of porosity estimates

derived from a single type of log data can vary widely. Consequently, relying solely on either sonic or density log data to estimate effective porosity values is not recommended. This method can be used to discover trends in porosity and compare porosity values within the same well. To enhance the reliability of these calculations, it is recommended to correct the compaction factor used in sonic log-based porosity calculations by optimizing the fit in cross-plots of porosity estimates calculated from different log types. A strong correlation between porosity data calculated from sonic and density logs indicates good quality of the porosity results.

4.2 Experimental porosity estimates

The effective porosity estimates, measured using a pycnometer, do not show a general trend for samples 1-5 with increasing load. The total porosity, calculated from the measured displacement, shows a decrease with increasing load (Table 3.4). This discrepancy is remarkable since both porosity estimates were obtained under identical conditions measuring the same samples. Compaction increases with depth and results in a decrease of the porosity with increasing depth (section 1.5; Alberts, 2005; Hantschel & Kauerauf, 2009). The negative trend in the total porosity calculations matches with the expected porosity decrease due to compaction. However, the results of the effective porosity cannot be explained by this process. Potential influences on the experimental porosity estimates may include sample preparation procedures or factors encountered during the experiment (section 4.2.1). Uncertainties in the lithology of the samples complicates the interpretation of the measured porosity data (sections 3.2.1 and 4.2.3). Moreover, the difference between effective and total porosity should be considered, when interpreting these experimental porosity data (section 4.3). The following sections discuss the actions and potential errors preceding and during the experiment, which could contribute to inaccuracies in porosity measurements (section 4.2.1 and 4.2.2). Furthermore, the lithology of the samples and their link to porosity data is discussed (section 4.2.3).

4.2.1 Possible causes of errors in effective porosity measurements by a pycnometer

Several factors in sample preparation could have affected the effective porosity measurements by the pycnometer. Sawing pieces of the core, from which the samples were collected, could have altered the grain packing and consequently the porosity within the pieces. Additionally, protruding the samples and transferring these into the aluminium casing could also change the grain packing (Essen, 2022). The final sample length of ~7.4 cm, matching the length of the aluminium casing, complicates positioning the pressure pieces on the sample in a manner that allowed them to move along the aluminium casing and apply pressure evenly (section 2.2.2). Therefore, some pressure is applied to the sample to facilitate fitting the pressure pieces into the aluminium casing before transferring the sample to the UCS device. These manipulations may have slightly altered the original fabric. The displacement during these manipulations is up to a few millimeters, potentially causing a porosity decrease of a few percentages compared to the original sample (section 4.2.2).

Furthermore, the pycnometer measures the matrix volume of the sand based on pressure differences between the sample and the reference chamber (section 2.2.3). For accurate measurement, the sample must be completely dry, so that helium can replace the space between grains without obstruction from water. Although the samples were dried overnight at 60 °C in an oven, the drying method deviated from the European norm CEN ISO/TS 17892-2. This norm recommends drying samples in an oven for 24 h at 105 °C and is used in the determination of the dry volumetric mass in Buma et al. (2021). The shorter drying duration at lower temperatures raises uncertainty whether all water evaporated from the sample. Additionally, the presence of the aluminium casing, may have

obstructed evaporation of water from the sample, which could have resulted in residual moisture. When water is present during measurements of the matrix volume in the pycnometer, matrix volumes are overestimated, because helium cannot fully intrude all pore spaces. Moreover, the aluminium casing might prevent complete helium saturation of the pore spaces, because helium can only flow into the sample from the top down (Fig. 4.5). Eventually, this will result in lower porosity estimates (section 2.2.3).

The irregular edge of the sample, cut with a knife after placing the sample into the aluminium casing, introduces uncertainties in sample length and, consequently, total sample volume. A difference of 1.0 mm in input for the sample length in porosity calculation based on matrix volume measured by a pycnometer could result in 1.0% change in porosity. Consequently, uncertainties in the sample length significantly impact effective porosity uncertainty. Finally, as effective porosity is measured after applying pressure to the sample, any relaxation of the sample under surface pressure might lead to higher porosity estimates.

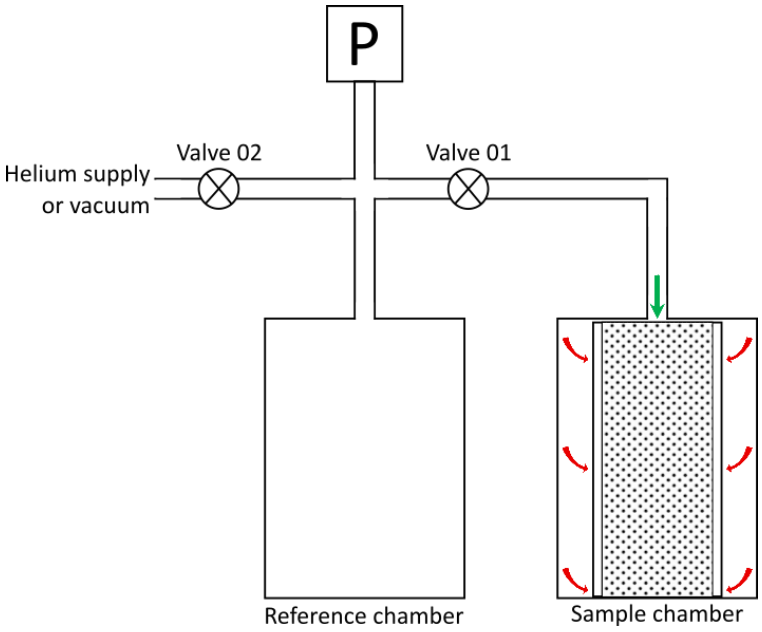

Fig. 4.5 Schematic overview of the pycnometer set-up including a reference chamber, sample chamber, pressure gauge, and valves. The sample is surrounded by the aluminium casing and parafilm at the bottom when located in the sample chamber of the pycnometer. The red arrows show the flow of helium that cannot intrude the sample because of the surrounding aluminium casing. The green arrow shows the path through which helium can enter the sample. The obstructed flow of the helium into the pore spaces of the sample could result in underestimation of the porosity.

4.2.2 Possible causes of errors in total porosity calculated from the measured displacement

The total porosity calculated from the displacement that is measured during increasing pressure in the UCS device, is subject to influences like to those described in section 4.2.1. Sawing pieces from the core and fitting the pressure pieces on the sample could have caused structural differences within the samples, potentially resulting in a decrease of total porosity estimates. Furthermore, uncertainty regarding the individual sample length complicates total porosity calculations, because the pre-pressure volume is used to calculate total porosity changes for different stresses (section 3.3). 1.0 mm difference from the original sample length results in a change of the total porosity change of only

0.05%. However, other factors in this method of porosity determination could impact total porosity calculations resulting in differences up to 7%.

Variations in the time between sample saturation and pressurization, due to dependence on CT scanner availability, may cause differences in sample saturation levels and water pore pressures throughout the experiment. Although samples were stored in a fridge with parafilm before pressurizing, this could influence porosity changes with increasing pressure, as pore fluid pressures counteract the compaction process (Smith, 1971).

The decrease in dry sample weight after pressure application suggests samples loss during experimental steps up to 9.2 gr (Table 4.1). Losses likely occurred during saturation, as fine sand and silt particles (<82 µm) may pass through nettings and sieve meshes (82x82 µm; sections 2.2.4 and 2.2.6). Additionally, sample loss may occur during removal of nettings and sieve meshes with some sample remaining in aluminium cups, in which CT-scans were performed. Saturation likely resulted in significant sample loss, evidenced by sand accumulation in the aluminium cups, though this loss could not be quantified due mixing of different samples per cup. Estimated losses from nettings, sieve meshes, and aluminium cups in between CT-scanning range from 2-4 gr (Table 4.1). Using the density of quartz of 2650 kg/m^3 the volume of the lost samples could be calculated and consequently porosity changes up to 6.7%. These porosity changes caused by sample loss are relatively high compared to the total porosity changes calculated from the displacement, which range from 8% to 15%, introducing large uncertainty in total porosity data (Table 4.2). This sample loss could explain the offsets in total porosity-depth graphs between the data from experiment up to 15 MPa and 30 MPa, shown in Fig. 3.7, though these could also result from errors in combining different datasets (section 3.3).

Adding different displacement measurements together within experiments up to 15 and 30 MPa, was performed based on the measurements with a displacement-controlled speed of 0.0100 m/s (section 3.3). This results in relatively smooth trends with minor depth peaks at depths, where data were added together (sections 2.2.6 and 3.3). These peaks could be caused by a little decrease in stress when pressurizing is paused to adjust the LVDT's. This method could not be applied to compile data from experiments up to 15 and 30 MPa, because these data both contain a displacement-controlled speed of 0.0100 m/s. Therefore, these data are added together based on the continuation of the stress. This introduces uncertainty, as displacement may increase differently in experiments up to 15 MPa compared to 30 MPa due to second pressurization in the 30 MPa experiment. Therefore, offsets between the data of the two experiments could also be caused by adding these data together based on continuing stresses. Grain deformation could affect the measured displacement and contribute to potential overestimation of the porosity (section 1.5; Alberts, 2005). Although this process is absent in quartz grains within the mid-depth range, as critical pressures are reached from 75-380 MPa (Zhang, Wong, & Davis, 1990), the lower hardness of glauconite could result in grain deformation of glauconite within the mid-depth range (Díaz et al., 2003).

Especially the effect of sample loss should be considered when interpreting the calculated total porosity change.

Sample	1	2	3	4	5
Dry weight before pressure (g)	91.661	85.644	85.524	94.904	86.399
Dry weight after 30 MPa pressure (g)	85.561	79.084	82.037	88.477	77.169
Calculated dry weight loss (g)	6.100	6.560	3.487	6.427	9.230
Measured weight loss lost sample (g)	3.420	3.640	2.820	2.838	4.242
Saturated weight before pressure (g)	111.964	101.475	100.624	108.72	100.092
Weight saturated water before pressure (g)	20.303	15.831	15.100	13.816	13.693
Saturated weight after 15 MPa pressure (g)	104.091	97.515	-	?	91.242
Saturated weight after 30 MPa pressure (g)	99.211	92.275	97.574	102.13	88.612

Table 4.1 Measured weight of samples 1-5 before putting the samples under pressure, after applying 30 MPa of pressure, the calculated weight loss of the dry samples, and the measured weight loss of the samples by collecting the sand that was stuck in nettings, mesh sieves and aluminium cups. The saturated weights before, after 15, and 30 MPa are also displayed, together with the calculated weight of the saturated water.

Sample	1	2	3	4	5
Weight loss (g)	6.100	6.560	3.487	6.427	9.230
Volume loss (cm3)	2.30	2.48	1.32	2.43	3.48
Height (mm)	-3.3	-3.5	-1.9	-3.4	-4.9
Porosity change (%)	-4.4	-4.7	-2.5	-4.6	-6.7

Table 4.2 Calculated sample volume loss (cm^3) based on a quartz density of 2650 kg/m^3 and the height of lost samples within the aluminium casing (mm). Using the same method as described in section 3.3 the total porosity loss based on the height of the lost sample was calculated.

4.2.3 Lithology of the samples

The lithology interpretations of samples 1-5 from core descriptions are questioned, because of differences in lithology interpretations from the Liessel core description and the more reliable laser particle size analysis data (section 3.2.1). In a cross-plot, the indicated and measured lutum, silt, sand, and gravel percentages from the core description and the laser particle size analysis are compared. These values do not correlate well, with the core description data often underestimating lutum and silt percentages and overestimating sand percentage. Therefore, based on nearby laser particle size analysis data, samples 1 and 4 are further interpreted as clayey sands according to NEN5104 (Fig. 9.6), with particle percentages outlined in Table 4.3. For samples 2, 3, and 5, which have a larger distance to the reference data points of the laser grain size particle analysis data, the lithology interpretation of the core description is retained, as lithology can vary over short distances (Table 2.3 and Table 4.3). It should be noted that these grain size estimates are less precise than those obtained from laser particle size analysis data. An overview of the lithology estimates for samples 1-5, which are used in the following interpretations is given in Table 4.3. Samples 2, 3 and 5 lack accurate data on grain sorting, as no particle size analysis data is present. Furthermore, samples 1-5 do not contain data on the grain sphericity. In this study porosity estimates can therefore not be correlated to grain packing of the samples, as accurate grain sorting and sphericity data are lacking.

Sample	Lithology	Depth range (cm)		M63	D50	LU (%)	SI (%)	ZA (%)	GR (%)	GLAU (%)
		Top	*Base*							
1*	Kz2	847	860		173	12.2	8.3	79.6	0	1 a 2
2	Sand	1675	1691	170		0	1	99	0	6
3	Sand	2188	2200	200		0	2	98	0	3
4*	Kz3	1582	1593		174	11.5	9.8	78.7	0	2
5	Zs1 (2789-2793 cm)	2789	2800	180		1	3	96	0	6
	Glauconitic sand (2793-2795 cm)					1	2	62	35	
	Zs2 (2795-2800 m)			160		1	14	85	0	6

*Table 4.3 Lithology interpretation, depth range, M63 and D50 of the sand fraction (µm), lutum (<2 µm) percentage, silt (2-63 µm) percentage, sand (63 µm – 2 mm) percentage, gravel (2-63 mm) percentage, and glauconite percentage, which is only based on core description data. The * indicates that the lithology interpretation and displayed data, with exception of the glauconite percentage, is based on laser particle size analysis data. The lithology codes are according to NEN5104 (Fig. 9.6).*

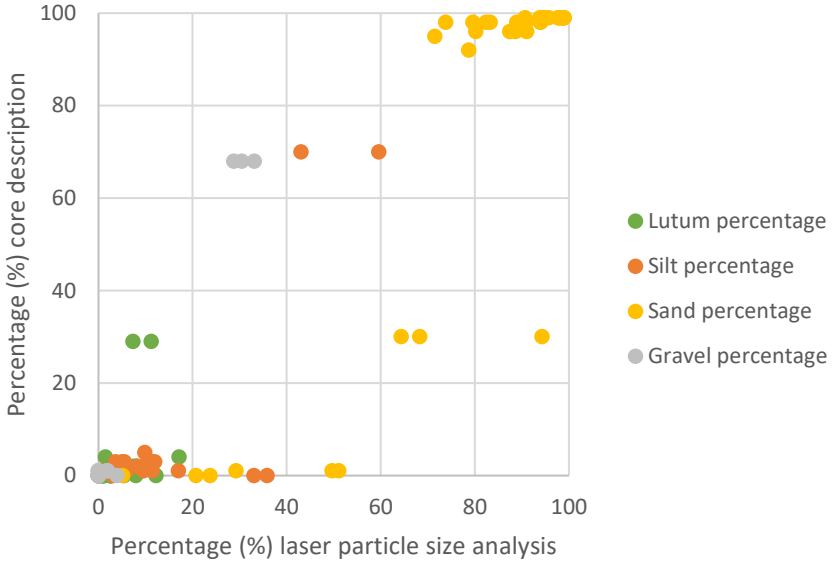

Fig. 4.6 Cross-plot between the lutum (<2 µm) percentage, silt (2-63 µm) percentage, sand (63 µm – 2 mm) percentage, and gravel (2-63 mm) percentage indicated in the core description and measurements based on laser particle size analysis. The core description data does not correspond to the laser particle size analysis data of the same samples. The core description data show higher estimates for sand percentages above 90% compared to laser particle size analysis data.

4.2.4 Overview of effective porosity estimates per lithological group

The effective porosity of the sand samples doesn't match the calculated effective porosity based on sonic log data, as for sandy clay and clayey sand there is a relatively good correlation (Fig. 4.7). Different interpretations of the lithology could cause this difference, as the sand groups in the well data include very clean sands (section 4.1.2). Sand samples 2, 3, and 5 are based on core description data, which are indicated to overestimate the sand percentage (section 4.2.3 and Fig. 4.6). Therefore samples 2, 3, and 5 may also be classified as a clayey sand. Samples 1-5 fit within the porosity range of clayey sands, with lower porosity values observed for sample 1 and 4, which exhibit higher lutum percentages, compared to samples 2, 3, and 5. The absence of a clear negative trend of the porosity estimates with

increasing depths for the sandy clay samples (Fig. 4.7) may be a result of errors in the effective porosity measurements (section 4.2.1). However, it might also be influenced by relatively high lutum percentages in the samples, which complicates grain rearrangement, and therefore show relatively constant porosity values with increasing depths (Essen, 2022).

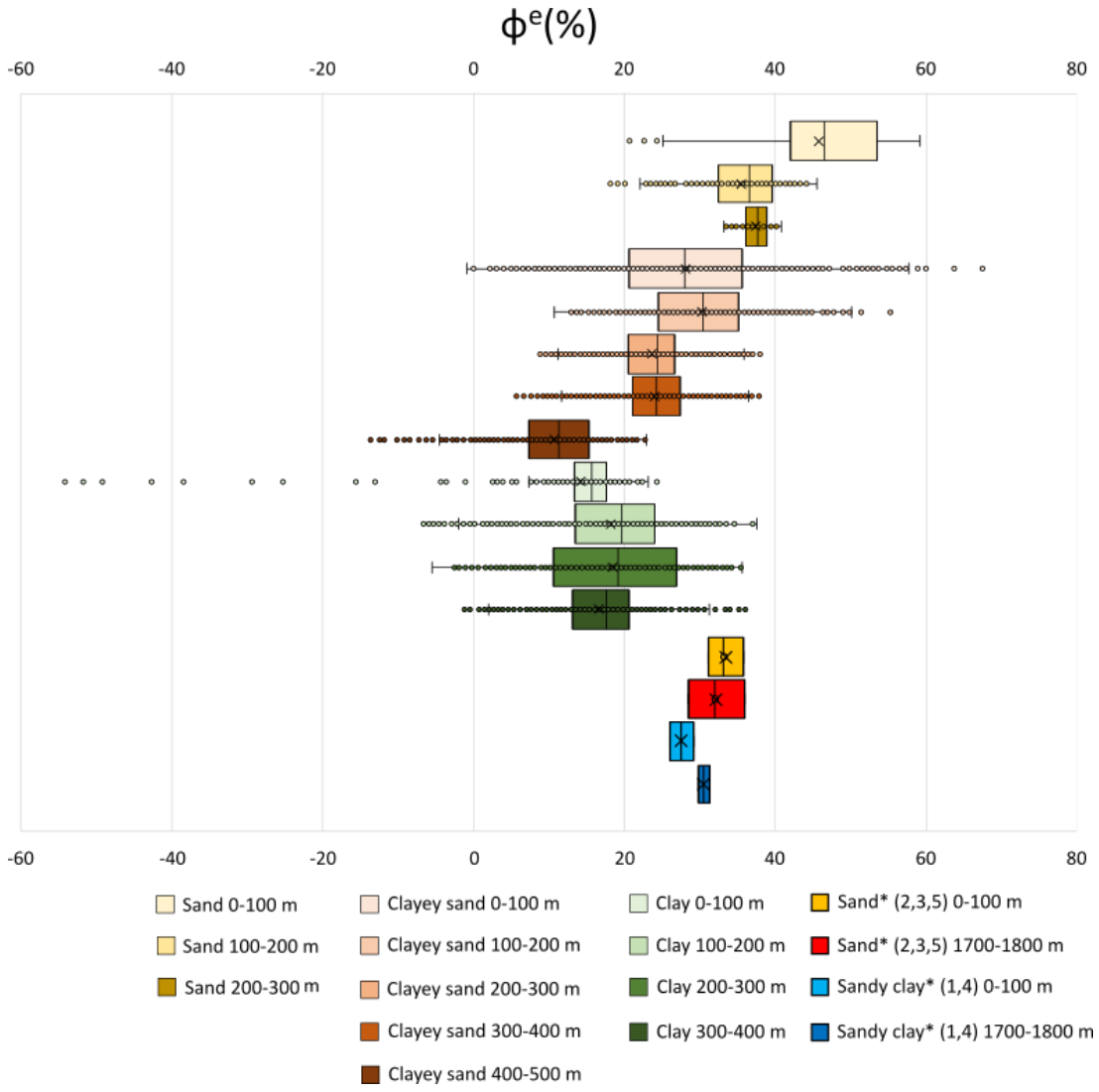

*Fig. 4.7 Box and whisker plot showing the (corrected) effective sonic porosity per lithological and depth group. Sand: GR < 30 gAPI, clayey sand: 30 gAPI < GR < 60 gAPI, clay: GR > 60 gAPI. Data of the following wells were included per depth range: 0-100 m -> WDL-01, HBV-01, JPE-01, KTG-01, and RLO-01; 100-200 m -> HBV-01, JPE-01, KTG-01, RLO-01, and B30G4529; 200-300 m -> HBV-01, NWK-01, JPE-01, and B30G4529; 400-500 m -> HBV-01. The effective porosity measured using a pycnometer for the sand samples 2,3 and 5 and clay samples 1 and 4 are shown for depth groups 0-100 m and 1700-1800 m and marked with a *. The lithology of these samples is based on core description data and laser particle size analysis (section 4.2.3). The depths of the sample data are calculated based on an overburden sediment density of 1770 kg/m^3. A general decrease of porosity values is visible with increasing depths and for samples, which contain more clay. The sandy clay of sample 1 and 4 is an exception on this trend, as higher porosity values are measured at larger depths.*

4.3 Comparison between different porosity data

The median of all porosity estimates for sands, clayey sand/sandy clays, and clays of the Upper North Sea Group ranges from ~11% to ~46% (Fig. 4.8). Compared to experimental data, calculated porosities from sonic log data show larger ranges (sections 3.1.2 and 4.1). The difference in the amount of data points should be noted, where the effective porosity calculated from the sonic logs include 500-1500 porosity estimates per depth range and lithology group against 2-15 porosity estimates for the experimental data. The (corrected) effective porosity estimates calculated from sonic log data for sand are generally higher and for clayey sand/sandy clay similar compared to the experimentally obtained porosity values (Fig. 4.8). The total porosity estimates measured with the falling head method are like the calculated estimates for sand, but deviate the most from calculated porosities for clayey sands/sandy clays compared to other experimentally derived estimates (Fig. 4.8). Again, varying definitions of lithology groups for different methods to indicate porosity should be noted, as lithology of porosity estimates from well data are indicated based on the gamma ray, as the experimental data are classified based on laser particle size analysis data and core description data according to NEN5104 (section 4.2.4). Overestimation of the sand fraction in core description data (section 4.2.3) could result in classification in sand, instead of clayey sand/sandy clay (Fig. 4.8). This could explain the relatively low porosity estimates for sand samples of the Liessel core compared to the clean sands with GR < 30 gAPI in the selected wells (Fig. 4.8). The clayey sand/sandy clay porosity calculated from the well data show a relatively good fit with the experimental data. However, these experimental results do not compare to the low calculated porosity range for 400-500 m depth in the clayey sand/sandy clay group (Fig. 4.8). The cause of the extreme low porosity values for this group is unknown.

Within the experimental porosity estimates the total porosity estimates measured using the falling head method are high (Fig. 4.8). This could be caused by differences in total and effective porosity definitions. Effective porosity is defined by the interconnected pore space of a sediment, as the total porosity is the ratio of the total void volume to the total bulk volume (Fig. 2.2 and Fig. 4.9; Gibb et al., 1984). In clean sands that lack clay bound water, total porosity is very similar to effective porosity (Al-Ruwaili & Al-Waheed, 2004). As sands in the Liessel core are doubted to be “clean” (section 4.2.3), comparison and combination of total and effective porosity estimates should be interpreted carefully. For sediments with a higher clay fraction, the effective porosity is expected to be lower than the total porosity, as more clay bound water can be present (Fig. 4.9). This could explain the higher total porosity estimates using the falling head method compared to the effective porosity estimates. Furthermore, this distinction in porosity type questions the quality of the total porosity data calculated from displacement data. The total porosity is based on a combination of the effective porosity measurements of the samples, which are used to indicate the surface porosity, and the calculated total porosity change (Fig. 4.8). The estimated total porosity values at larger depths are lower than the effective porosity measured with a pycnometer (Fig. 4.8), which is not in line with the expected higher total porosity compared to effective porosity. Uncertainties on the quality of this data, because of combining total and effective porosity data and sample loss throughout the experiment (section 4.2.2), could explain these differences. Total porosity estimates using the falling head method on samples from the Liessel core fit into the large porosity data range for clayey sands from the TopIntegraal program of samples from the upper 30-50 m in the North of the Netherlands (Fig. 4.8 and Fig. 4.10; (Buma et al., 2021). Total porosity estimates based on combining the measured effective porosity as surface porosity and the total porosity change calculated from displacement, are low for both sand and clayey sand/sandy clay samples compared to an overview of total porosity estimates, collected as

part of the TopIntegraal program (Fig. 4.10 and Fig. 4.8). This deviation contributes to questioning the quality of these data.

Consequently, the different methods result in different porosity estimates. Comparison is complicated because of the relative uncertain and heterogenous lithology of the samples and the large porosity range of clayey sands/sandy clays. As the Upper North Sea Group lacks clean sands and pure clays (section 1.3), it could be interesting to distinguish between lithology in more detail to better indicate lithology per lithology, but this is out of the scope for this study due to time constraints. Furthermore, differences in total and effective porosities, which are measured using different methods, and the limited amount of well and experimental data complicate the comparison of the porosity outcome. Questions arise on the quality of the total porosity estimates from the displacement and effective porosity estimates used as the surface porosity. Furthermore, the low porosity estimates at larger depths for the calculated clayey sand values from well data and high porosity estimates at larger depths for the effective porosity measurements by the pycnometer, cannot be explained.

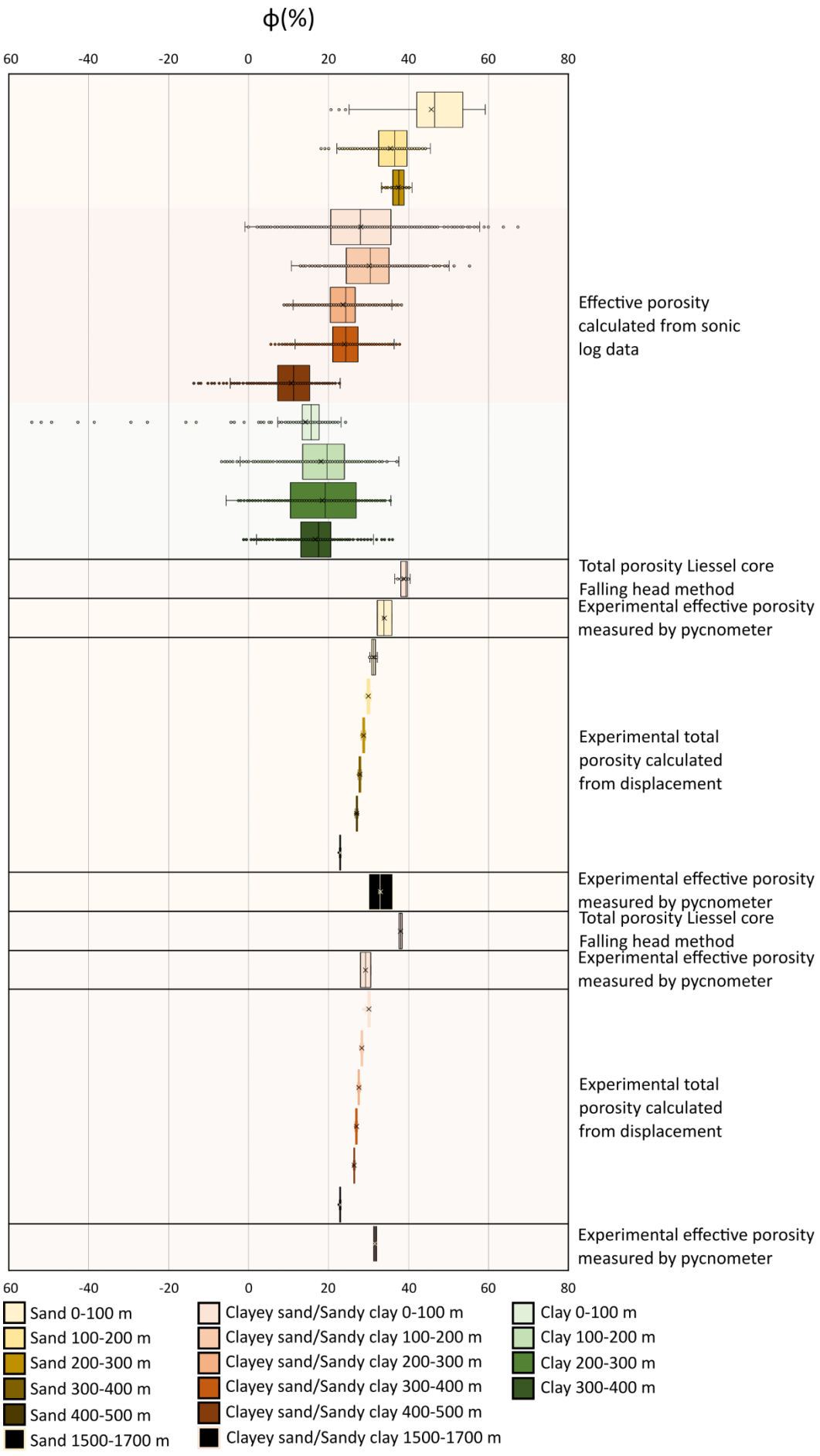
ϕ(%)
60
-40
-20
0
20
40
60
80
Effective porosity calculated from sonic log data
Total porosity Liessel core Falling head method
Experimental effective porosity measured by pycnometer
Experimental total porosity calculated from displacement
Experimental effective porosity measured by pycnometer
Total porosity Liessel core Falling head method
Experimental effective porosity measured by pycnometer
Experimental total porosity calculated from displacement
Experimental effective porosity measured by pycnometer
Sand 0-100 m
Sand 100-200 m
Sand 200-300 m
Sand 300-400 m
Sand 400-500 m
Sand 1500-1700 m
Clayey sand/Sandy clay 0-100 m
Clayey sand/Sandy clay 100-200 m
Clayey sand/Sandy clay 200-300 m
Clayey sand/Sandy clay 300-400 m
Clayey sand/Sandy clay 400-500 m
Clayey sand/Sandy clay 1500-1700 m
Clay 0-100 m
Clay 100-200 m
Clay 200-300 m
Clay 300-400 m

Fig. 4.8 Box- and whisker plot including effective porosity data, calculated from sonic log data (sections 3.1 and 4.1), total porosity of samples from the Liessel core, using the falling head method (section 3.1.1), effective porosity of the selected samples 1-5 measured with a pycnometer (sections 3.2 and 4.2.4), and the total porosity of the selected samples 1, 2, 4, and 5, calculated from the displacement (section 3.3). Porosity estimates based on sonic log data of wells HBV-01, JPE-01, KTG-01, NWK-02, RLO-01, WDL-01, and B30G4529 were used within this overview, and when present, the corrected sonic porosity estimates are displayed. For the calculated effective porosity estimates from log data the lithological groups are based on the GR: Sand: GR < 30 gAPI, clayey sand: 30 gAPI < GR < 60 gAPI, clay: GR > 60 gAPI (section 4.1.2). Lithological groups for the experimental data are classified with the NEN5104 classification based on core descriptive data for samples 2, 3, and 5 and laser particle size analysis data for samples 1 and 4 and the samples of the Liessel core, of which porosity was indicated using the falling head method. The background colour of the graph indicates the lithology with yellow for sand, red for clayey sand/sandy clay, and green for clay. The experimental total porosity calculated from displacement is based on a surface porosity of the effective porosity measurements by a pycnometer before applying pressure and the calculated change with increasing depth. Pressure in the experimental data was converted to depth using an overburden sediment density of 1770 kg/m^3. Lighter colours indicate shallower depth-ranges. The experimental data for samples classified in the sand lithology group are low compared to porosity estimates from calculations based on log data, with exception of the total porosity estimates using the falling head method. The experimental data for the clayey sand lithology group are like porosity estimates from calculations based on log data, with exception of the total porosity using the falling head method, which is higher. Overall, porosity estimates are lower with increasing depths and lithology groups, which contain higher clay content.

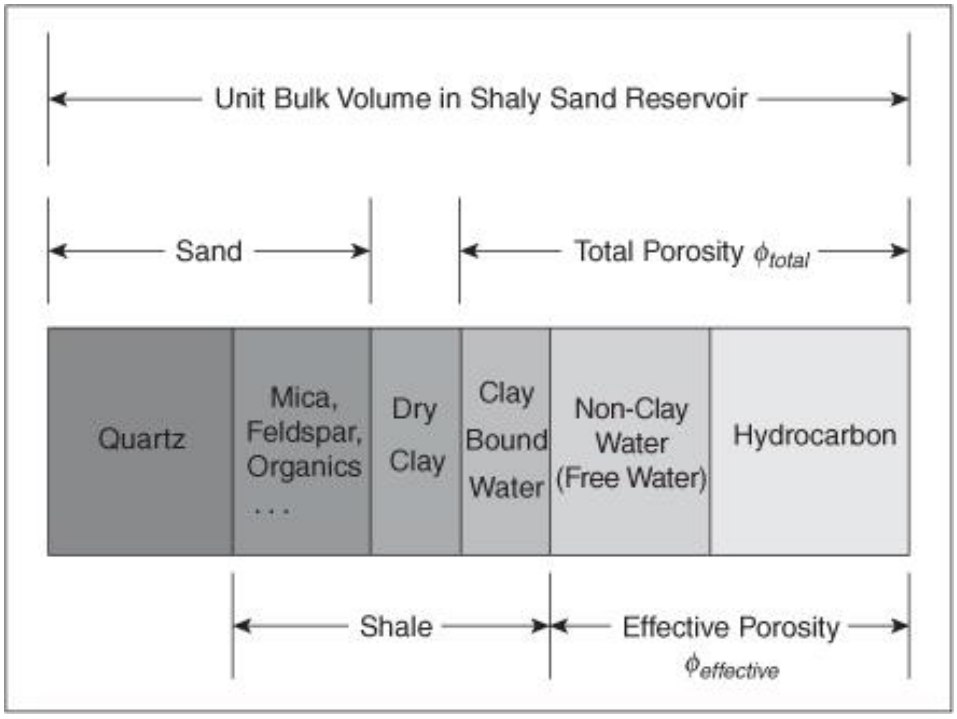

Fig. 4.9 Schematic overview of the Unit Bulk Volume in a shaly sand reservoir showing the total and effective porosity (Al-Ruwaili & Al-Waheed, 2004). The difference between the total and effective porosity is shown, as the clay bound water is included in total porosity, but not in effective porosity.

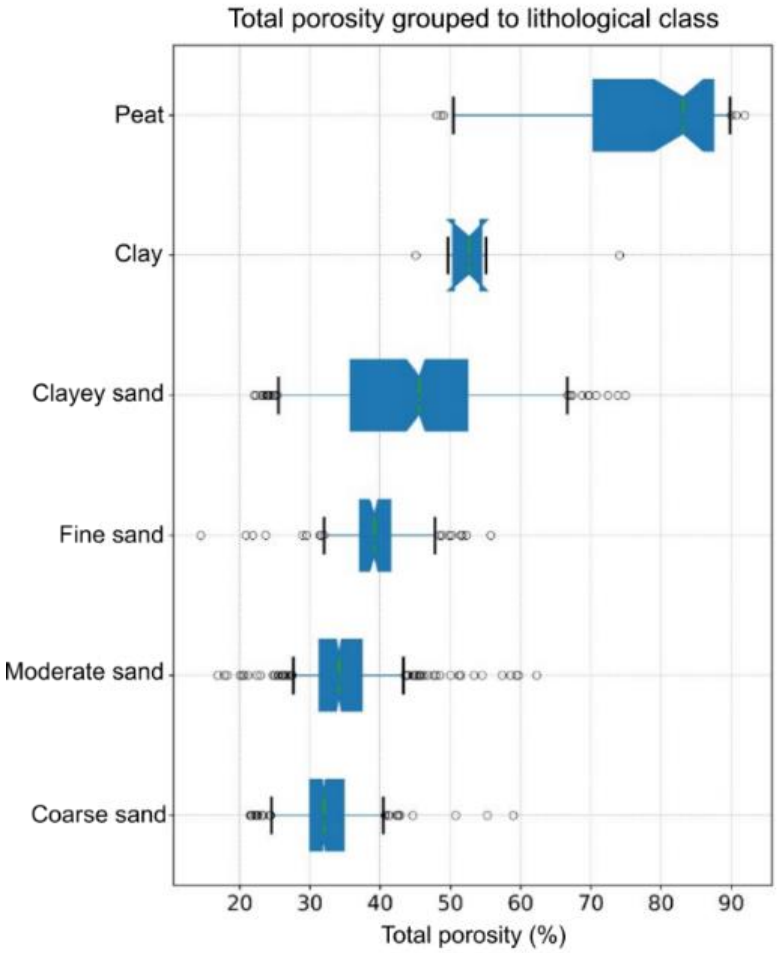

Fig. 4.10 Overview of total porosity estimates using the falling head method per lithological class from samples of 30-50 m depth in the TopIntegraal program (Buma et al., 2021). The total porosity measurements are lower for sand compared to clay. The clayey sand class has a large range of porosity measurements.

4.4 Influence of compaction on porosity-depth relation

The different outcomes per method complicate the possibility to generate a general porosity-depth relationship for unconsolidated sediments of the Upper North Sea Group. Therefore, the porosity-depth relationship per method is compared to Athy's curve (section 1.5.3) currently used for Upper North Sea sandy sediments in unpublished data of ThermoGIS (Fig. 4.11; Veldkamp, 2024). This relation is described using Eq. 1.5. It should be noted that this curve is very uncertain due to the lack of porosity estimates of good quality.

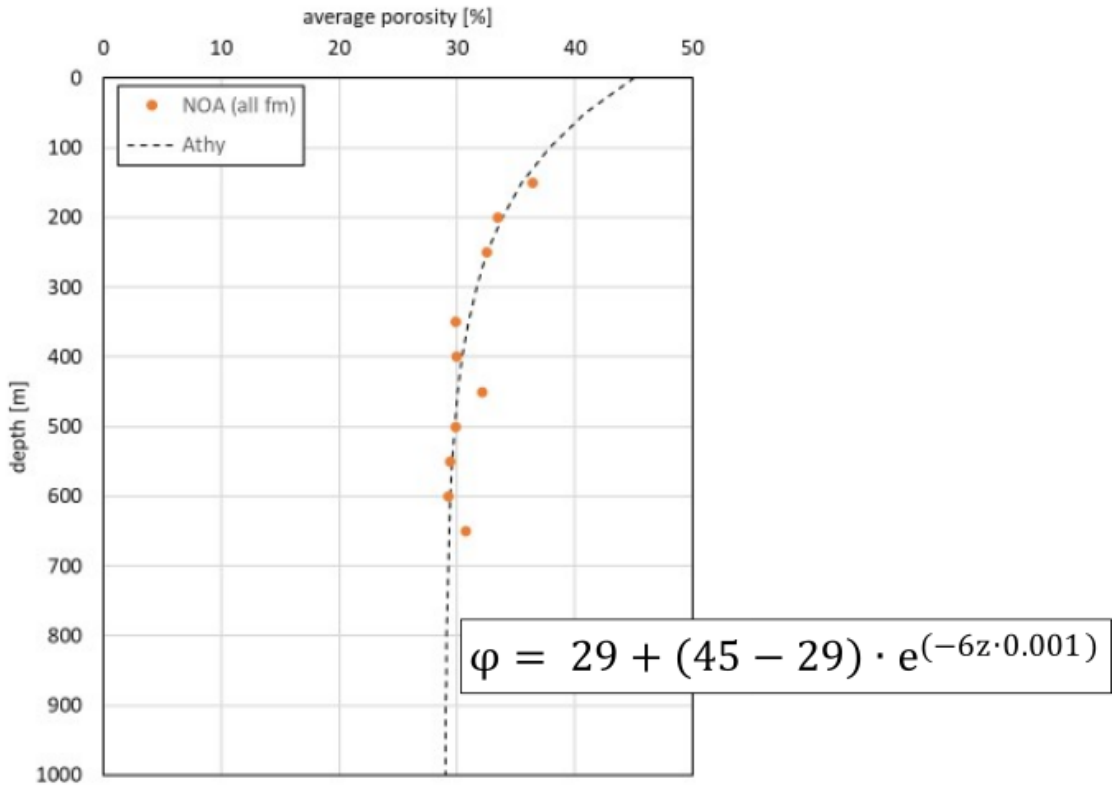

Fig. 4.11 Athy's curve fitted for porosity estimates of sands in the Upper North Sea Group (Veldkamp, 2024). The rate of porosity decrease declines with increasing depth. The data on which this curve of Athy is based include high uncertainty.

The sands with a GR lower than 30 gAPI show a relatively good fit with Athy's curve apart from higher porosity estimates for JPE-01, and some higher estimates for KTG-01 and B30G4529 (Fig. 4.12). The other porosity calculations and experimental porosity estimates do not have a good fit with the currently used curve of Athy for sands in the Upper North Sea group (Fig. 4.12). The clayey sands with a GR between 30 gAPI and 60 gAPI show a relatively large range of porosity estimates as discussed in sections 4.2.1 and 4.3. The porosity estimates in wells RLO-01 and B30G4529 include data points that have a relatively good fit with Athy's curve (Fig. 4.12). These data points may represent lithologies dominated by sand, thereby resulting in a better fit, but more detailed distinction between lithologies is required to explain the differences in fit with Athy's curve. The porosity calculations for clays with a GR above 60 gAPI are relatively low compared to Athy's curve for sand, which would be expected from a lithology that has a lower effective porosity compared to sand (Fig. 4.12). Tweaking of the parameters in Athy's curve to achieve better alignment with the porosity calculations from the wells is very difficult due to the wide range. After determining lithology variations in the wells in more detail, data for sands can be integrated into available porosity estimates of Upper North Sea Group (Fig. 4.11) to improve the compaction curve for the Upper North Sea Group.

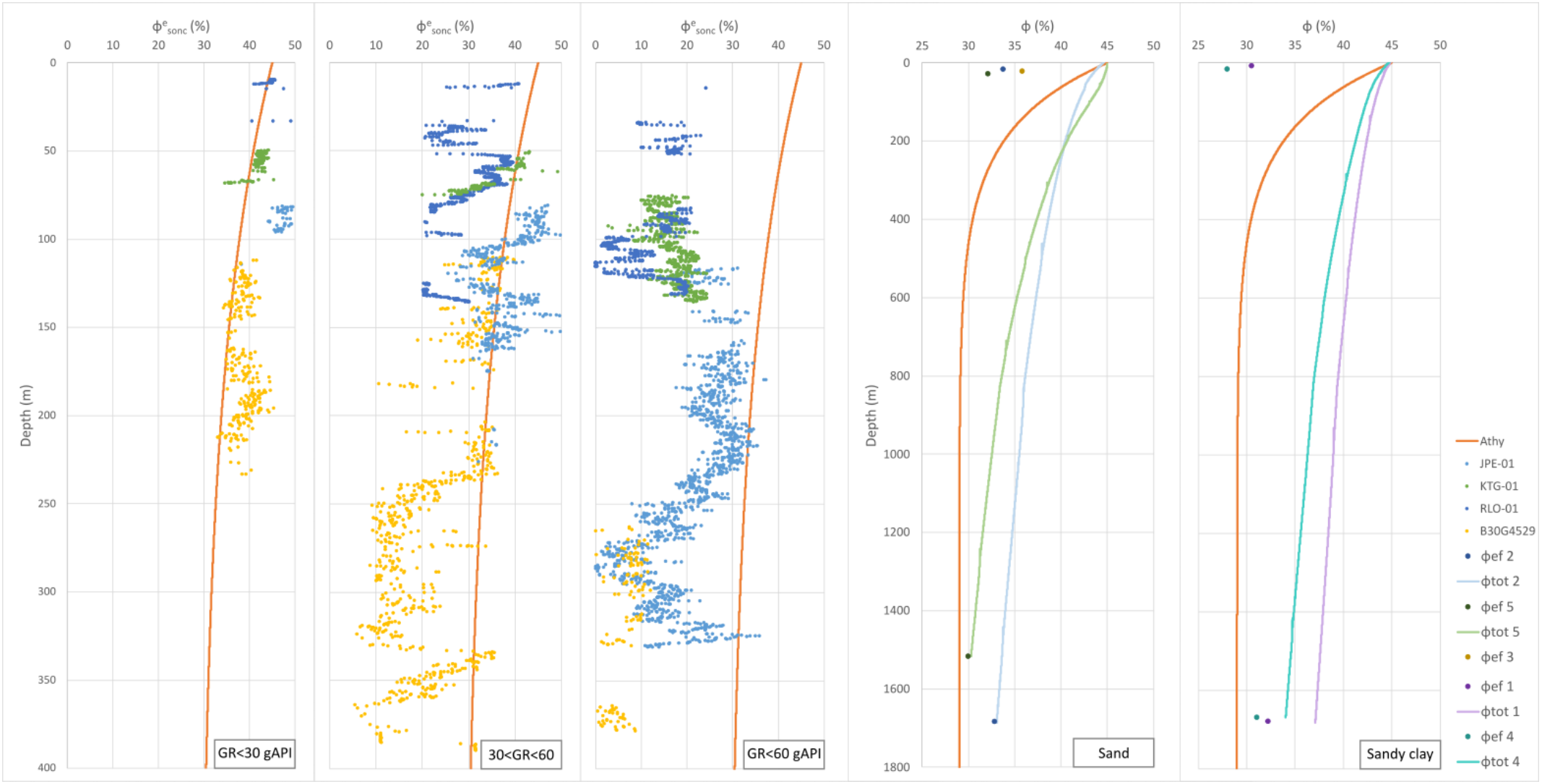

Fig. 4.12 Porosity-depth relations based on calculations from the selected well data and experimental porosity estimates for different lithologies, plotted with Athy's curve used for sands in the Upper North Sea (red line). The corrected sonic porosity from wells JPE-01, KTG-01, RLO-01, and B30G4529 for sand - GR<30 gAPI, clayey sand/sandy clay - 30 gAPI<GR<60 g API, and clay – GR>60 gAPI are plotted in different graphs. The effective porosity and total porosity change, based on a surface porosity of 45%, are plotted for samples 2, 3, and 5, which are interpreted as sands, and for sample 1 and 4, which are interpreted as sandy clays. In the experimental porosity data graphs, depth was calculated from stress using an overburden sediment density of 1770 kg/m^3. The porosity estimates calculated from log data for the sand group (GR<30 gAPI) show the best fit with Athy's curve and for the clayey sand group (30<GR<60) show parts with a good fit. The porosity estimates calculated from log data for clays and experimental porosity data do not fit with Athy's curve.

Both effective and total porosity estimates for the sand samples 2, 3, and 5 do not fit Athy's curve (Fig. 4.12). It should be noted that the plotted curve of Athy is not based on data deeper than 700 m and comparison with other data below this depth should be performed with caution (Fig. 4.11). The effective porosity estimates of the sands near the surface are relatively low compared to the surface porosity of 45% for Athy's curve, as the effective porosity measurements at larger depths are high (Fig. 4.12). The total porosity declines less fast with increasing depth compared to Athy's curve. The uncertainty on the lithology, the porosity at the surface, and sand loss could explain different estimates than what would be expected based on the current used Athy's curve for sands in the Upper North Sea Group (sections 4.2.2 and 4.2.3). However, the large uncertainty in Athy's curve that is currently used could also cause differences with the experimental results. A remarkable detail regarding the total porosity against the depth for samples 2 and 5, when a surface porosity of 45% is estimated, is the good fit with the effective porosity estimates that were measured after applying the pressure (Fig. 4.12). Again, this raises questions on the quality of the effective porosity data measured by the pycnometer (sections 4.2.1 and 4.2.4). The sandy clay porosity data of samples 1 and 4 differ even more from Athy's curve, which is expected based on their lithology with a higher lutum percentage (Fig. 4.12). The experimental data, however, lack sufficient reliable data points to indicate Athy's curve for lithologies with low and high lutum percentages.

Consequently, the quality of the experimental data collected in this study are insufficient to indicate porosity-depth relations for unconsolidated sediments of the Upper North Sea Group. Hence, they also do not validate to adjust the currently used curve of Athy for sands of the Upper North Sea Group. However, the experiments add valuable porosity data of Upper North Sea Group sediments, given the present scarcity of measured data (section 6). A better understanding and indication of the uncertainty from the obtained experimental data is necessary to evaluate the currently used porosity-depth relation. The heterogenous lithology present within these formations complicate the process to expand the porosity dataset for relatively clean sands.

The effective porosity calculations based on well log data can be used to indicate porosity-depth relations of sediments in the Upper North Sea Group. Classification of calculated porosity estimates in more detailed lithology groups are required to confirm or adjust the currently used porosity-depth relation. Porosity data can be calculated based on log data required from new wells in the mid-depth range that include sediments of the Upper North Sea Group. With a higher amount of porosity estimates it may be possible to establish a reliable porosity-depth relationship for these sediments in the mid-depth range.

4.5 Quality of compressional wave slowness calculations

4.5.1 Comparison with sonic data selected wells

The calculated pressure wave slowness for samples 1, 2, 4, and 5 ranges from 50-70 µs/ft (~4900 - ~6100 m/s), excluding data from sample 1 subjected to 15 MPa pressure. This is lower than the DT values from the sonic logs of the selected wells, which exhibit a range of 150-200 µs/ft (~1500 - ~2000 m/s; Fig. 3.13). The compressional wave velocity for unconsolidated wet and dry sands ranges from 1600 m/s to 2400 m/s up to 20 MPa (Zimmer, 2004). In Carmichael (1989) the acoustic velocity of unconsolidated sands at the surface is indicated to be lower than 5200 m/s. These acoustic velocity estimates from the literature do not compare to the calculated compressional velocities of samples 1, 2, 4, and 5 (Fig. 3.13). The aluminium casing surrounding the samples explains the high velocity estimates, given that the compressional wave velocity of aluminium is approximately 6420 m/s.

Acoustic signals could have moved through both the samples and the aluminium casing. Because of the faster travel time of compressional waves through aluminium, the arrival times of the acoustic signal that were selected, likely indicate the arrival of the acoustic signal through the aluminium casing. Therefore, the calculated DT values do not reflect the sonic slowness of the samples. This also explains the relatively constant DT values for increasing depth, as there are minimal internal changes in the aluminium casing throughout the experiment, as pressure is applied to the sample.

4.5.2 Acoustic signal of sample

An alternative approach in calculating the pressure wave slowness of the samples was performed by selecting different arrival times. As modelling different influences on the acoustic signal was beyond the scope of this study, the arrival time of the first prominent peak was selected for each sample (green dot; Fig. 4.13). It remains uncertain whether this peak in the signal compares to the arrival of the acoustic signal passing through the sample. Therefore, interpretation of absolute results obtained from these calculations should be approached with caution.

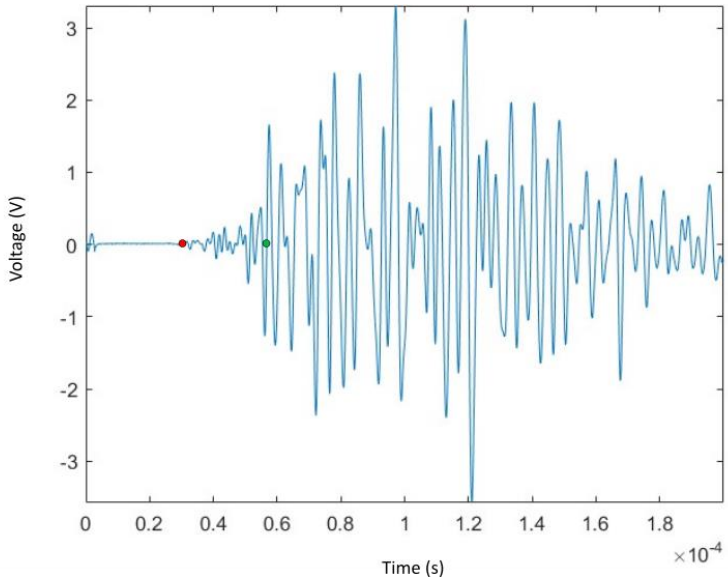

Fig. 4.13 Plotted acoustic signal through sample 4 after applying 15 MPa stress. The red dot indicates the selected arrival time, which results in high compressional wave velocities from signals through the aluminium casing. The green dot shows the first prominent peak of which the arrival time is selected to calculate the p-wave velocity, which could be from signal that only passed through the sample.

With the exception of sample 1 applying a total of 30 MPa pressure, the DT estimates of ~160-220 µs/ft (~1400-1900 m/s) fall within the range observed in sonic log data of the selected wells (Fig. 9.4 and Fig. 4.14). These values have a better fit with the compressional wave velocity range of 1600 m/s to 2400 m/s for sands up to 20 MPa measured by Zimmer (2004) and the acoustic velocity estimates below 5200 m/s in Carmichael (1989) compared to the previous calculated acoustic velocity values from the first arrival time of the acoustic signal (section 3.6). However, it is still not clear if the arrival time of the acoustic signal through the sample is selected. Further analysis and understanding of the structure of the acoustic signal are necessary to confirm this. With increasing depth, a decrease in compressional wave slowness is expected (section 1.5.4). Apart from sample 1 after applying 30 MPa pressure, all samples show a slight decrease in slowness with increasing depth of up to 15 µs/ft (Fig. 4.14). The experimentally derived acoustic velocity data are compared to other compressional velocity

data of sediments from the Upper North Sea Group in section 4.5.3. They should be interpreted with caution because it is uncertain whether the slowness values are representative of the sediment.

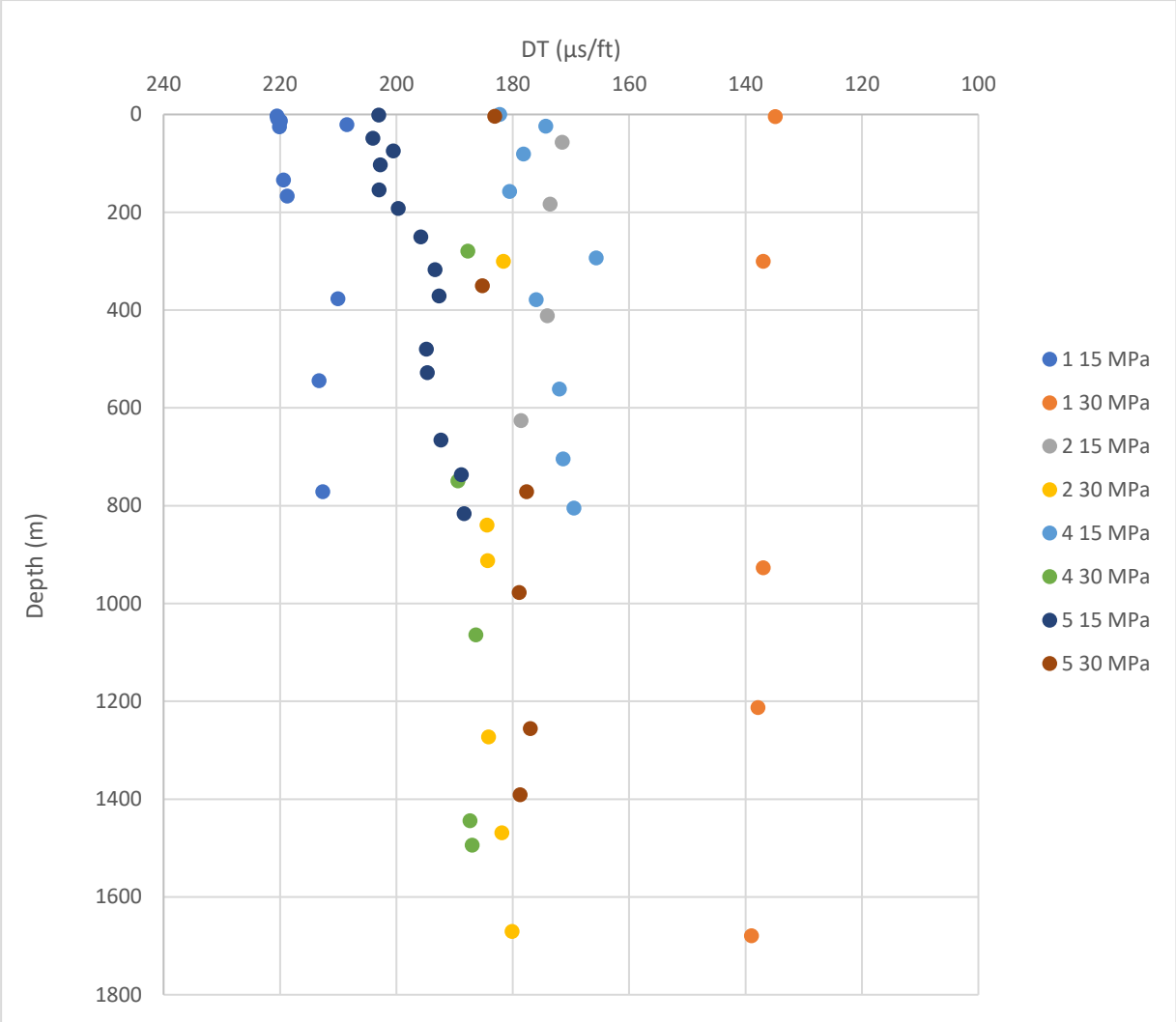

Fig. 4.14 Overview of the calculated DT (µs/ft) from the arrival time of the first prominent peak in the acoustic signals for samples 1, 2, 4, and 5 after 15 MPa pressure and after 30 MPa against the depth, based on a density of the overburden sediments of 1770 kg/m^3. Sample 1 after 30 MPa pressure differs from the other calculations. All samples show an increase in compressional slowness with depth, with exception of sample 1 after applying 30 MPa pressure.

4.5.3 Overview of compressional wave velocity data including experimentally derived estimates

The compressional wave velocity estimates based on the second picked arrival times for samples 1, 2, 4, and 5 (red dots; section 3.6) are plotted in an overview of velocity data from wells (Fig. 4.15). The interval velocity values lower than 1600 m/s were discarded in the overview of velocity data used in VELMOD-3.1. This could explain the relatively low compressional velocity estimates of sample 1, 2, 4, and 5 compared to the other estimates in the North Sea Group (yellow dots; Fig. 4.15). The dip of the calculated velocity data from the samples equals the smaller slope of the North Sea Group sediments when compared to the older Chalklime, Rhineland, Upper Jurassic, Altena, Triassic, Rotliegend and

Limburg groups, which all show a faster velocity increase with depth (Fig. 4.15). This shows the potential of using acoustic velocity data, when the arrival time is with certainty caused by the sample (section 4.5.2), to compare sonic velocity data from wells with experimental velocity data. With qualitative experimental data the method to calculate porosity from the sonic slowness could be improved, when comparing porosity and velocity data of experiments and calculations.

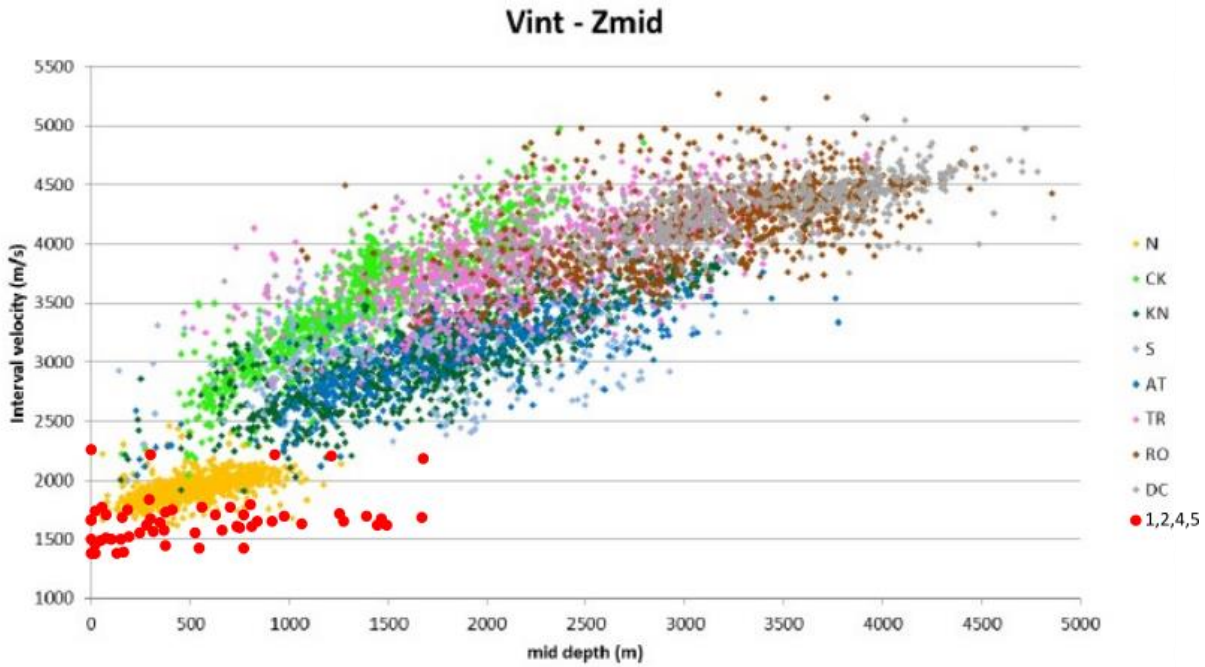

Fig. 4.15 Compressional wave velocity estimates calculated from acoustic data measured on samples 1, 2, 4, and 5 with increasing pressure up to 30 MPa, together with an overview of compressional wave velocity data for each main lithostratigraphic group from 1642 wells that were used for the development of VELMOD-3.1, a seismic velocity model on lithostratigraphic layers in the Netherlands (Fig. 1.13; (Doornenbal et al., 2022). In order of increasing age: N: North Sea Group, CK: Chalklime Group, KN: Rhineland Group, S: Upper Jurassic Group, AT: Altena Group, TR: Triassic Group, RO: Rotliegend Group, DC: Limburg Group. The dip of the calculated velocity data from samples 1, 2, 4, and 5 equals the slope of the North Sea Group velocity data. The increase of the sonic velocity with increasing depth is lower for the sediments of the North Sea Group compared to all other lithostratigraphic layers, displayed in this figure.

5. Conclusions

More porosity and permeability data are required to assess the full geothermal potential of reservoirs in the Upper North Sea Group. Porosity calculations using log data of selected wells and compaction experiments on sediments from the Breda Formation are promising methods to create new porosity estimates for the mid-depth range (100-1200 m), and to construct indicative porosity-depth relationships for sediments present within the Upper North Sea Group.

All porosity calculations based on log data show a negative trend towards lower porosity at larger depths, which is in line with expectations from different compaction models as outlined in Dasgupta and Mukherjee (2020). However, significant fluctuations show in the porosity estimates across the depth ranges of the wells. These are primarily driven by lithology variations in the heterogenous Breda, Oosterhout, and Maassluis Formations. The fluctuations can also be caused by uncertainty of this method to calculate porosity based on the sonic or the density log. Therefore, the quality of the calculation results should be indicated by calibrating the porosity estimates based on both the sonic and density log. The compaction factor used to calculate porosity from the sonic log introduces the largest uncertainty in porosity estimates. It is therefore recommended to correct this factor based on the best fit of sonic porosity estimates with porosity estimates calculated from density log data. This method seems insufficient to calculate accurate porosity in the upper 100 m of the subsurface, as porosity estimates calculated from log data result in large ranges within this shallow depth range. Corrected porosity estimates calculated from the sonic log for sands, interpreted from GR values, show the best fit with Athy's curve that is currently used for sands in the Upper North Sea group in the ThermoGIS geothermal potential calculations. However, the wide range of porosity estimates hinders conclusive support or adjustment of Athy's curve (Veldkamp, 2024). Improved lithology indication based on both the GR and lithology interpretations of nearby shallow wells, and improved quality control on the log data can reduce the uncertainty of the porosity calculations and increase the applicability to indicate porosity-depth relationships. Calculating porosity from a combination of log data is an excellent method to indicate porosity-depth relations for the Upper North Sea Group sediments in the mid-depth range. It should be used on future wells such as those of the SCAN project in which high-quality log data will be acquired.

The quality of the experimental porosity estimates is insufficient to indicate porosity-depth relations of sediments in the Upper North Sea Group. The lack of a significant decrease in the effective porosity data measured by a pycnometer after applying ~30 MPa is remarkable and does not compare to different compaction models as shown in Dasgupta and Mukherjee (2020). The total porosity change calculated from displacement data shows a change in porosity of -7% to -14%, which does not compare to the changes in measured and calculated effective porosity data of -0.9% to +3.1% and -14.7% to -71.3%, respectively. Uncertainties on the surface porosity of the samples used to calculate the total porosity from displacement complicate an absolute comparison with other measured and calculated porosity data. The sample loss during the experiment equals a total porosity loss when calculated from the displacement of up to 7%. This raises questions on the quality of the total porosity calculations. Sample handling throughout the experiment which could influence the porosity of the samples, and differences in porosity estimates from the Liessel core using the falling head method both add to the uncertainty of the experimentally derived porosity estimates. Because of differences between core description and laser particle size analysis lithology data, the lithology of the samples is uncertain. This uncertainty in lithology complicates the interpretation of the experimental porosity estimates.

Furthermore, the experimentally derived porosity estimates do not fit with Athy's curve that is currently used for sediments of the Upper North Sea Group. However, this curve of Athy is based on very limited data availability and includes large uncertainty. Therefore, the experimental results cannot be invalidated based on this poor fit with Athy's curve. The spatial resolution of the CT-scans is too low to indicate the porosity. No clear compressional wave velocity data could be obtained from acoustic velocity measurements due to the aluminium casing. The experimental results can therefore not yet be used to indicate porosity-depth relations. However, the experimental methods to gather porosity data demonstrate to be an efficient strategy to diminish the limited availability of porosity data for the mid-depth range. This study provides new insights into porosity experiments that in the near future may produce additional high quality porosity data for sediments of the Upper North Sea Group in the mid-depth range, and that can be used when resolving porosity-depth relationships.

Both the calculations of porosity from log data and experimental porosity estimates have the potential to contribute to the improvement of the currently used porosity-depth relation for sediments in the Upper North Sea Group in the mid-depth range. Heterogeneity in lithology of the Breda, Oosterhout, and Maassluis Formations complicates the establishment of one single applicable porosity-depth curve for the Upper North Sea Group. Further research into the lithological variation within the Upper North Sea group, log data quality, and experiments to compact unconsolidated sediment and measure porosity are required to improve the quality of compaction curves for unconsolidated sediments of the Upper North Sea Group for the mid-depth range.

6. Recommendations

Improvements on the method to calculate porosity and on the compaction experiment could decrease the uncertainty in porosity estimates and add qualitative data to the limited availability of porosity data of sediments in the Upper North Sea Group for the mid-depth range.

Because lithology significantly influences porosity estimates, it is essential to specify the range of lithologies for which the porosity-depth relationship is indicated. The classification in lithology groups for porosity calculations based on log data relies solely on the gamma ray log (section 4.2.4). The lithology classification based on gamma ray values can be improved by further analysis of the relation between gamma ray values and the lithology. Furthermore, these lithology estimates based on gamma ray log data can be compared to the interpreted lithology of selected shallow wells positioned close to the selected deep wells. This approach facilitates lithology interpretation over matching depth intervals between the wells and enables clearer identification of lithology ranges, for which the porosity-depth relation can be calculated.

For samples used in compaction experiments it is recommended to gather laser particle size analysis data to interpret lithology. Furthermore, grain sorting can be required from laser particle size analysis data. In combination with data on grain sphericity these could give more insight in the grain packing of different samples and add to interpretations on differences in compaction processes. Low uncertainty in the lithology of the samples allows for quality control of the porosity measurements with increasing depth (section 4.2.3).

In this study several wells that were initially selected for porosity calculation were not used to calculate porosity, because of the poor data quality (sections 2.1.2 and 3.1.3). This quality control was based on the appearance of the log data without indicating (the lack of) conversion of the data. Variations in the appearance of log data could for example be caused using different logging tool types, the eccentricity of these tools, and variations in borehole size, when no uniform corrections are applied. It is worthwhile to further assess the well information from drilling reports and attachments of the log data to evaluate the corrections and quality of the data. Considerable time was spent on extracting this data manually from scanned drilling reports. It is useful to store important well information in a consistent way in a well database. Log data that was considered not useful in this study, may well be useful in porosity calculation after correction for particularities described in the drilling report. This approach would reduce the data scarcity for sediments of the Upper North Sea Group in the mid-depth range.

The compaction factor, required for calculation of the porosity from the sonic log, should be corrected based on the fit between porosity estimates calculated from the sonic log and the density log. Furthermore, it is recommended to test the quality of the porosity estimates calculated from log data by comparing porosity estimates based on at least two log data types (sections 3.1.2 and 4.1.3). A database on determined compaction factors would help future porosity determinations. Moreover, calculation of porosity based on log data should not be performed on sediments in the upper 100 m of the subsurface, as this results in high ranges of porosity estimates.

The sample loss during the experiment is the main problem in estimating the porosity of the unconsolidated sediments (section 4.2.2). Using nettings/sieve meshes featuring smaller pores than 82x82 µm will decrease the loss of small particles from the aluminium casing during saturation and compression of the samples (sections 2.2.4 and 2.2.6). Furthermore, there are setups to perform in

situ CT-scans when pressurizing the sample, in which it is not necessary to remove the sample from the uni-axial stress-strain device to the CT-scanner. Such a procedure will also reduce the fraction of the sample that is lost throughout the experiment. CT-scans should be performed with higher spatial resolution to improve the accuracy of porosity determination using Dragonfly (section 3.4).

The aluminium casing should preferably be replaced with a material that is strong enough to (i) maintain its shape under 30 MPa pressure and (ii) has a lower acoustic velocity than the sample (section 4.5.1). These modifications would enable to calculate the precise compressional wave velocities from the sample and compare those with the sonic log data of the wells. The correction for and effect of the aluminium casing, while measuring the matrix volume in a pycnometer, should be further investigated (section 4.2.1).

The number of samples for the compaction experiments was very limited to allow for a good comparison between the results of the samples and the porosity calculations, as well as for indication of porosity-depth relations. It is therefore, recommended to increase the sample size in future compaction experiments. It could also be interesting to measure effective porosity using a pycnometer at more pressure steps during compaction to increase the number of porosity data points and create a more accurate and validated fit with Athy's curve. However, chances on sample loss will be higher, because the sample then needs to be transported multiple times between the pycnometer and the uni-axial stress-strain device. Furthermore, measuring porosity of samples during compaction experiments using the falling head method could be interesting to better indicate the data quality. However, these total porosity estimates could not be directly compared to effective porosity estimates measured by a pycnometer. It could therefore be interesting to further explore the relation between total and effective porosity for different lithologies as total porosity estimates then possibly can be better combined with effective porosity in indicating porosity-depth relations.

Finally, it is recommended to calculate porosity on newly derived log data from recently drilled wells in the mid-depth range and continue with the development of compaction experiments. This will reduce the lack of porosity data and improve the knowledge of porosity-depth relations of sediments in the Upper North Sea Group, thereby enhancing the ability to estimate the geothermal potential of reservoirs positioned at these shallow depths.

7. Acknowledgements

Part of the work during this project was conducted under the WarmingUP Geothermal and Storage Upscaling (WarmingUPGOO) project. This was made possible by a subsidy from the Netherlands Enterprise Agency - Rijksdienst voor Ondernemend Nederland (RVO) as part of the Mission-driven Research, Development, and Innovation subsidy scheme - Missie-gedreven Onderzoek, Ontwikkeling en Innovatie (MOOI) -, known by RVO under project number MOOI322012. WarmingUPGOO fulfils MOOI mission B Built Environment and supports the innovation theme of Sustainable collective heat supply. This project also benefitted from EPOS-NL Facility Access to TU Delft, supported by the Dutch Research Council (NWO). I would like to thank my research mentors Hans Veldkamp and Lies Peters (TNO; Utrecht; The Netherlands) for all the feedback, their guidance throughout this project and for warmly welcoming me to TNO. I enjoyed my internship at TNO and had fun with the other TNO interns and colleagues, whose expertise and support I benefited from throughout my project. Big thanks to them! Furthermore, I would like to give credit to Auke Barnhoorn (assoc. Prof.), Marc Friebel, Karel Heller, Ellen Meijvogel-de Koning, Entale Kane, and Milad Naderloo from the Technical University of Delft (TU Delft; The Netherlands), for their support in setting up the compaction experiment, introducing me to the Laboratory of Geoscience and Engineering at TU Delft, and helping me out with data processing. It was very educational to use the facilities in the lab and I am happy that I could perform the experiment myself with guidance of the technical staff. I would like to express my gratitude to my VU Amsterdam Supervisor John Reijmer (emeritus Prof.) for providing me with feedback to improve my Master Thesis and scientific writing. Furthermore, I would like to thank my second assessor Bernd Andeweg and Jeroen van der Lubbe (asst. Prof.) for evaluating my Master Thesis. Finally, I would like to thank my parents, Mees, Loes, and friends for believing in me, supporting me through the ups and downs of the project, and for their encouragement during my Thesis presentation.

8. References

Agemar, T., Weber, J., & Schulz, R. (2014). Deep Geothermal Energy Production in Germany. *Energies*, *7*, 4397-4416. https://doi.org/10.3390/en7074397

Ahmed, A. A., Assadi, M., Kalantar, A., Sliwa, T., & Sapińska-Śliwa, A. (2022). A Critical Review on the Use of Shallow Geothermal Energy Systems for Heating and Cooling Purposes. *Energies*, *15*(12). https://doi.org/10.3390/en15124281

Akinsete, O., & Adekoya, D. (2016). *Effects of Mud Filtrate Invasion on Well Log Measurements* SPE Nigeria Annual International Conference and Exhibition, Lagos, Nigeria.

Al-Khoury, R. (2011). *Computational modeling of shallow geothermal systems*. CRC press. https://doi.org/10.1201/b11462

Al-Ruwaili, S. B., & Al-Waheed, H. H. (2004). *Improved Petrophysical Methods and Techniques for Shaly Sands Evaluation* SPE Annual Technical Conference and Exhibition, https://doi.org/10.2118/89735-MS

Alberts, L. J. H. (2005). *Initial porosity of random packing: computer simulation of grain rearrangement* http://resolver.tudelft.nl/uuid:fa3b8d33-3eda-474a-bebd-87f43dd58873

Athy, L. F. (1930). Compaction and Oil Migration. *AAPG Bulletin*, *14*(1), 25-35. https://doi.org/10.1306/3D93289F-16B1-11D7-8645000102C1865D

Baldwin, B., & Butler, C. (1985). Compaction curves. *AAPG Bulletin*, *69*, 622-626. https://doi.org/10.1306/AD462547-16F7-11D7-8645000102C1865D

Barbier, E. (2002). Geothermal energy technology and current status: an overview. *Renewable and Sustainable Energy Reviews*, *6*(1), 3-65. https://doi.org/10.1016/S1364-0321(02)00002-3

Békési, E., Struijk, M., Bonté, D., Veldkamp, H., Limberger, J., Fokker, P. A., Vrijlandt, M., & van Wees, J.-D. (2020). An updated geothermal model of the Dutch subsurface based on inversion of temperature data. *Geothermics*, *88*, 101880. https://doi.org/10.1016/j.geothermics.2020.101880

Bernabé, Y., Mok, U., & Evans, B. (2003). Permeability-porosity Relationships in Rocks Subjected to Various Evolution Processes. *Pure and Applied Geophysics*, *160*(5), 937-960. https://doi.org/10.1007/PL00012574

Bjørlykke, K. (2003). Compaction (consolidation) of sediments. In G. V. Middleton, M. J. Church, M. Coniglio, L. A. Hardie, & F. J. Longstaffe (Eds.), *Encyclopedia of Sediments and Sedimentary Rocks* (pp. 161-168). Springer Netherlands. https://doi.org/10.1007/978-1-4020-3609-5_53

Bond, L. J., Denslow, K. M., Griffin, J. W., Dale, G. E., Harris, R. V., Moran, T. L., Sheen, D. M., & Schenkel, T. (2010). *Evaluation of non-nuclear techniques for well logging: Technology evaluation*. https://www.pnnl.gov/main/publications/external/technical_reports/pnnl-20831.pdf

Buik, N., & Bakema, G. (2019). *Geothermie putten in ondiepe fijnzandige formaties* (65163/RDx/20191218). https://www.kasalsenergiebron.nl/content/user_upload/Geothermie_Putten_in_ondiepe_fijnzandige_formaties_def_2.pdf

Buma, J., Bus, T., Harting, S. A. R., & Zaadnoordijk, W. J. (2021). *Karakterisering van de doorlatendheid van de ondiepe ondergrond van Noord-Nederland. TNO report R10310*. https://www.grondwatertools.nl/sites/default/files/2021-08/TNO-GDN2021_KarakteriseringDoorlatendheidOndiepeOndergrondNoord-Nederland_TNO-R10310.pdf

Byrnes, A. P. (1994). *Empirical Methods of Reservoir Quality Prediction* (Vol. 30). SEPM Society for Sedimentary Geology. https://doi.org/10.2110/scn.94.30.0009

Carbó, R., & Molero, A. C. (2000). The effect of temperature on sound wave absorption in a sediment layer. *The Journal of the Acoustical Society of America*, *108*(4), 1545-1547. https://doi.org/10.1121/1.1289360

Carmichael, R. S. (1989). *Practical Handbook of Physical Properties of Rocks and Minerals*. CRC Press. https://doi.org/10.1201/9780203710968

Chakraborty, S., Yadav, A., & Chatterjee, R. (2021). Comprehensive Rock Physics, Petrophysics workflow to correct Sonic Logs for improved seismic QI: Study using wells of Krishna Godavari basin. *Journal of Applied Geophysics*, *192*, 104394. https://doi.org/10.1016/j.jappgeo.2021.104394

Chuhan, F. A., Kjeldstad, A., Bjørlykke, K., & Høeg, K. (2002). Porosity loss in sand by grain crushing—experimental evidence and relevance to reservoir quality. *Marine and Petroleum Geology*, *19*(1), 39-53. https://doi.org/10.1016/S0264-8172(01)00049-6

Darcy, H. (1856). *Les fontaines publiques de la ville de Dijon: exposition et application des principes à suivre et des formules à employer dans les questions de distribution d'eau* (Vol. 1). Victor dalmont. https://search.worldcat.org/title/fontaines-publiques-de-la-ville-de-dijon-exposition-et-application-des-principes-a-suivre-et-des-formules-a-employer-dans-les-questions-de-distribution-deau/oclc/421873273

Das, G. K. (2016). Sediment Grain Size. In M. J. Kennish (Ed.), *Encyclopedia of Estuaries* (pp. 555-558). Springer Netherlands. https://doi.org/10.1007/978-94-017-8801-4_148

Dasgupta, T., & Mukherjee, S. (2020). *Sediment Compaction and Applications in Petroleum Geoscience*. https://doi.org/10.1007/978-3-030-13442-6

Díaz, E., Prasad, M., Mavko, G., & Dvorkin, J. (2003). Effect of glauconite on the elastic properties, porosity, and permeability of reservoir rocks. *The Leading Edge*, *22*, 42-45. https://doi.org/10.1190/1.1542755

Dickinson, G. (1953). Geological Aspects of Abnormal Reservoir Pressures in Gulf Coast Louisiana. *AAPG Bulletin*, *37*(2), 410-432. https://doi.org/10.1306/5CEADC6B-16BB-11D7-8645000102C1865D

Domenico, S. N. (1977). Elastic properties of unconsolidated reservoirs. *GEOPHYSICS*, *42*(7), 1339-1368. https://doi.org/10.1190/1.1440797

Doornenbal, J. C., Middelburg, H., de Haan, H., & Botz, M. (2022). *VELMOD-4* (TNO 2020 R10558). https://www.nlog.nl/sites/default/files/2022-03/r10558_velmod-4_nam_final_public_report.pdf

Drijver, B., Bakema, G., & Oerlemans, P. (2019). *State of the art of HT-ATES in The Netherlands* European Geothermal Congress 2019, Den Haag, The Netherlands. https://europeangeothermalcongress.eu/wp-content/uploads/2019/07/289.pdf

Dzevanshir, R. D., Buryakovskiy, L. A., & Chilingarian, G. V. (1986). Simple quantitative evaluation of porosity of argillaceous sediments at various depths of burial. *Sedimentary Geology*, *46*(3), 169-175. https://doi.org/10.1016/0037-0738(86)90057-6

EBN, TNO, & EZK. (2024). *SCAN*. https://scanaardwarmte.nl/

Essen, H. v. (2022). *Achtergrond doorlatendheidsmetingen* (11207257-002-GEO-0004).

Falvey, D. A., & Deighton, I. (1982). Recent advances in burial and thermal geohistory analysis. *The APPEA Journal*, *22*(1), 65-81. https://doi.org/https://doi.org/10.1071/AJ81004

Foster, E. (2007). *Well Log Interpretation*. PetroSkills. www.petroskills.com

Foster, J. B. (1966). Estimation of Formation Pressures From Electrical Surveys-Offshore Louisiana. *Journal of Petroleum Technology*, *18*(02), 165-171. https://doi.org/10.2118/1200-PA

Galloway, W. E. (1974). Deposition and Diagenetic Alteration of Sandstone in Northeast Pacific Arc-Related Basins: Implications for Graywacke Genesis. *GSA Bulletin*, *85*(3), 379-390. https://doi.org/10.1130/0016-7606(1974)85

Geel, C. (1999). *Interpretation of Petrophysical Data*.

Geel, K., & Foeken, J. (2021). *Formation Evaluation of the Brussels Sand Member in the Netherlands*. https://www.warmingup.info/documenten/final-report-formation-evaluation-brussels-sand-2021-12-01.pdf

Gibb, J. P., Barcelona, M. J., Ritchey, J. D., & LeFaivre, M. H. (1984). *Effective Porosity of Geologic Materials: First Annual Report*. http://hdl.handle.net/2142/73188

Gil, G., Schneider, E. A. G., Moreno, M. M., & Cerezal, J. C. S. (2022). *Shallow Geothermal Energy*. Springer. https://doi.org/10.1007/978-3-030-92258-0

Giles, M. R. (1997). *Diagenesis: A quantitative perspective: Implications for basin modelling and rock property prediction* (1 ed.). Springer. https://link.springer.com/book/9780792348146

Guy, N., Colombo, D., Frey, J., Cornu, T., & Cacas-Stentz, M. C. (2019). Coupled Modeling of Sedimentary Basin and Geomechanics: A Modified Drucker–Prager Cap Model to Describe Rock Compaction in Tectonic Context. *Rock Mechanics and Rock Engineering*, *52*(10), 3627-3643. https://doi.org/10.1007/s00603-019-01783-y

Ham, H. (1966). New charts help estimate formation pressures. *Oil Gas J*, *64*(51), 58-63.

Hantschel, T., & Kauerauf, A. I. (2009). *Fundamentals of basin and petroleum systems modeling*. Springer Science & Business Media. https://doi.org/10.1007/978-3-540-72318-9

Hartog, N., Griffioen, J., & van Bergen, P. F. (2005). Depositional and paleohydrogeological controls on the distribution of organic matter and other reactive reductants in aquifer sediments. *Chemical Geology*, *216*(1), 113-131. https://doi.org/10.1016/j.chemgeo.2004.11.006

He, W., Hajash, A., & Sparks, D. (2007). Evolution of fluid chemistry in quartz compaction systems: Experimental investigations and numerical modeling. *Geochimica et Cosmochimica Acta*, *71*(20), 4846-4855. https://doi.org/10.1016/j.gca.2007.08.013

Hedberg, H. D. (1936). Gravitational compaction of clays and shales. *American Journal of Science*, 241-287. https://doi.org/10.2475/AJS.S5-31.184.241

Hicks, W. G., & Berry, J. E. (1956). Application of continuous velocity logs to determination of fluid saturation of reservoir rocks. *GEOPHYSICS*, *21*(3), 739-754. https://doi.org/10.1190/1.1438267

Hosoi, H. (1963). First migration of petroleum in Akita and Yamagata Prefecture (II). *The Journal of the Japanese Association of Mineralogists,Petrologists and Economic Geologists*, *49*, 101-114. https://doi.org/10.2465/GANKO1941.49.101

Hossain, Z., Mukerji, T., & Fabricius, I. L. (2012). Vp-Vs relationship and amplitude variation with offset modelling of glauconitic greensand. *Geophysical Prospecting*, *60*(1), 117-137. https://doi.org/https://doi.org/10.1111/j.1365-2478.2011.00968.x

Hummelman, J., Maljers, D., Menkovic, A., Reindersma, R., Vernes, R., & Stafleu, J. (2019). *Totstandkomingsrapport hydrogeologisch model (REGIS II)*. https://www.broloket.nl/sites/default/files/Totstandkomingsrapport-REGIS-II.pdf

Jansen, H. S. M., Huizer, J., Dijkmans, J. W. A., Mesdag, C., & van Hinte, J. E. (2004). The geometry and stratigraphic position of the Maassluis Formation (western Netherlands and southeastern North Sea). *Netherlands Journal of Geosciences*, *83*(2), 93-99. https://doi.org/10.1017/S0016774600020060

Kiden, P. (2019). *Kwaliteitstoetsingsdocument Hydrogeologisch model REGIS II v2.2* (TNO 2019 R11932). https://www.dinoloket.nl/regis-ii-het-hydrogeologische-model

Lako, P., Luxembourg, S., Ruiter, A., & Groen, B. i. t. (2011). *Geothermische energie en de SDE: Inventarisatie van de kosten van geothermische energie bij opname in de SDE* (ECN-E--11-022). https://publicaties.ecn.nl/PdfFetch.aspx?nr=ECN-E--11-022

Loucks, R., Dodge, M., & Galloway, W. E. (1979). *Sandstone consolidation analysis to delineate areas of high-quality reservoirs suitable for production of geopressured geothermal energy along the Texas Gulf Coast*. https://doi.org/10.2172/5754234

Lyons, W. C. (2010). Formation Evaluation. In W. C. Lyons (Ed.), *Working Guide to Reservoir Engineering* (pp. 97-232). Gulf Professional Publishing. https://doi.org/10.1016/B978-1-85617-824-2.00002-2

Magara, K. (1968). Compaction and Migration of Fluids in Miocene Mudstone, Nagaoka Plain, Japan. *AAPG Bulletin*, *52*(12), 2466-2501. https://doi.org/10.1306/5D25C58D-16C1-11D7-8645000102C1865D

Meade, R. H. (1966). Factors influencing the early stages of the compaction of clays and sands; review. *Journal of Sedimentary Research*, *36*(4), 1085-1101. https://doi.org/10.1306/74D71604-2B21-11D7-8648000102C1865D

Meegoda, N. J., & Gunasekera, S. D. (1992). A new method to measure the effective porosity of clays. *Geotechnical Testing Journal*, *15*, 340-340. https://doi.org/10.1520/GTJ10248J

Mijnlieff, H., Obdam, A., Van Wees, J., Pluymaekers, M., & Veldkamp, J. (2014). *DoubletCalc 1.4 manual* (TNO 2014 R11396). (English version for DoubletCalc, Issue. https://www.nlog.nl/sites/default/files/6ab98fc3-1ca1-4bbe-b0a2-c5a9658a3597_doubletcalc%20v143%20manual.pdf

Munsterman, D. K., ten Veen, J. H., Menkovic, A., Deckers, J., Witmans, N., Verhaegen, J., Kerstholt-Boegehold, S. J., van de Ven, T., & Busschers, F. S. (2019). An updated and revised stratigraphic framework for the Miocene and earliest Pliocene strata of the Roer Valley Graben and adjacent blocks. *Netherlands Journal of Geosciences*, *98*. https://doi.org/10.1017/njg.2019.10

Olowokere, M. (2011). Porosity and Lithology Prediction in Eve Field, Niger Delta Using Compaction Curves and Rock Physics Models. *International Journal of Geosciences*, *2*, 366-372. https://doi.org/10.4236/ijg.2011.23039

Pittman, E. D., & Larese, R. E. (1991). Compaction of Lithic Sands: Experimental Results and Applications1. *AAPG Bulletin*, *75*(8), 1279-1299. https://doi.org/10.1306/0C9B292F-1710-11D7-8645000102C1865D

Proshlyakov, B. (1960). *Reservoir properties of rocks as a function of their depth and lithology*. Associated Technical Services. https://www.researchgate.net/publication/291752598_Reservoir_properties_of_rocks_as_a_function_of_their_depth_and_lithology

Revil, A., Grauls, D., & Brévart, O. (2002). Mechanical compaction of sand/clay mixtures. *Journal of Geophysical Research: Solid Earth*, *107*. https://doi.org/10.1029/2001JB000318

Rider, M. H. (2002). *The geological interpretation of well logs* (2 ed.). Rider-French Consulting Limited. https://search.worldcat.org/title/geological-interpretation-of-well-logs/oclc/51638049

RVO, R. v. O. N.-. (2017). *Wat is bodemenergie en aardwarmte?* https://www.rvo.nl/onderwerpen/bodemenergie-aardwarmte/wat-het

Saul, M. J., & Lumley, D. E. (2013). A new velocity–pressure–compaction model for uncemented sediments. *Geophysical Journal International*, *193*(2), 905-913. https://doi.org/10.1093/gji/ggt005

Scherer, M. (1987). Parameters Influencing Porosity in Sandstones: A Model for Sandstone Porosity Prediction: ERRATUM. *AAPG Bulletin*, *71*. https://doi.org/10.1306/703C80FB-1707-11D7-8645000102C1865D

Schneider, F., Burrus, J., & Wolf, S. (1993). Modelling overpressures by effective-stress / porosity relationships in low-permeability rocks: Empirical artifice or physical reality. *Norwegian Petroleum Society Special Publications*, *3*. https://www.researchgate.net/publication/325961682_Modelling_overpressures_by_effective-stress_porosity_relationships_in_low-permeability_rocks_Empirical_artifice_or_physical_reality

Schneider, F., Potdevin, J.-L., Wolf, S., & Faille, I. (1994). Modèle de compaction élastoplastique et viscoplastique pour simulateur de bassins sédimentaires. *Oil & Gas Science and Technology-revue De L Institut Francais Du Petrole*, *49*, 141-148. https://doi.org/10.2516/ogst:1994007

Schneider, F., Potdevin, J. L., Wolf, S., & Faille, I. (1996). Mechanical and chemical compaction model for sedimentary basin simulators. *Tectonophysics*, *263*(1), 307-317. https://doi.org/10.1016/S0040-1951(96)00027-3

Sclater, J. G., & Christie, P. A. F. (1980). Continental stretching: An explanation of the Post-Mid-Cretaceous subsidence of the central North Sea Basin. *Journal of Geophysical Research: Solid Earth*, *85*(B7), 3711-3739. https://doi.org/https://doi.org/10.1029/JB085iB07p03711

Serra, O. (1983). *Fundamentals of well-log interpretation*. Elsevier. https://faculty.ksu.edu.sa/sites/default/files/Fundamentals%20of%20Well-Log%20Interpretation%20-%20The%20Acquisition%20of%20Logging%20Data_0.pdf

Simmelink, H. J., Underschultz, J., Verweij, J. M., & Witmans, N. (2012). Pressure and fluid dynamic characterisation of the Dutch subsurface. *Netherlands Journal of Geosciences - Geologie en Mijnbouw*, *91*(4), 465-490. https://doi.org/10.1017/S0016774600000342

Smit, F. (2022). *An overlooked aquifer in the Netherlands: geothermal potential of the Breda Formation in the Zuiderzee Low* [Master thesis, https://repository.tudelft.nl/islandora/object/uuid%3A416ab31c-99e0-4119-9b1e-c8143f9a4eb3

Smith, J. E. (1971). The dynamics of shale compaction and evolution of pore-fluid pressures. *Journal of the International Association for Mathematical Geology*, *3*(3), 239-263. https://doi.org/10.1007/BF02045794

Sørensen, M. K. (2015). *Mud-filtrate correction of sonic logs by fluid substitution* [Ph.D. Thesis]. https://backend.orbit.dtu.dk/ws/portalfiles/portal/131381314/Thesis.pdf

Terzaghi, K. (1925). *Erdbaumechanik auf bodenphysikalischer grundlage*. F. Deuticke. https://search.worldcat.org/title/erdbaumechanik-auf-bodenphysikalischer-grundlage/oclc/2710377

TNO. (2023a). *Data en informatie van de Nederlandse Ondergrond*. https://www.dinoloket.nl/ondergrondgegevens

TNO. (2023b). *Nederlandse Olie- en Gasportaal*. https://www.nlog.nl/datacenter/brh-overview

TNO. (2024). *ThermoGIS*. https://www.thermogis.nl/mapviewer

Tsagarakis, K. P., Efthymiou, L., Michopoulos, A., Mavragani, A., Anđelković, A. S., Antolini, F., Bacic, M., Bajare, D., Baralis, M., Bogusz, W., Burlon, S., Figueira, J., Genç, M. S., Javed, S., Jurelionis, A., Koca, K., Ryżyński, G., Urchueguia, J. F., & Žlender, B. (2020). A review of the legal framework in shallow geothermal energy in selected European countries: Need for guidelines. *Renewable Energy*, *147*, 2556-2571. https://doi.org/10.1016/j.renene.2018.10.007

Vardon, P., Abels, H. A., Barnhoorn, A., B., S., D., A.-C., D., G., L., & Vargas Meleza, L. (2023). *Geothermal Project on TU Delft Campus - DAPGEO-02 Initial Borehole Dataset* Version 2). https://doi.org/doi.org/10.4121/20299644.v2

Vardon, P. J., Laumann, S. J., Schmiedel, T., Vargas Meleza, L., Barnhoorn, A., Abels, H. A., Drijkoningen, G. G., Dieudonné, A. A. M., Beernink, S. T. W., & van den Berg, J. J. (2022). *Drilling report* [Report]. Delft University of Technology. https://doi.org/10.4233/uuid:fde70c00-cf65-4174-9cd3-89585a5e61bd

Veldkamp, H. (2024). *ThermoGIS data [unpublished]*. TNO. https://www.thermogis.nl/

Veldkamp, H., Dinkelman, D., Kleinlugtenbelt, R., Drijver, B., Schlief, D., Sesink, J., & Jansen, F. (2021). *Hoge temperatuuropslag NEXTgarden*.

Veldkamp, J., Geel, C., & Peters, E. (2022). *Characterization of aquifer properties of the Brussels Sand Member from cuttings* (060.43190/01.01.01). https://www.warmingup.info/documenten/brussel-sand-psd-fnal-report_20220907.pdf

Vernes, R. W., Deckers, J., Walstra, J., Kruisselbrink, A. F., Menkovic, A., Bogemans, F., De Ceukelaire, M., Dirix, K., Dusar, M., Hummelman, H. J., Maes, R., Meyvis, B., Munsterman, D. K., Reindersma, R., Rombaut, B., Van Baelen, K., Van den Ven, T. J. M., Van Haren, T., & Welkenhuysen, K. (2023). *Geologisch en hydrogeologisch 3D model van het Cenozoïcum van de Belgisch-Nederlandse grensstreek van De Noorderkempen/West-Brabant (H3O – De Voorkempen).* https://www.vlaanderen.be/publicaties/geologisch-en-hydrogeologisch-3d-model-van-het-cenozoicum-van-de-belgisch-nederlandse-grensstreek-van-de-noorderkempen-west-brabant

Wang, S. W., Zhu, W., Qian, X., Xu, H., & Fan, X. (2016). Study of threshold gradient for compacted clays based on effective aperture. *Environmental Earth Sciences*, *75*. https://doi.org/10.1007/s12665-016-5502-z

Weller, J. M. (1959). Compaction of Sediments1. *AAPG Bulletin*, *43*(2), 273-310. https://doi.org/10.1306/0BDA5C9F-16BD-11D7-8645000102C1865D

Woessner, W. W., & Poeter, E. P. (2020). *Hydrogeologic Properties of Earth Materials and Principles of Groundwater Flow*. The Groundwater Project. https://gw-project.org/books/hydrogeologic-properties-of-earth-materials-and-principles-of-groundwater-flow/

Wyllie, M. R. J., Gregory, A. R., & Gardner, L. W. (1956). Elastic wave velocities in heterogeneous and porous media. *GEOPHYSICS*, *21*(1), 41-70. https://doi.org/10.1190/1.1438217

Zhang, J., Wong, T.-F., & Davis, D. M. (1990). Micromechanics of pressure-induced grain crushing in porous rocks. *Journal of Geophysical Research: Solid Earth*, *95*(B1), 341-352. https://doi.org/https://doi.org/10.1029/JB095iB01p00341

Zimmer, M. (2004). *Seismic velocities in unconsolidated sands: Measurements of pressure, sorting, and compaction effects* [PhD Thesis, Stanford University]. https://pangea.stanford.edu/research/srb/docs/theses/SRB_95_NOV03_Zimmer.pdf

9. Appendix

9.1 Figures

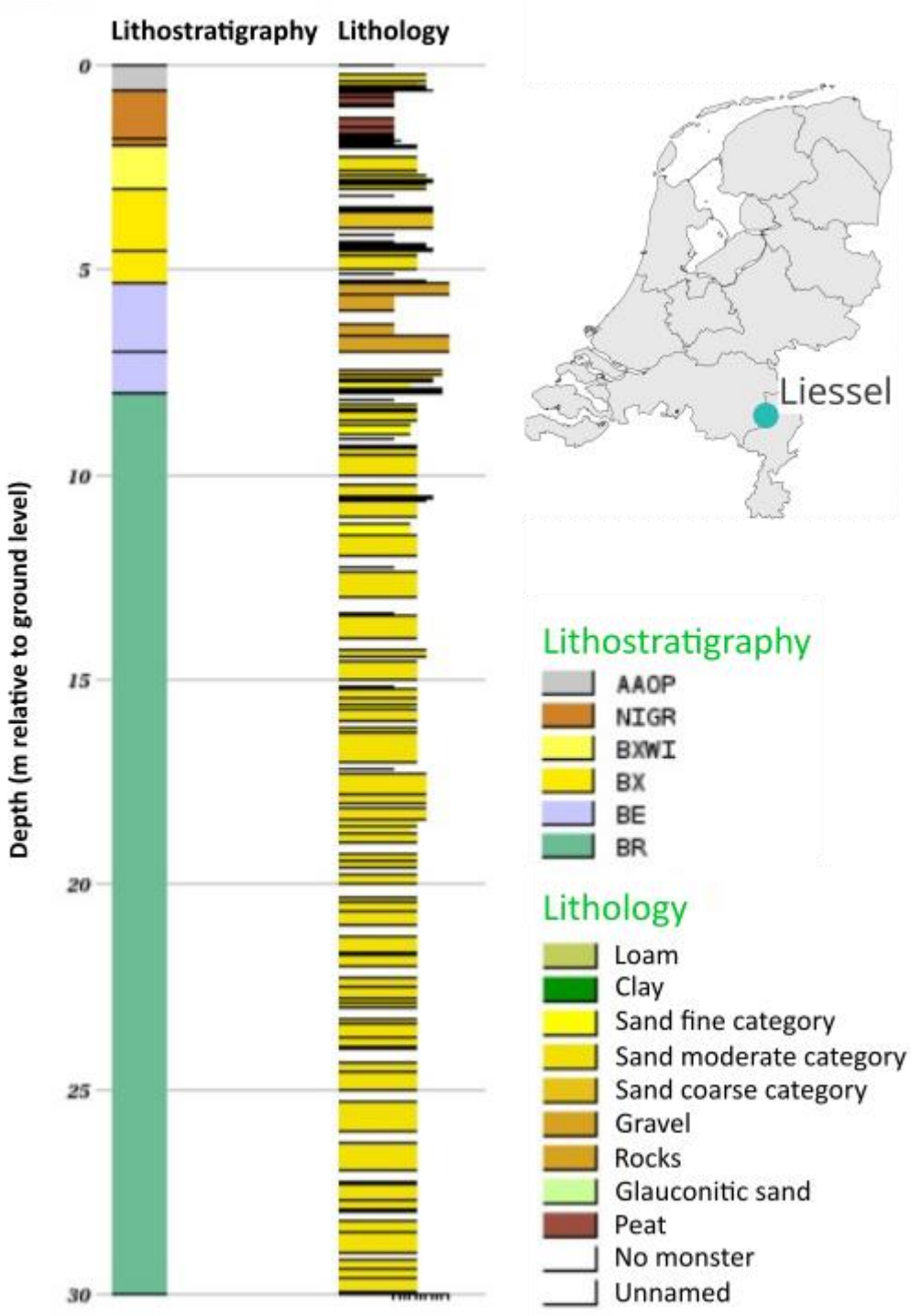

Fig. 9.1 Location, lithostratigraphy and lithology of the Liessel core, B52C2133. Lithostratigraphy: BR: Breda Fm, BE: Beegden Fm, BX: Boxtel Fm, BXWI: Boxtel Fm, Wierden deposit, NIGR: Nieuwkoop Fm, Griendsveen deposit, AAOP: anthropogenic ground (TNO, 2023a).

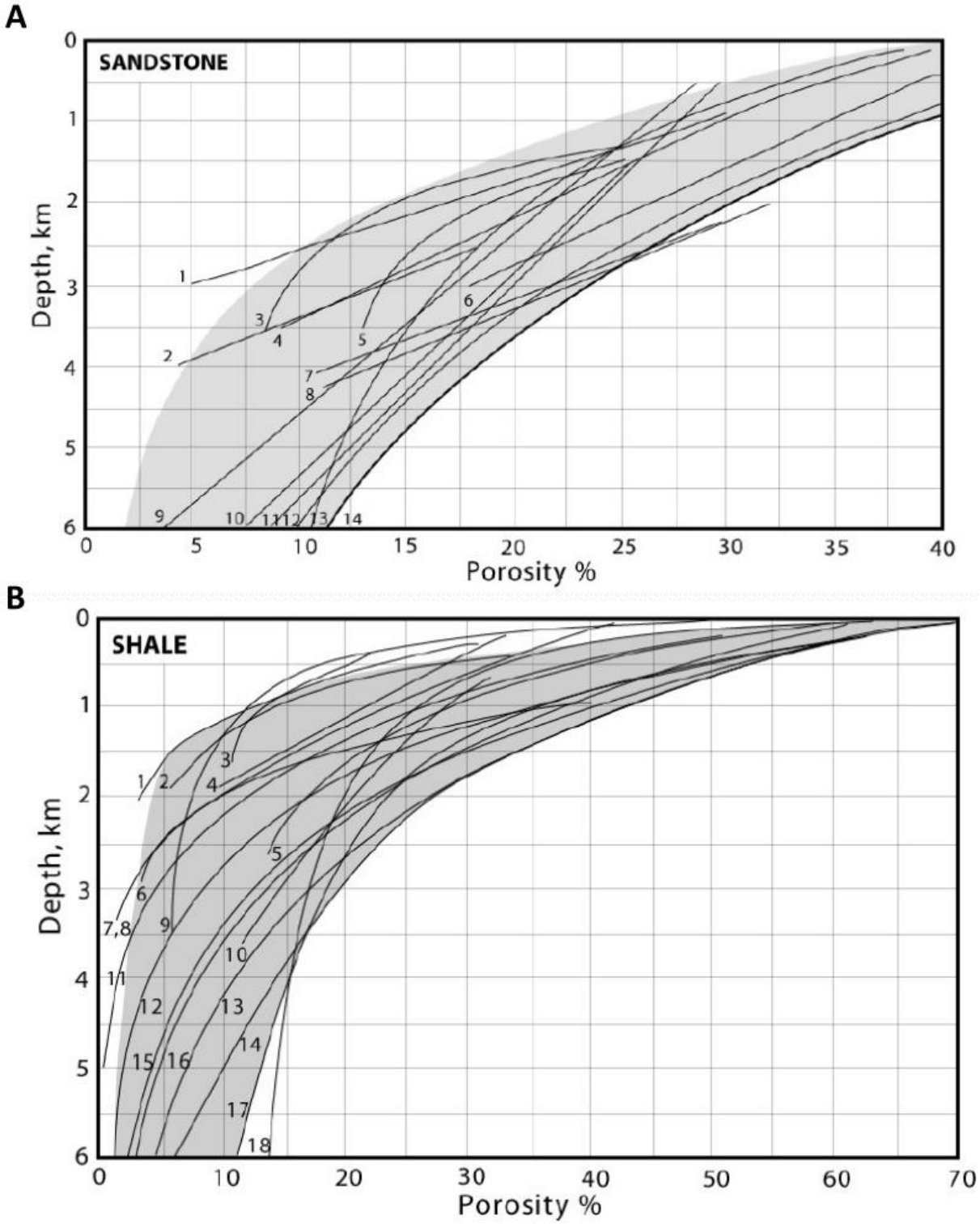

Fig. 9.2 A. Porosity-depth relations for sandstones; 1, 6: (Galloway, 1974); 2, 3, 5, 7, 8: (Giles, 1997); 9: (Loucks, Dodge, & Galloway, 1979); 10, 12: (Scherer, 1987); 11: (Baldwin & Butler, 1985) ; 13: (Sclater & Christie, 1980); 14: (Falvey & Deighton, 1982). B. Porosity-depth relations for shales; 1: (Athy, 1930), 2: (Hosoi, 1963); 3: (Meade, 1966); 4: (Hedberg, 1936); 5: (Magara, 1968); 6: (Weller, 1959); 7, 8, 11, 14: (Giles, 1997); 9: (Proshlyakov, 1960); 10: (Foster, 1966); 12, 16: (Dzevanshir, Buryakovskiy, & Chilingarian, 1986); 13: (Ham, 1966); 15: (Sclater & Christie, 1980); 17: (Falvey & Deighton, 1982); 18: (Dickinson, 1953).

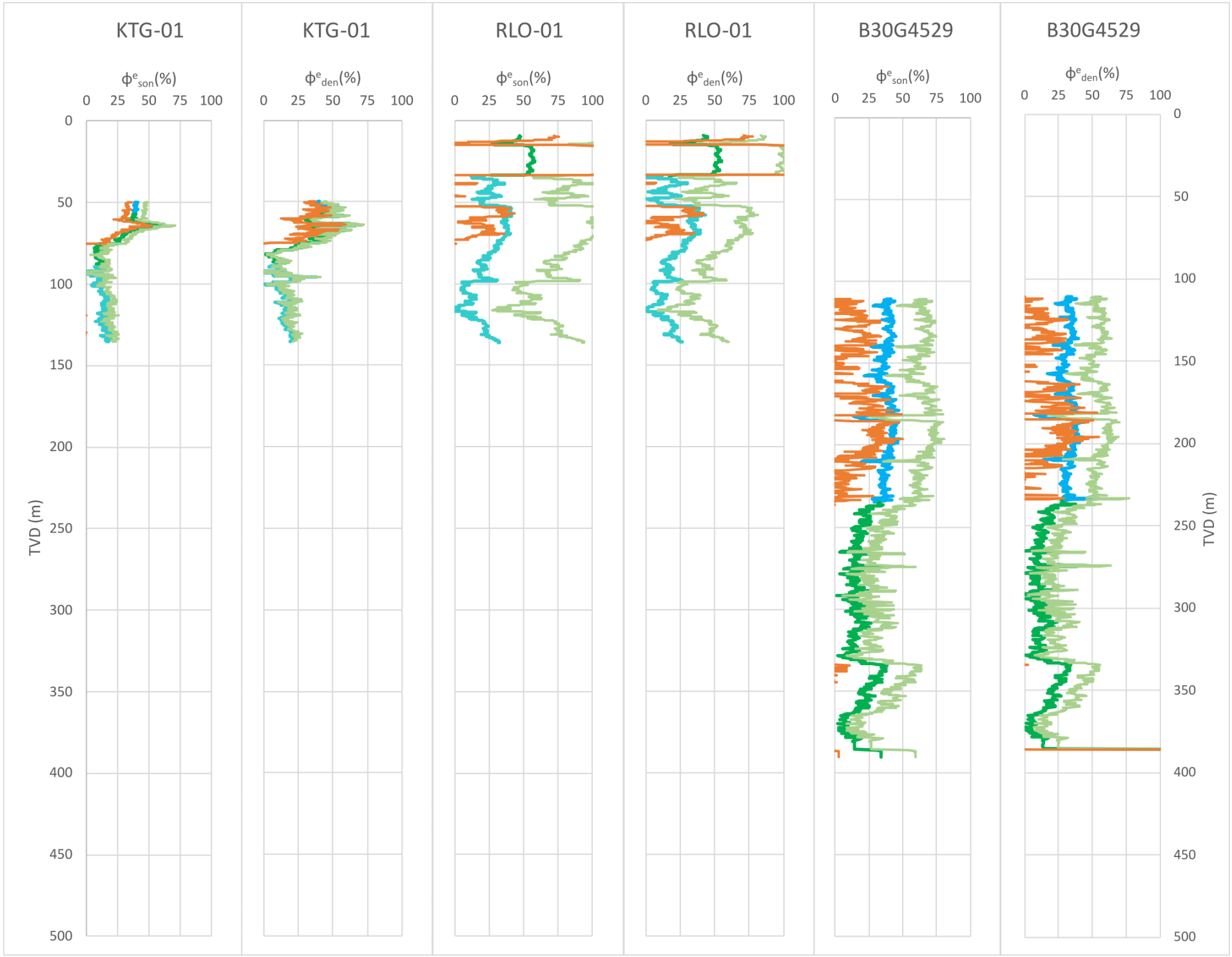
KTG-01
KTG-01
RLO-01
RLO-01
B30G4529
B30G4529
ϕ^e_son(%)
ϕ^e_den(%)
0 25 50 75 100
TVD (m)
0 50 100 150 200 250 300 350 400 450 500

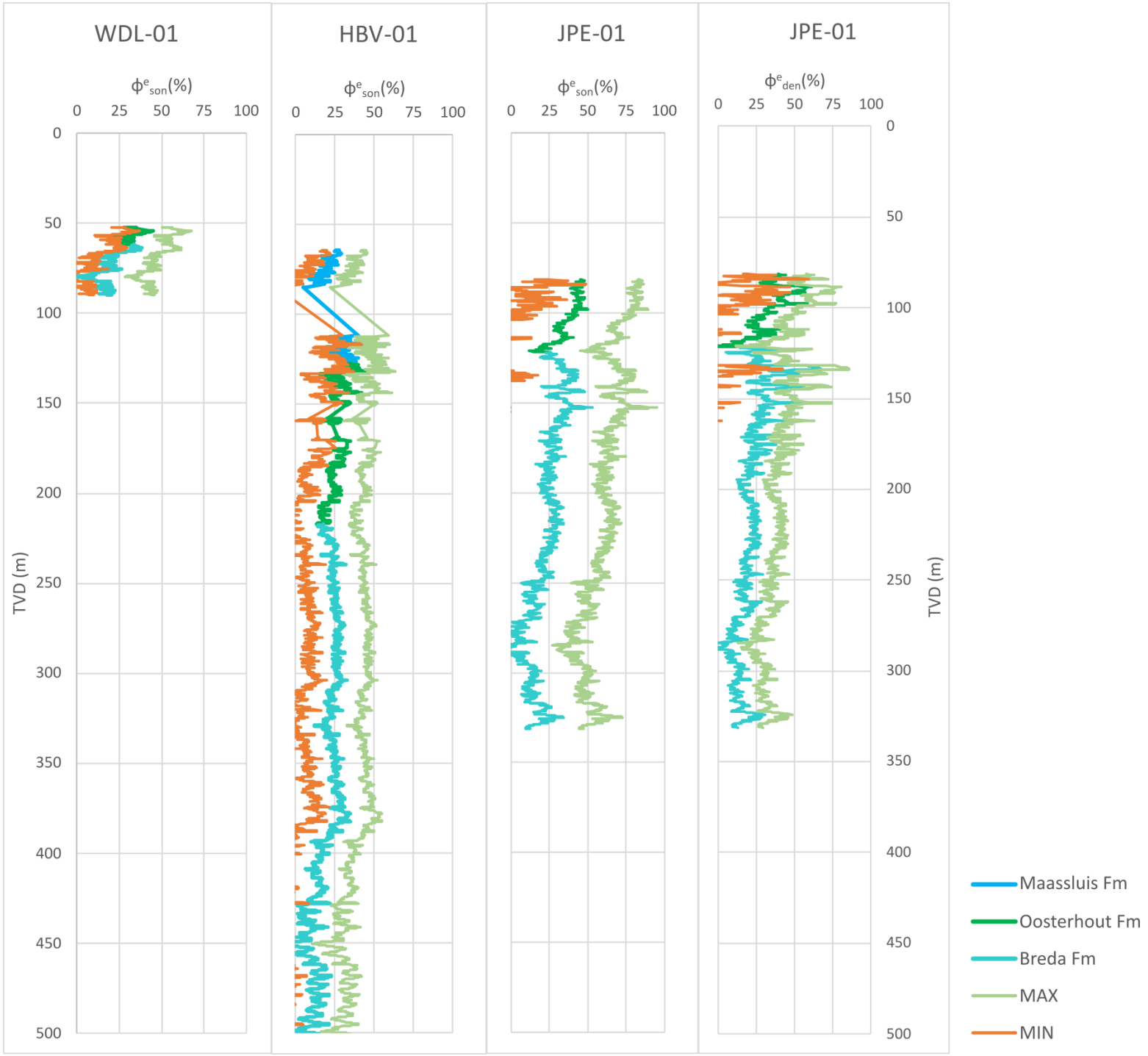
WDL-01
HBV-01
JPE-01
JPE-01
ϕ^e_{son}(%)
ϕ^e_{den}(%)
0 25 50 75 100
TVD (m)
0 50 100 150 200 250 300 350 400 450 500
Maassluis Fm
Oosterhout Fm
Breda Fm
MAX
MIN

Fig. 9.3 Overview of the φ^{e}_{son} and φ^{e}_{den} estimates, including minimum (red) and maximum (green) estimates based on selection of the most extreme parameters present in the log data for the Breda (turquoise), Oosterhout (green), and Maassluis (blue) Formations in well KTG-01, RLO-01, B30G4529, WDL-01, HBV-01, and JPE-01.

*Fig. 9.4 Overview of the gamma ray (GR), sonic slowness (DT), density (RHOB), porosity calculated from the sonic (**φ**SON), corrected porosity (**φ**SONc), porosity calculated from the density (**φ**DEN), presence of casing, and the composite log lithology for wells HBV-01, JPE-01, KTG-01, NWK-02, RLO-01, WDL-01, B30G4529, B49F0378, and DAPGEO_2_500m against the meter measured depth (mMD) along borehole. The lithology and size of the sand fraction is displayed in the selected combined shallow well. B30G4529, B49F0378, and DAPGEO_2_500m also include lithology data, which is displayed in the right columns. The stratigraphy tops are displayed with dotted lines; (NM)RUBO: Rupel Fm – unit of Boom, VE: Veldhoven Fm, BR(_TD): Breda Fm, BRAA: Unit of Aalten, BREI: unit of Eibergen, BRZE: unit of Zenderen, BRDE: unit of Delden, OO(_TD): Oosterhout Fm, MS: Maassluis Fm.*

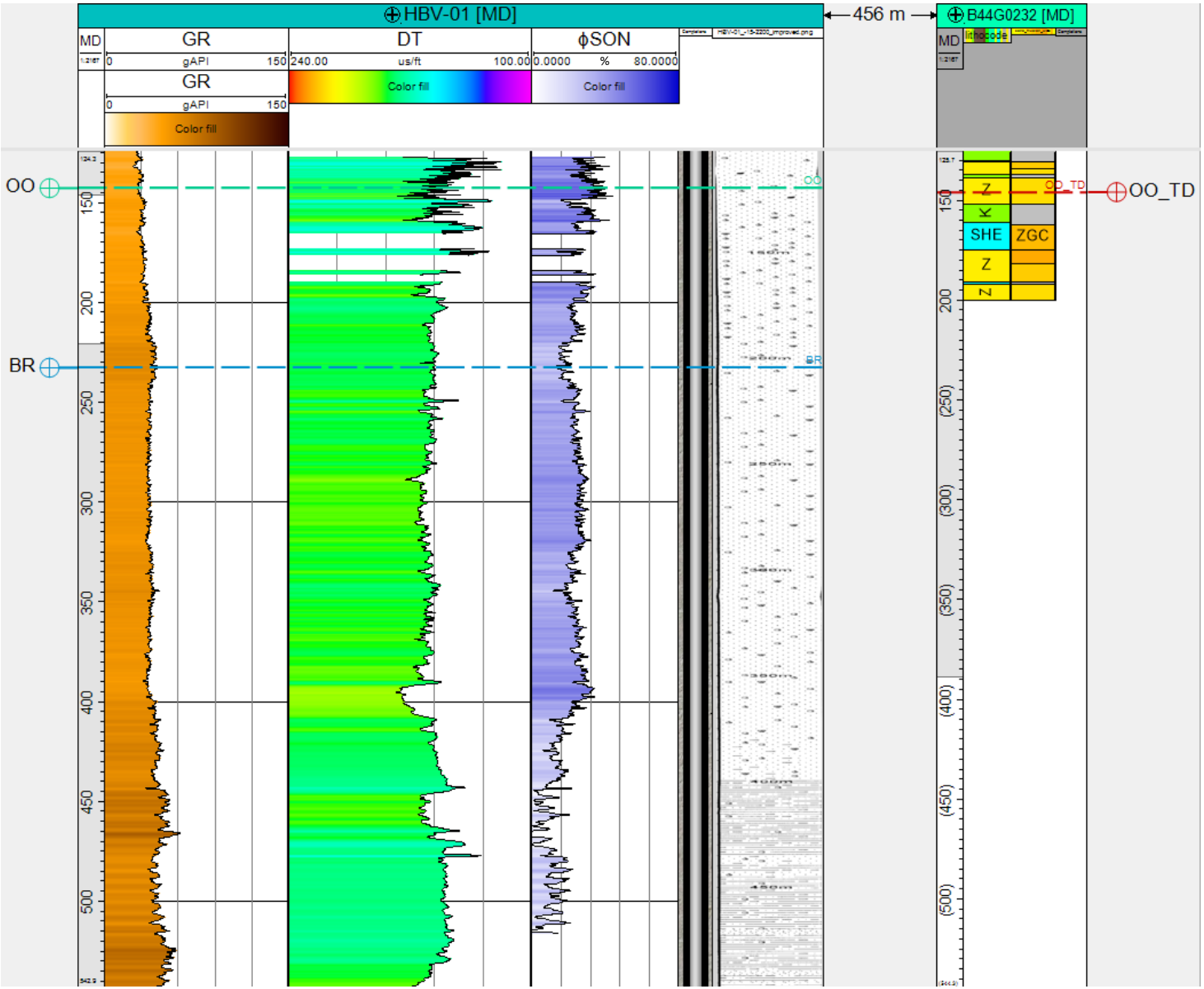
HBV-01 [MD]
456 m
B44G0232 [MD]
MD
GR
0
gAPI
150
DT
240.00
us/ft
100.00
ϕSON
0.0000
%
80.0000
Color fill
OO
BR
OO_TD
Z
K
SHE
ZGC
Z
N

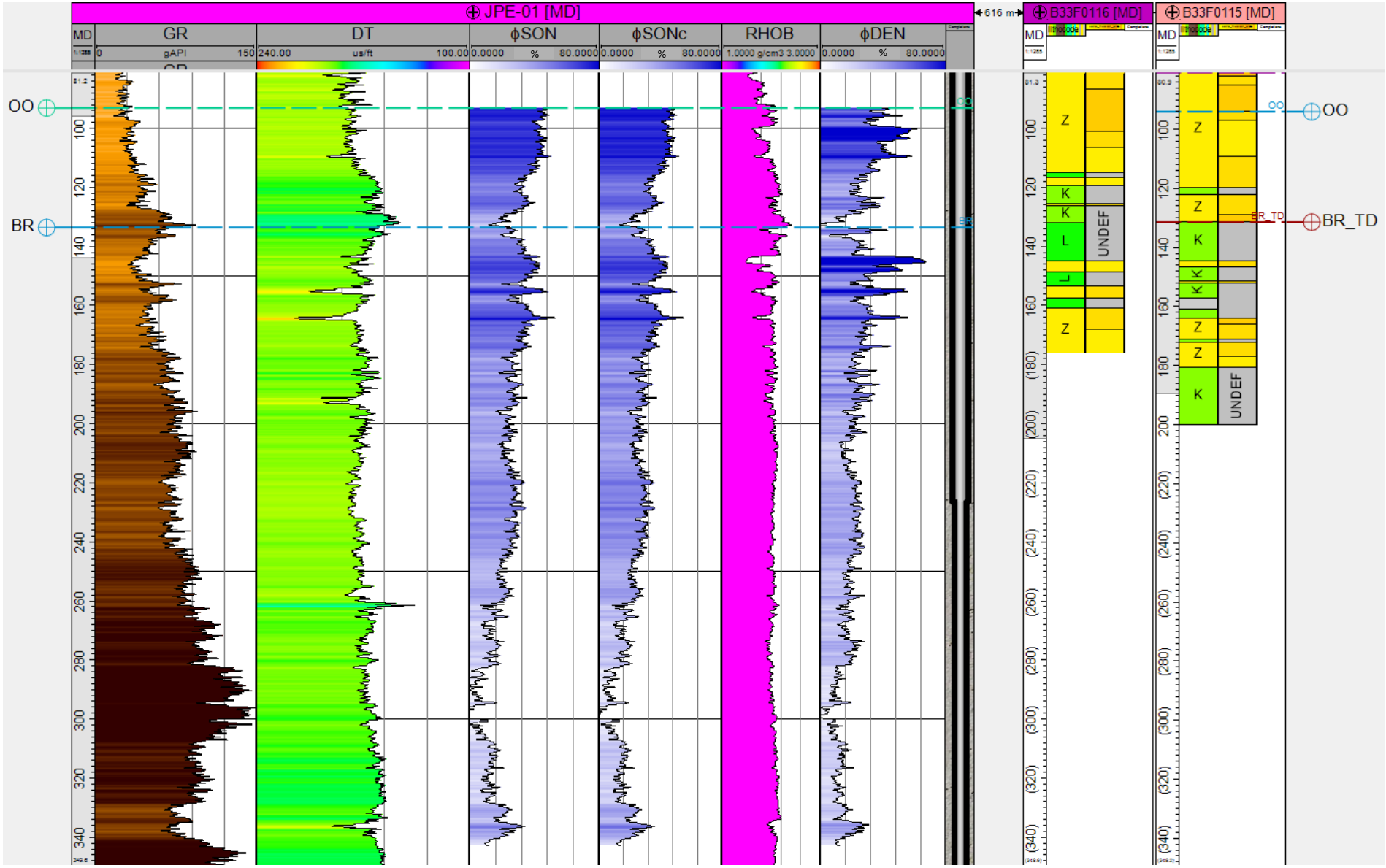
JPE-01 [MD]
616 m
B33F0116 [MD]
B33F0115 [MD]
MD
GR
gAPI
0
150
DT
us/ft
240.00
100.00
ϕSON
ϕSONc
RHOB
g/cm3
1.0000
3.0000
ϕDEN
%
0.0000
80.0000
OO
BR
BR_TD
Z
K
L
UNDEF

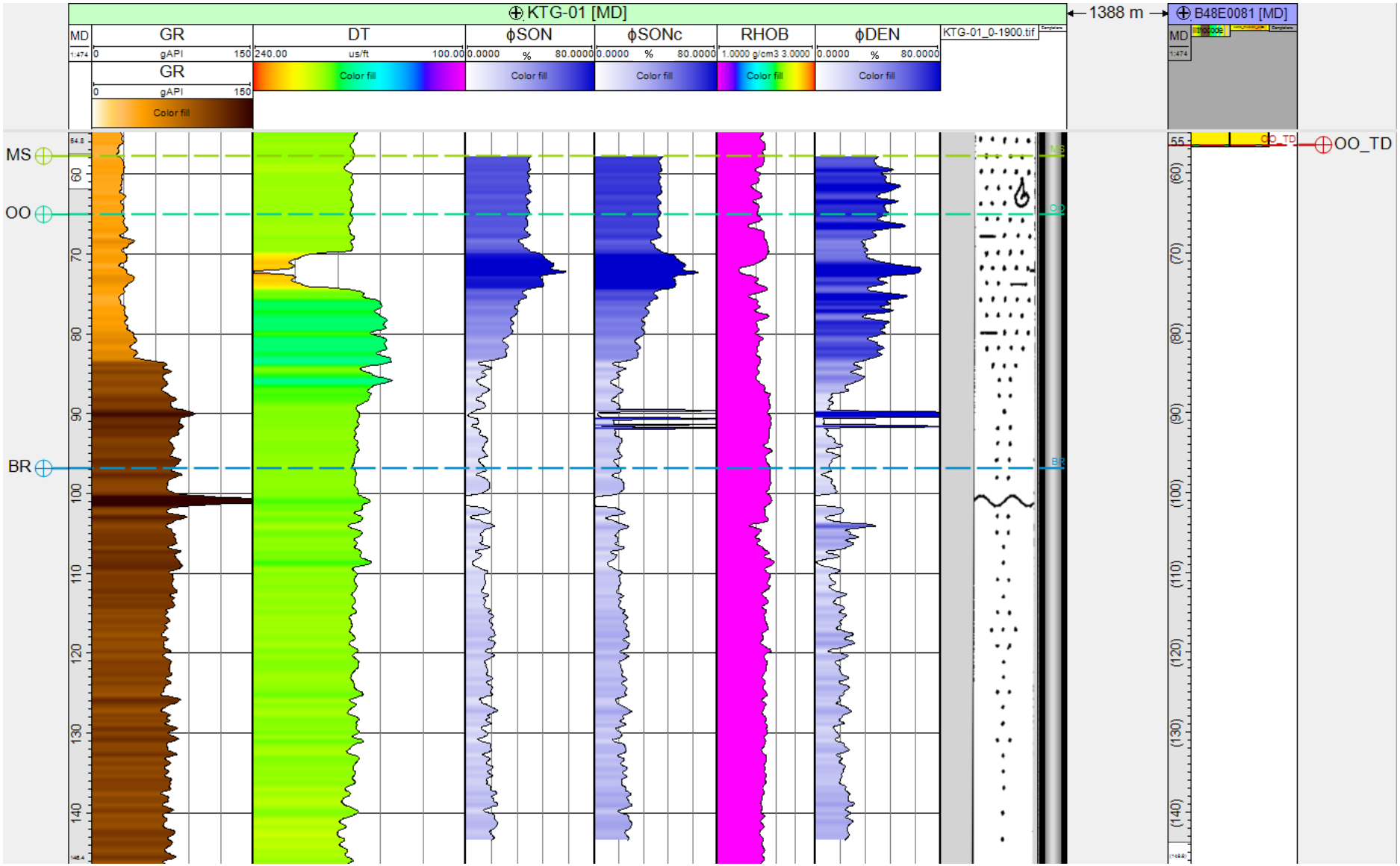
KTG-01 [MD]
1388 m
B48E0081 [MD]
MD
GR
DT
ϕSON
ϕSONc
RHOB
ϕDEN
KTG-01_0-1900.tif
0 gAPI 150
240.00 us/ft 100.00
0.0000 % 80.0000
1.0000 g/cm3 3.0000
Color fill
MS
OO
BR
OO_TD

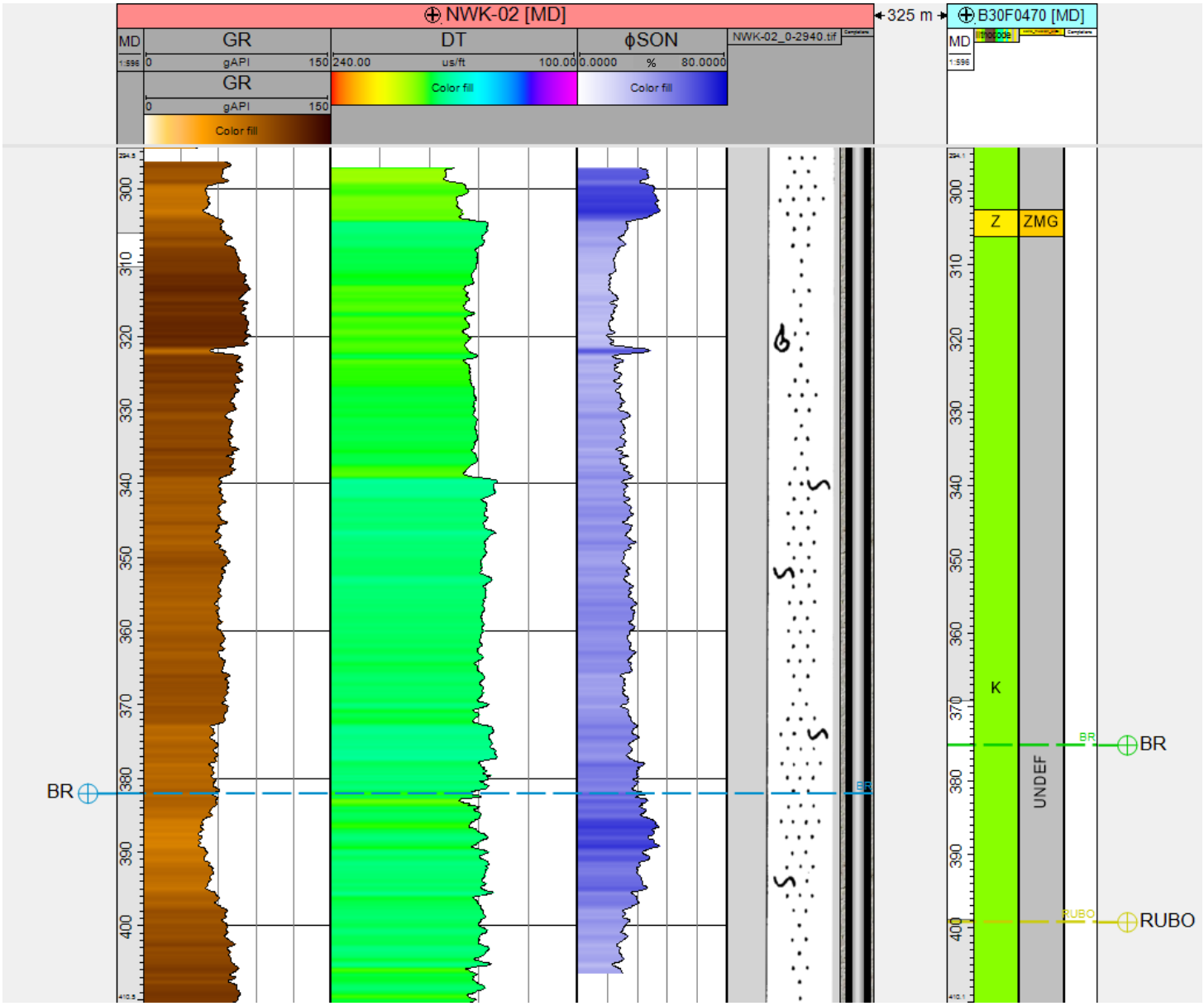
NWK-02 [MD]
325 m
B30F0470 [MD]
MD
GR
0 gAPI 150
DT
240.00 us/ft 100.00
ϕSON
0.0000 % 80.0000
NWK-02_0-2940.tif
Color fill
Z
ZMG
K
UNDEF
BR
RUBO
300
310
320
330
340
350
360
370
380
390
400

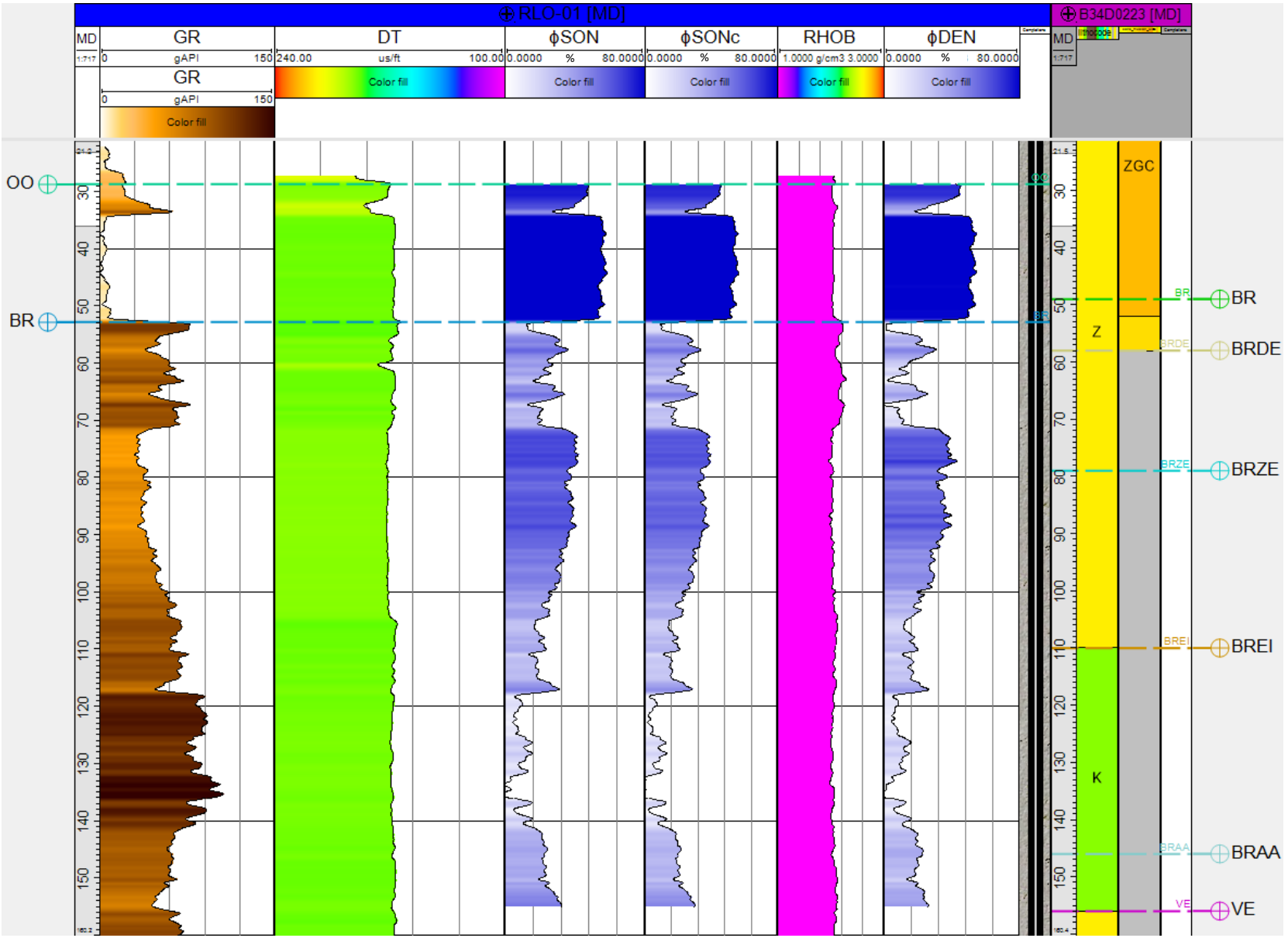
RLO-01 [MD]
B34D0223 [MD]
MD
GR
gAPI
0
150
DT
us/ft
240.00
100.00
ϕSON
ϕSONc
RHOB
g/cm3
1.0000
3.0000
ϕDEN
%
0.0000
80.0000
Color fill
OO
BR
ZGC
Z
K
BR
BRDE
BRZE
BREI
BRAA
VE

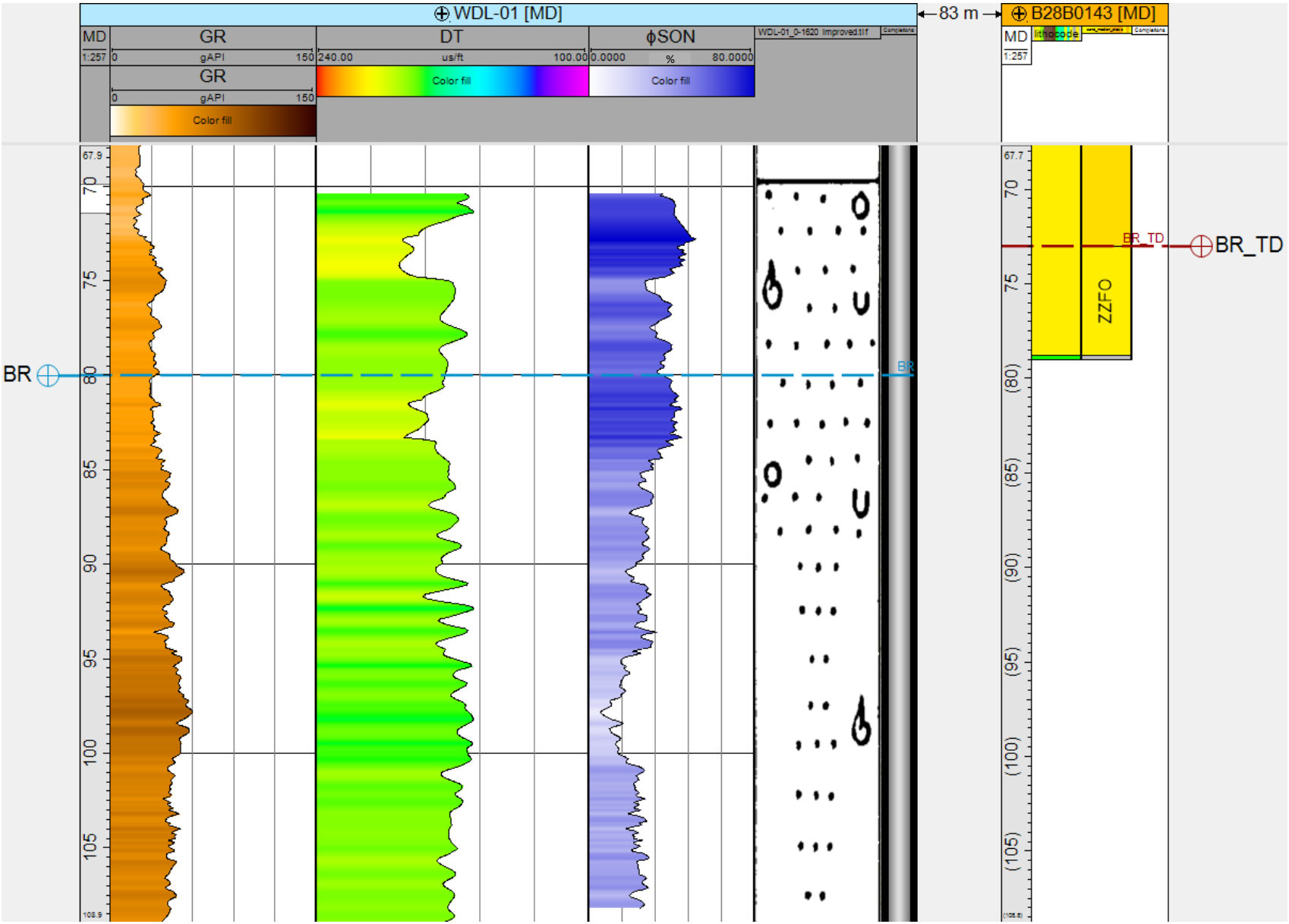
WDL-01 [MD]
83 m
B28B0143 [MD]
MD
1:257
GR
gAPI
0
150
DT
240.00
us/ft
100.00
ϕSON
0.0000
%
80.0000
Color fill
WDL-01_0-1620 Improved.tif
Lithocode
BR
BR_TD
ZZFO

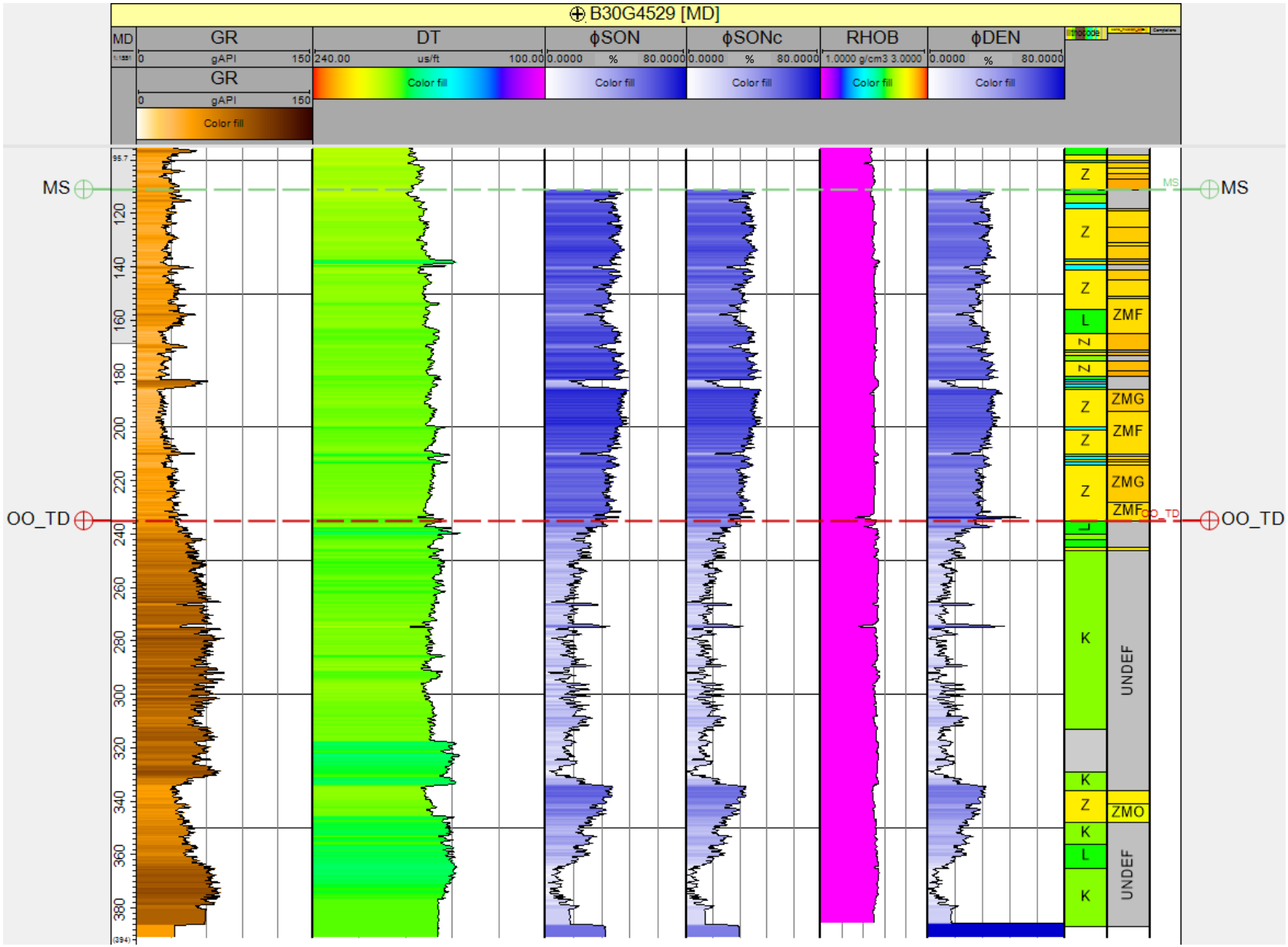
B30G4529 [MD]
MD
GR
0 gAPI 150
DT
240.00 us/ft 100.00
ϕSON
0.0000 % 80.0000
ϕSONc
0.0000 % 80.0000
RHOB
1.0000 g/cm3 3.0000
ϕDEN
0.0000 % 80.0000
Color fill
MS
OO_TD
ZMF
ZMG
ZMO
UNDEF

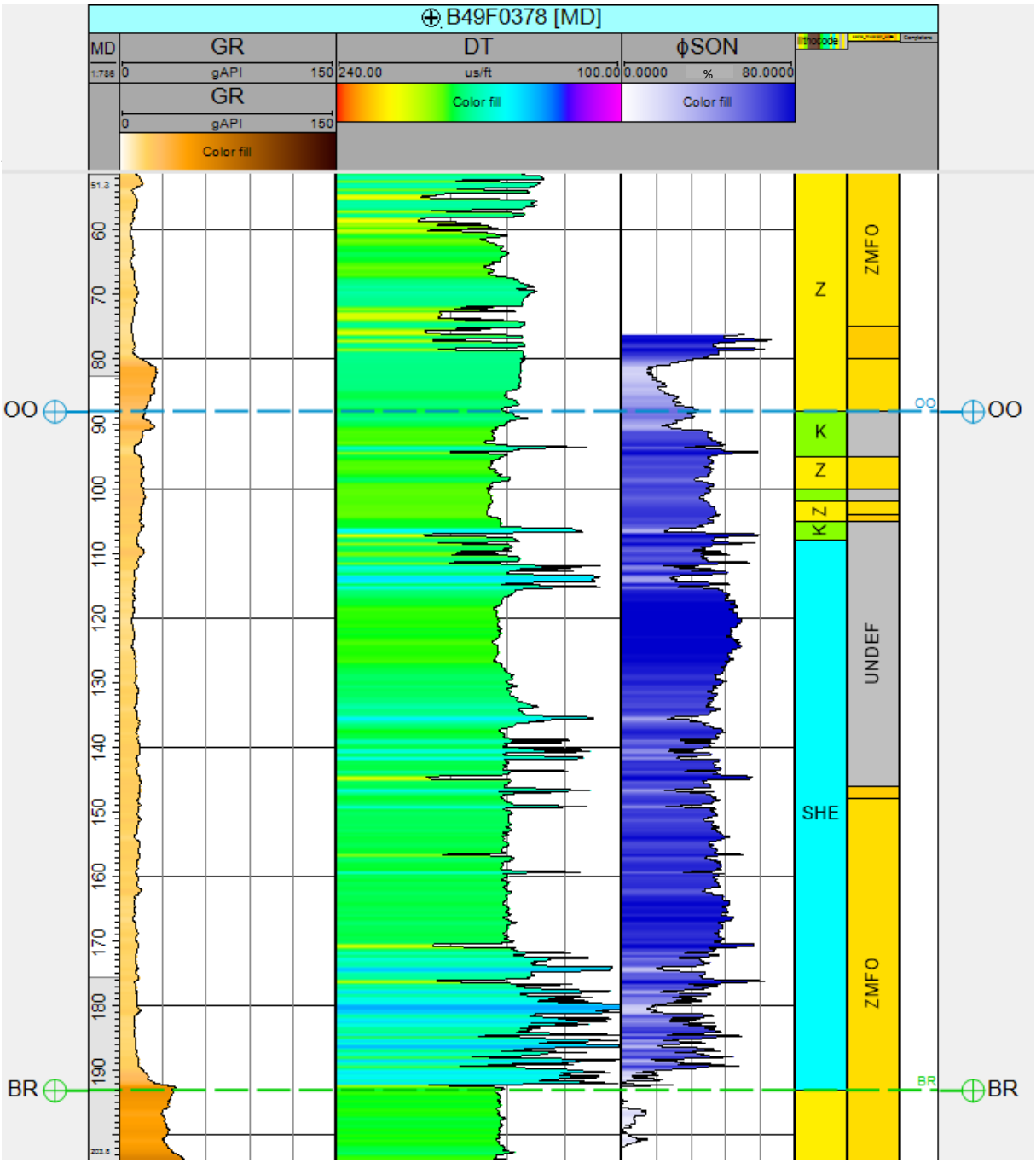
B49F0378 [MD]
MD
GR
0 gAPI 150
DT
240.00 us/ft 100.00
ϕSON
0.0000 % 80.0000
Color fill
Color fill
GR
0 gAPI 150
Color fill
OO
BR
Z
K
Z
K Z
SHE
ZMFO
UNDEF
ZMFO
OO
BR

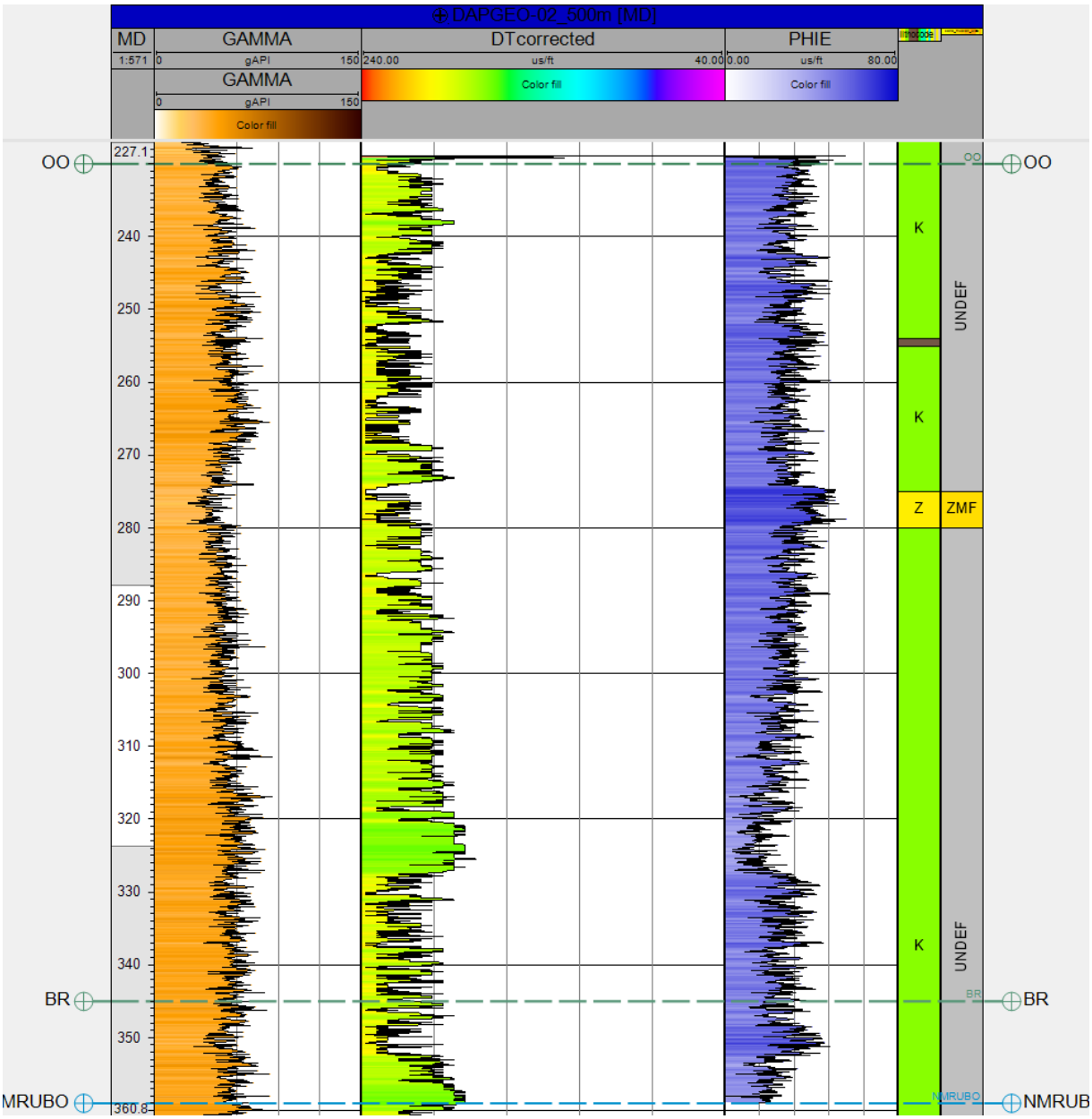
DAPGEO-02_500m [MD]
MD
1:571
GAMMA
0
gAPI
150
GAMMA
0
gAPI
150
Color fill
DTcorrected
240.00
us/ft
40.00
Color fill
PHIE
0.00
us/ft
80.00
Color fill
OO
BR
NMRUBO
227.1
240
250
260
270
280
290
300
310
320
330
340
350
360.8
K
K
Z
K
UNDEF
ZMF
UNDEF
OO
BR
NMRUB

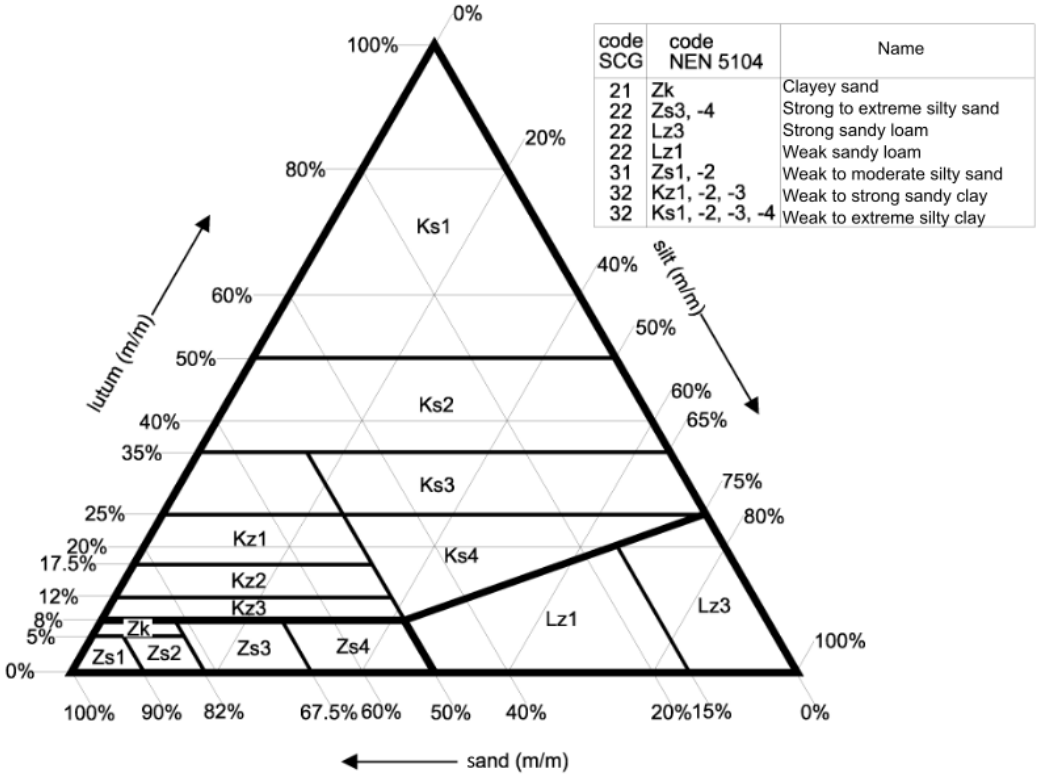

Fig. 9.6 Classification in lithology based on lutum, silt, and sand percentage according to NEN5104.

9.2 Tables

	Depo. Poro. [%]	Athy k $\left[\frac{1}{\text{km}}\right]$	Athy k $\left[\frac{1}{\text{MPa}}\right]$	Compress. y Max. $\left[\frac{10^{-7}}{\text{kPa}}\right]$	Compress. y Min. $\left[\frac{10^{-7}}{\text{kPa}}\right]$	Schneider Factor k_a $\left[\frac{1}{\text{MPa}}\right]$	Schneider Factor k_b $\left[\frac{1}{\text{MPa}}\right]$	ϕ
Limestone								
ooid grainstone	35.0	0.01	0.001	2.0	1.0	0.001	0.001	0.18
Waulsort. mound	16.0	0.01	0.001	2.0	1.0	0.001	0.001	0.08
micrite	51.0	0.52	0.04766	850.0	19.8	0.03212	0.07894	0.26
shaly	48.0	0.50	0.04493	686.5	18.8	0.03091	0.07090	0.24
org.–rich								
typical	51.0	0.52	0.04939	881.2	20.5	0.03329	0.08185	0.26
1-2% TOC	51.0	0.52	0.04851	865.1	20.1	0.03270	0.08037	0.26
10% TOC	51.0	0.52	0.05365	956.8	22.3	0.03616	0.08890	0.26
chalk, typical	70.0	0.90	0.10546	4613.3	41.6	0.20793	0.05813	0.35
chalk, 95% calcite	70.0	0.90	0.10546	4611.2	41.7	0.20793	0.05813	0.35
chalk, 75% calcite	67.0	0.90	0.10124	3871.1	40.6	0.19000	0.05738	0.34
chalk, 40% calcite	65.0	0.90	0.09870	3453.3	39.9	0.05891	0.18975	0.33
Marl	50.0	0.50	0.04651	778.0	19.8	0.07375	0.03086	0.25
Dolomite								
typical	35.0	0.39	0.03084	252.3	11.0	0.04219	0.02344	0.17
org.–lean, sandy	35.0	0.39	0.03119	255.2	11.2	0.04312	0.02344	0.17
org.–lean, silty	35.0	0.39	0.03138	256.7	11.2	0.04188	0.02406	0.17
org.–rich	35.0	0.39	0.03459	283.0	12.4	0.02656	0.04634	0.17

Table 9.1 Compaction parameters of carbonate rocks (Hantschel & Kauerauf, 2009).

	Depo. Poro. [%]	Athy k $\left[\frac{1}{\text{km}}\right]$	Athy k $\left[\frac{1}{\text{MPa}}\right]$	Compress. y Max. $\left[\frac{10^{-7}}{\text{kPa}}\right]$	Compress. y Min. $\left[\frac{10^{-7}}{\text{kPa}}\right]$	Schneider Factor k_a $\left[\frac{1}{\text{MPa}}\right]$	Schneider Factor k_b $\left[\frac{1}{\text{MPa}}\right]$	Schneider Factor ϕ
Biogenic Sediments								
Chalk, typical	70.0	0.90	0.10546	4611.2	41.7	5.00000	0.04500	0.35
Chalk, 95% calcite	70.0	0.90	0.10546	4611.2	41.7	0.20793	0.05813	0.35
Chalk, 75% calcite	67.0	0.90	0.10124	3871.1	40.6	0.19000	0.05738	0.34
Chalk, 40% calcite	65.0	0.90	0.09870	3453.3	39.9	0.05891	0.18975	0.33
Coal, pure	76.0	0.43	1.51396	87407.4	564.6	3.41736	0.74043	0.38
Coal, impure	74.0	0.42	0.22597	11692.7	87.9	0.49695	0.11328	0.37
Coal, silty	68.0	0.40	0.13392	5289.1	53.2	0.07308	0.28035	0.34
Clastic Sediments								
Sandstone								
typical	41.0	0.31	0.02660	274.7	11.5	0.04156	0.01781	0.20
clay–rich	40.0	0.32	0.02661	265.4	11.1	0.04000	0.01812	0.20
clay–poor	42.0	0.30	0.02627	280.5	11.8	0.04047	0.01734	0.21
quartzite								
typical	42.0	0.30	0.02726	291.0	12.2	0.04281	0.01781	0.21
very quartz–rich	42.0	0.27	0.02461	252.6	11.8	0.01615	0.03977	0.21
subarkose								
typical	41.0	0.28	0.02468	244.8	11.4	0.01631	0.03874	0.20
quartz–rich	42.0	0.28	0.02533	263.4	11.9	0.03984	0.01641	0.21
clay–rich	42.0	0.30	0.02643	282.2	11.8	0.04063	0.01750	0.21
clay–poor	42.0	0.30	0.02627	280.5	11.8	0.04047	0.01734	0.21
dolomite–rich	40.0	0.30	0.02572	249.8	11.2	0.04000	0.01688	0.20
arkose								
typical	39.0	0.33	0.02772	267.3	11.2	0.01981	0.04212	0.20
quartz–rich	41.0	0.30	0.02623	267.1	11.6	0.04094	0.01750	0.20
quartz–poor	40.0	0.32	0.02646	263.9	11.1	0.04000	0.01812	0.20
clay–rich	40.0	0.32	0.02661	265.4	11.1	0.04000	0.01812	0.20
clay–poor	39.0	0.32	0.02722	258.9	11.2	0.04063	0.01812	0.20
dolomite–rich	39.0	0.32	0.02658	252.8	11.0	0.03875	0.01812	0.20
wacke	39.0	0.34	0.02773	271.1	10.9	0.01992	0.04192	0.20

Table 9.2 Compaction parameters of biogenic and clastic sediments (Hantschel & Kauerauf, 2009).

	Depo. Poro. [%]	Athy k $\left[\frac{1}{\text{km}}\right]$	Athy k $\left[\frac{1}{\text{MPa}}\right]$	Compress. y Max. $\left[\frac{10^{-7}}{\text{kPa}}\right]$	Compress. y Min. $\left[\frac{10^{-7}}{\text{kPa}}\right]$	Schneider Factor k_a $\left[\frac{1}{\text{MPa}}\right]$	Schneider Factor k_b $\left[\frac{1}{\text{MPa}}\right]$	ϕ
Shale								
typical	70.0	0.83	0.09613	4032.7	40.3	0.19157	0.05270	0.35
org.–lean								
typical	70.0	0.83	0.09613	4032.7	40.3	0.19157	0.05270	0.35
sandy	65.0	0.83	0.08999	3005.2	38.7	0.17479	0.05340	0.33
silty	67.0	0.83	0.09230	3373.4	39.4	0.18394	0.05357	0.34
silic., typical	70.0	0.83	0.09556	4007.5	40.1	0.19043	0.05238	0.35
silic., 95% Opal–CT	80.0	0.83	0.14631	7397.5	37.8	0.33248	0.06983	0.40
black	70.0	0.83	0.10931	4584.3	45.8	0.22348	0.06082	0.35
organic–rich								
typical	70.0	0.83	0.10931	4291.1	42.9	0.18549	0.05265	0.30
3% TOC	70.0	0.83	0.10165	4264.1	42.6	0.20782	0.05656	0.35
8% TOC	70.0	0.83	0.10931	4584.3	45.4	0.22348	0.06082	0.35
20% TOC	70.0	0.83	0.12975	5441.2	54.4	0.26527	0.07219	0.35
Siltstone								
org.–lean	55.0	0.51	0.04907	1036.1	21.1	0.03165	0.08611	0.28
organic–rich								
typical	55.0	0.51	0.04937	1042.2	21.2	0.03185	0.08660	0.28
$>$ 10% TOC	55.0	0.51	0.05459	1152.6	23.5	0.09119	0.03419	0.28
2-3% TOC	55.0	0.51	0.04966	1048.7	21.4	0.03204	0.08714	0.28
Conglomerate								
typical	30.0	0.30	0.02429	142.1	8.8	0.01897	0.03228	0.15
quartzitic	30.0	0.30	0.02429	142.1	8.8	0.01897	0.03228	0.15
Tuff, felsic	60.0	0.35	0.03711	959.1	16.5	0.06961	0.02117	0.3
Tuff, basaltic	60.0	0.35	0.03212	829.3	14.3	0.06000	0.01844	0.3

Table 9.3 Compaction parameters of clastic sediments (Hantschel & Kauerauf, 2009).

Deep well	GR	DT	RHOB/DRHO	Composite lit	Por/perm	Shallow well	Lit	Lit vs strat	Strat deep vs strat undeep	Lit vs GR	Lit vs DT	Lit vs por/perm	Distance (m)	Overall quality
NWK-02	Interesting transition from 296 MD (not at the same level as transition sand-clay (undeep), but seems ok	Looks fine	Too deep for comparison	Lacks detail for comparison		B30F0470	Detailed	MS: More clay towards bottom. OO: Mostly clay. BR: clay, based on presence glauconite	Bottom MS deep=top OO undeep	385-395 MD: sand expected, but clay. Sand-clay transitions from 20 MD to 220 MD not clear	Lower DT not well correlated to clay units		325	
KTG-01	Big shift to higher values at 83 MD, but seems ok	Weird lack in data around 73 MD, but looks good in the other parts	Very small overlap, but looks good	Unconformity in composite at the same place as base Breda. Also at higher depth lots of matches between composite and interpreted stratigraphy borders.	Porosity only for sands good calculated. Doubts on permeability. Calculated for Brussels sand parameters and not Oosterhout	B48E0081	Detailed	OO: Verty thin clay layer visible, MS: Sand and thin clay layer	Basis NUCT just above top OO. OO deep and shallow 35 m different height	Too little overlap for major correlations, values could match with sand	Too little overlap for major correlations, values could match with sand	Little overlap with lit. Permeability above NUCT probably incorrect. Porosity above 0.4 can match with sand	1388	
SCH-2952	Very noisy with a lot of small peaks. DGRC. Very high values	Almost no difference, could be the case due to the relatively small interval				B22F0008	OK	OO: only sand in this small interval	No strat of SCH-2952	Very high values for sand	Sand all has similar velocities		1108	
WDL-01	Looks good, present in Upper Northsea	Seems a bit noisy in the upper part, but overall ok	Too deep for comparison	Good correlation with strat deep well		B28B0143	Detailed	OO: all sand, BR: sand and a little bit of loam. Not comparable with deep strat as only bottom NU is given	Only NU in deep strat, so not comparable. Can fit with undeep strat	Loam good visible very undeep. Also slightly higher GR below top OO and higher towards bottom BR.	Relatively big transitions in DT for the interpreted sandy lithology		83	
HBV-01	Looks good	Lots of intervals with gaps in the DT record. Also a lot of noise, which questions the quality of this log in above 175 MD. Below this point it looks good	Too deep for comparison	No good allignment, but at fluctuations in the GR and sonic also different layers in the composite are visible.		B44G0232	Detailed, thick shell layer at 155 MD	OO: Sand, shells, and some clay, MS: Mostly clay layers, thin shell layer and sands, MS:	Basis MS in deep well not correlated to top OO in shallow wel.	Some higher GR values at thin clay layers, but no complete match with the lithology	Only a small overlap with the "good" quality DT log. Somewhat lower DT at shell layers and clay layers		456	
HBV-01						B44G0233	Detailed, thick shell layer at 155 MD	OO: thick shell layers, clays and 2 thin sand layers, MS: Sand, clays and a very thin shell layer.	NUCT/top MS close to top MS shallow.	No good correlation between GR and clay-sand alterations	Lit only overlaps with bad part of DT log. No good correlation		523	
HBV-01						B44G0226	Detailed, thick shell layer at 155 MD	BR: thick shell layer and sand, OO: Sand, MS: sand and clay	Top MS shallow correlated ith NUCT in deep. Top OO in shallow and base MS also fine correlation.	Seems to be a correlation between clay and higher GR, but no correlation between shell layer and GR	Shell layer not clear in DT due to missing parts. No other lithologies to compare except for sand		460	
HBV-01						B44G0221	Detailed, also the shell layer	OO: part shells, clay and some sand, MS: Mostly sand and some clay	MS well top in shallow well closeby top OO in deep well	No other GR values for shell layer. Around 87 MD lower GR for clay layers, but not every interpreted clay layer matches with higher values	Only a small overlap with the "good" quality DT log. Somewhat lower DT at shell layers and clay layers		848	
HBV-01						B44G0313	Detailed, also the shell layer	OO: shell layer, clays and some sand, MS: Mostly sand and some clay layers	Basis MS in deep close to top OO in shallow	Higher GR also around 87 MD, but not perfectly alligning to the clays.	Only a small overlap with the "good" quality DT log. Somewhat lower DT at shell layers and clay layers		950	
HBV-01						B44G0072	From 157 MD unrealistic thick shell layer	OO: thick shell layer and sand, MS: sand and clay on top	Base MS from deep in between top OO and MS in shallow	Shell layer not matching with different GR. Clay layers somewhat higher GR	Higher at thick shell layer, but no good correlation visible		874	
HBV-01						B44G0225	Detailed, with shell layer	OO: Shell layer, sand and thin clay layer on top, MS: Sand and little clay on top	NUMS of deep close to top OO in shallow and NUCT of deep a little above top MS in shallow	Around clays somewhat higher GR, but no good correlation	Transition shells to sand shows higher DT		732	
HBV-01						B44G0224	Detailed, with shell layer	OO: Shell and sand, MS: Sand and a thin clay layer in middle	Base OO correlates with top OO of shallow well, Base MS correlates to top WA, so no good correlation	Around clays somewhat higher GR, but no good correlation	No big overlap		615	

HBV-01						B44G0230	Very detaild, small shell layers also	MS: sand and clay on top	Top MS in shallow close to NUCT in deep	Some clays have higher GR. No correlation with shell layers	No big overlap		899
HBV-01						B44G0220	Detailed, no shell	OO: Sand and some thin clay layers, MS: sand, some clay layers	Top MS in shallow below base MS in deep. Top OO just above base OO in deep. Not good	Some clays show higher GR	No big overlap		1080
HBV-01						B44G0156	Very detaild, small shell layers also	OO: shell layers, sand, clay, MS: Sand and some thin clay layers	Top MS in shallow below base MS in deep. Top OO just above base OO in deep. Not good	Around clays somewhat higher GR, but no good correlation	No big overlap		1232
HBV-01						B44G0218	Detailed, no shell	OO: Sand and some thin clay layers, MS: sand, some clay layers	Top MS in shallow below base MS in deep. Top OO just above base OO in deep. Not good	Some clays have higher GR.	No big overlap		1451
HBV-01						B44G0217	Detailed, small shell layer	OO: thin shell layer, sand and little clay, MS: Sand and clay layers near top	Top OO correlated to base MS deep well. Top MS just below base NUCT in deep.	Some clays have higher GR.	No big overlap		1474
BKH-01	Looks good	Relatively low velocities compared to other wells	Too deep for comparison	Lacks detail for comparison		B33G0154	Detailed	OO: Mostly sand with minor clay, MS: Predominantly sand and very little clay	Old NUCT (basis Quartair) used in deep. No clear correlations with top Oosterhout and top Maassluis.	No clear correlations between GR and lit, overall below NCT more clays and higher GR values	No overlap between lit and DT		150
JPE-01	OK	Below 70 MD looks fine. Some higher DTS	Too deep for comparison			B33F0115	Detailed	MS: Mostly sand, little clay, OO: Mostly sand, little clay, BR: Mostly clay and some sand	Old NUCT (basis Quartair) used in deep. No clear correlations with top BR, OO and MS	Relatively higher GR at clays	Not perfectly matching, but somewhat higher DTs at clay intervals		622
JPE-01						B33F0116	Detailed			Lower at parts with loam and clay but not detailed correlation	Lower DT at clays and loam, but no detailed correlation		515
BLF-106	Relatively high values, GRPD	Above 52 MD unreliable DT fluctuations		Lacks detail for comparison		B06A0076	Detailed	BR: Almost completely sand beside one small interval clay.	Only NU in deep strat, so not comparable. Can fit with undeep strat	No clear differences in GR values between sandy and clayey intervals	Smaller DT values for clays?		1463
SPKO-02	Lots of peaks, but could be ok. GRS	Very low DTs. From 180 MS very noisy.				B37G0154	Very detailed, thin layers	MS: sand and a little loam at top	Only NU in deep strat, so not comparable. Can fit with undeep strat	No good correlation	No good correlation		1766
RLO-01	From 5-35 MD and below 480 MD very low GR. Further OK	Looks fine	Pretty constant, looks ok			B34D0223	Detailed	BR: clay at bottom and sand on top	Base Breda in deep well very close to BRAA. OO in deep well, but not in shallow well	Overall higher GR at clay intervals	No clear correlation		0
DRT-01	OK	Relatyively low values over complete log and some gaps	Too deep for comparison	Good correlation with GR and well tops strat		B38C0732	Detailed	MS: sand and clay on top	Only N in deep strat, so not comparable. Undeep well could fit with deep	No good correlation	No clear correlation		1835
DRT-01						B38C0445	Detailed	OO: sand and clay layers alternations, MS: clay, sand, shell alternations and sand layer on top	Only N in deep strat, so not comparable. Undeep well could fit with deep	No good correlation	No clear correlation		1775
STH-01	OK	Some random peaks	Too deep for comparison	Some correlation with GR and strat		B44D0488	Detailed	MS: sand and clay on top	No overlap	No overlap	No overlap		936
SMG-01	OK	Looks ok, but big transitions	Too deep for comparison	Some correlation with GR and strat, but not so much		B45D0124	Detailed	MS: sand and clay on top	Base Kiezeloöliet in deep beneath top Kiezeloöliet and MS in shallow, so OK	No clear correlation	No clear correlation		923
VAL-01	OK	OK	Some dips, but overall constant	No good correlation		B30E0093	Not so detailed, mostly sand	No BR, OO, MS	MS from deep well to deep to correlate to undeep well	Lower values for clay at 1 MD? GR shows different values in the thick sand layer	Only sand can be correlated, seems fine		845
						B30G0935	Detailed	MS: Clay and sand and a little shell interval, OO: Mostly clay and a little sand, BR: Clay		Higher values for clay layers from 42 MD and 240 MD. Above less good correlation			
						B30G4529	Detailed (more than above)	MS: Clays and sands and some small shell intervalls, OO: Loam, clay and very little amount of sand		Higher GR for clays and loam compared to sands.	Lower DT for clays and shells than sand		Same well

	Very low values over whole log.	A lot of noise, doubts on quality		B49F0378	Detailed, from 105 MD very thick shell layer	BR: sand, OO: thick shell layer at base with on top alternations of sand and clay layers.		Somewhat higher GR at clay layers, lower GR at thick shell layer	Too noisy to make correlations			
DAPGEO-02_500m	Very small interval with GR. Looks ok			DAPGEO-02_500m	Detailed, ending in kalksteen			Higher at clays and lower at sands, very good correlation. Very low GR at KAS			0	

Table 9.4 Quality interpretation of deep and shallow well combinations and shallow wells including both log and lithology data.

Well	Drilling mud type	Mud filtrate resistivity (Ωm)	Formation Temperature (°C)
HBV-01	-	-	-
JPE-01	Basic Bentonite	3.5	15.5
KTG-01	Fresh water bentonite	0.286	20
NWK-02	Fresh water bentonite	1.13	14
RLO-01	Basic Bentonite	4.35	20
WDL-01	Fresh water bentonite	0.112/1.87	22/30
B30G4529	Water based	-	-
B49F0378	Water based	-	-
DAPGEO_2_500m	-	-	-

Table 9.5 Drilling mud type, mud filtrate resistivity, and formation temperature of the selected wells. Wells HBV-01, B30G4529, B49F0378, and DAPGEO_2_500m lack data on the salinity of the drilling mud. The DT_{fl} and ρ_{fl} values are therefore estimated based on fresh water (Table 2.2).

Well	GR_{max}			GR_{min}			DT_{ma}	DT_{fl}			C_p		
	<		>	<		>		<		>	<	>	*
WDL-01	55	60	97	17	17	40		214.0	217.8	217.8	1.57	1.65	1.89	-
HBV-01	39	51	61	24	24	32		214.5	218	218	1.31	1.50	1.58	-
NWK-02		84			35				217.6			1.42		-
B49F0378		25			9		56		218.0			1.22		-
JPE-01	39	130	139	21	23	57			217.9		1.23	1.60	1.86	1.55
KTG-01	66	95	96	20	20	30			216.5		1.62	1.70	1.83	1.58
RLO-01	45	104	104	31	32	75			217.9		1.14	1.75	1.76	1.85
B304529	35	72	75	20	20	44			218.0		1.52	1.56	1.81	1.64

Table 9.6 Overview of minimum (<), carefully selected, and maximum (>) parameters obtained from sonic and gamma ray log, well, and literature data to calculate the φ^e_{son}(*) (Geel & Foeken, 2021). For NWK-02 and B49F0378 no minimum and maximum data were distinguished. Cp shows the corrected compaction factors, where the φ^e_{son} estimates are adjusted to have a better fit with φ^e_{den} estimates. WDL-01, HBV-01, NWK-02, and B49F0378 lack density log data and therefore do not have a corrected compaction factor.*

Well	ρ_{ma}	ρ_{fl}	ρ_{sh}		
			<		>
JPE-01	2.65	1.0	1.98	2.15	2.20
KTG-01			1.66	2.08	2.09
RLO-01			1.88	2.00	2.23
B304529			1.70	2.06	2.11

Table 9.7 Overview of the minimum (<), selected, and maximum (>) parameters obtained from density log and literature data to calculate the φ^e_{den}.